Architecture of the native doublet microtubule

Corbin Steven Black

Anatomy and Cell Biology

McGill University, Montreal

May 2023

A thesis submitted to McGill University in partial fulfillment of the requirements of the degree of Doctor of Philosophy

Table of Contents

ABSTRACT (ENGLISH) ..... **- 5 -**

ABSTRACT (FRENCH) ..... **- 7 -**

ACKNOWLEDGMENTS ..... **- 9 -**

PREFACE ..... **- 10 -**

CONTRIBUTIONS TO ORIGINAL KNOWLEDGE ..... - 10 -
DETAILED CONTRIBUTIONS OF EACH AUTHOR ..... - 11 -

LIST OF ABBREVIATIONS AND TERMS USED IN THIS THESIS ..... **- 14 -**

INTRODUCTION, RATIONALE AND RESEARCH OBJECTIVES ..... **- 15 -**

CHAPTER 1: LITERATURE REVIEW ..... **- 19 -**

1.1 CILIA AND FLAGELLA ..... - 19 -
1.2 CILIOPATHIES ..... - 20 -
1.3 *TETRAHYMENA THERMOPHILA* AS A MODEL ORGANISM ..... - 21 -
1.4 ARCHITECTURE OF THE CILIUM AND THE AXONEME ..... - 23 -
1.5 DOUBLET MICROTUBULES AND TUBULIN POST-TRANSLATIONAL MODIFICATIONS ..... - 27 -
1.6.1 MICROTUBULE-ASSOCIATED PROTEINS ..... - 33 -
1.6.2 MICROTUBULE INNER PROTEINS ..... - 36 -
1.7 CRYOGENIC ELECTRON MICROSCOPY, DATA PROCESSING, AND PROTEIN STRUCTURE MODELLING ..... - 39 -
1.8 ADVANCES IN DOUBLET MICROTUBULE CRYOGENIC MICROSCOPY SAMPLE PREPARATION ..... - 42 -

CHAPTER 2: MOLECULAR ARCHITECTURE OF THE DMT OF *TETRAHYMENA THERMOPHILA* ..... **- 44 -**

2.1 METHODS – SAMPLE PREPARATION OF *TETRAHYMENA* DMTS FOR MASS SPECTROMETRY ANALYSIS AND CRYO-EM ..... - 44 -
2.1.1 Growth of Tetrahymena strain CU428 ..... *- 44 -*
2.1.2 Cilia purification from Tetrahymena strain CU428 ..... *- 45 -*
2.1.3 DMT preparation from purified Tetrahymena cilia ..... *- 47 -*
2.1.4 Salt treatment for mass spectrometry analyses of DMTs purified from Tetrahymena strain CU428 cilia ..... *- 48 -*
2.1.5 DMT preparation from purified Tetrahymena strain CU428 cilia for cryo-EM and non-salt washed mass spectrometry ..... *- 49 -*
2.1.6 Mass spectrometry sample preparation of cilia from Tetrahymena RIB72 knockout strains RIB72B-KO and RIB72A/B-KO ..... *- 49 -*
2.2 METHODS – MASS SPECTROMETRY DATA COLLECTION OF *TETRAHYMENA* STRAINS *CU428*, *RIB72B-KO*, AND *RIB72A/B-KO* - 50 -
2.2.1 Mass spectrometry data collection of Tetrahymena strains CU428, RIB72B-KO, and RIB72A/B-KO ..... *- 50 -*
2.2.1 Mass spectrometry data analysis of Tetrahymena strains CU428, RIB72B-KO, and RIB72A/B-KO ..... *- 51 -*
2.3 METHODS – CRYO-EM SAMPLE PREPARATION OF DMTS FROM *TETRAHYMENA* STRAIN *CU428* ..... - 51 -
2.4 METHODS – CRYO-EM DATA COLLECTION (SINGLE PARTICLE ANALYSIS) ..... - 52 -
2.5 METHODS – CRYO-EM DATA PROCESSING (SINGLE PARTICLE ANALYSIS) ..... - 53 -
2.6 METHODS – PROTEIN STRUCTURE MODELING AND MODEL VALIDATION ..... - 55 -
2.7 RESULTS AND DISCUSSION ..... - 57 -
2.7.1. Cryo-EM map of the Tetrahymena DMT ..... *- 57 -*
2.7.2. Tetrahymena DMT consists of conserved and non-conserved MIPs ..... *- 58 -*
2.7.3 MIP distribution in Tetrahymena has 96-nm periodicity ..... *- 69 -*
2.7.4 RIB72A and RIB72B are differentially required for the stability of several A-tubule MIPs ..... *- 70 -*
2.7.5 Organization of the inner and outer microtubule proteins in Tetrahymena axonemal DMTs is uncoupled - *73 -*
2.7.6 The outer surface of the intact DMT is associated with many filamentous proteins ..... *- 75 -*
2.7.7 The PG-rich motif is a novel microtubule-binding domain ..... *- 80 -*

CHAPTER 3: STRUCTURAL AND FUNCTIONAL CHARACTERIZATION OF THE CFAP77 KNOCKOUT MUTANT .....- 85 -

3.1 METHODS – SAMPLE PREPARATION OF *TETRAHYMENA* AXONEMES FOR CRYO-ET ..... - 86 -
3.1.1 Growth of Tetrahymena strains CU428 and CFAP77A/B-KO ..... - 86 -
3.1.2 Cilia purification from Tetrahymena strains CU428 and CFAP77A/B-KO..... - 86 -
3.1.3 Intact axoneme preparation from purified Tetrahymena strains CU428 and CFAP77A/B-KO cilia ..... - 86 -
3.2 METHODS – CRYO-ET SAMPLE PREPARATION OF *TETRAHYMENA* CILIA ..... - 87 -
3.3 METHODS – CRYO-ET DATA COLLECTION ..... - 88 -
3.4 METHODS – CRYO-ET DATA PROCESSING ..... - 89 -
3.5 METHODS – COARSE-GRAINED MOLECULAR DYNAMICS SIMULATIONS AND ANGULAR ELASTICITY ..... - 91 -
3.6 METHODS – CFAP77 GENE KNOCK-INS AND KNOCK-OUTS IN *TETRAHYMENA* ..... - 92 -
3.7 METHODS –PHENOTYPIC AND LOCALIZATION STUDIES OF *TETRAHYMENA* WILD-TYPE AND CFAP77-KO MUTANT STRAINS ..... - 93 -
3.8 METHODS – QUANTIFICATION OF POLYGLUTAMYLATION IN *TETRAHYMENA* WILD-TYPE AND CFAP77-KO MUTANT STRAINS .. - 94 -
3.9 RESULTS AND DISCUSSION ..... - 95 -
3.9.1 Overview of the Tetrahymena outer junction proteins..... - 95 -
3.9.2 Structural evidence for CFAP77 and OJ2 stabilizing the Tetrahymena outer junction..... - 98 -
3.9.3 Molecular dynamics demonstrate that CFAP77 and OJ2 stabilize the outer junction ..... - 105 -
3.9.4 CFAP77A and CFAP77B paralogs differentially localize in Tetrahymena cilia..... - 107 -
3.9.5 Knockout of CFAP77 reduces Tetrahymena swimming and cilia length ..... - 108 -
3.9.6 Knockout of CFAP77 disrupts the structure of the Tetrahymena axoneme ..... - 112 -
3.9.7 Knockout of CFAP77 in Tetrahymena is associated with higher tubulin polyglutamylation levels..... - 115 -

CHAPTER 4: GENERAL DISCUSSION AND CONCLUSION..... - 120 -

4.1 AXONEMAL *TETRAHYMENA* DMT AND MIPS ..... - 120 -
4.2 *TETRAHYMENA* DMT MIPS AND MAPS HAVE A 96-NM REGISTRY ..... - 120 -
4.3 *TETRAHYMENA* DMT IS DECORATED WITH PG-RICH MOTIF PROTEINS ..... - 121 -
4.4 TETRAHYMENA MAPS OVERLAP WITH TRACKS FOR IFT MOTOR PROTEINS..... - 122 -
4.5 CFAP77 AND OJ2 STABILIZE THE OUTER JUNCTION OF DMTS IN *TETRAHYMENA* ..... - 123 -
4.6 CFAP77 IS NOT ESSENTIAL FOR DMT ASSEMBLY OR SWIMMING IN *TETRAHYMENA* ..... - 125 -
4.7 A TUBULIN PTM CODE REGULATES DMT STABILITY AND INTERACTING PROTEINS IN CILIA..... - 127 -
4.8 CONCLUSION ..... - 128 -

REFERENCES ..... - 130 -

List of Figures and Tables

Figure 1.1. Electron micrographs and drawings of cilia from mussel-gill epithelium.....22
Figure 1.2. Cilia and flagella, the axoneme, and doublet microtubules.....24
Figure 1.3. The DMT in cilia.....30
Figure 1.4. Cartoon representation of the axoneme, axonemal DMT, and microtubule inner proteins.....34
Figure 1.5. Examples of cryo-EM sample preparation, data collection, and data processing.....39
Figure 2.1. Cryo-EM sample preparation and representative electron micrographs.....44
Figure 2.2. Visualization of side-chain densities of MIPs and crosslinks with tubulin.....56
Figure 2.3. Paralogs and unique conformations of Tetrahymena MIPs. (A-H) Structural comparisons of paralogs and unique conformations of Tetrahymena MIPs.....59
Figure 2.4. The structure of the native DMT from *Tetrahymena*.....61
Figure 2.5. Comparison of the DMT structure from *Tetrahymena*, Chlamydomonas and bovine respiratory cilia.....65
Figure 2.6. MIPs in *Tetrahymena* exhibit a 96-nm periodicity.....71
Figure 2.7. The outer surface filaments on the native DMT.....74
Figure 2.8. Anterograde and retrograde trains use different microtubules of the same DMT, which may be regulated by microtubules associated proteins such as MAP7. 76
Figure 2.9. The outer surface filament presents steric clashes with dynein and kinesin.....80
Figure 3.1. The Tetrahymena outer junction is occupied by the conserved CFAP77 and species-specific OJ2.....93
Figure 3.2. Structural evidence for CFAP77A and OJ2 stabilizing the outer junction.....97
Figure 3.3. CFAP77A and OJ2 hypothesized to interact with the C-terminal tails of β-tubulin through electrostatic interactions at outer junction. Cleavage of C-terminal tails of β-tubulin allow for partial doublet formation in vitro. 98
Figure 3.4. Sperm-MIPs at the ribbon interact with tubulin C-terminal tails.....100
Figure 3.5. CFAP77 stabilizes the outer junction. 101
Figure 3.6. Molecular dynamics simulations of CFAP77A and OJ2.....103
Figure 3.7. Knockout of CFAP77A/B caused mild defects in Tetrahymena cilia.....105
Figure 3.8. Knockout of CFAP77A/B caused mild defects in cilia.....107
Figure 3.9. Cilia in the CFAP77A/B-KO mutant have a slightly higher level of tubulin glutamylation.....109
Figure 3.10. Knockout of CFAP77A/B caused mild defects in cilia.....110
Figure 3.11. Cilia in the CFAP77A/B-KO mutant have a slightly higher level of tubulin glutamylation.....112
Figure 3.12. A model of the role of CFAP77 on the formation of the B-tubule.....114

Table 2.1. Cilia Wash and Final Buffers used for *Tetrahymena* cilia purification.....43
Table 2.2. Cryo-EM data collection and refinement parameters for all datasets used in this thesis.....54
Table 2.3. Identification of Tetrahymena proteins based on side chain fitting of our cryo-EM map.....57
Table 2.4. Species-specific MIPs in Tetrahymena, Chlamydomonas and Bovine cilia.....62
Table 2.5. Mass spectrometry analysis of wild type (WT), RIB72B and RIB72A/B knockout mutants showing the missing proteins.....69
Table 3.1. Antibodies used in this thesis. 91

Abstract (English)

Cilia and flagella are tentacle-like cellular appendages that are the biological basis for cellular motility and have existed since the last eukaryotic common ancestor. The cytoskeleton of cilia and flagella is the axoneme, a microtubule-based (MT) structure that consists of a complete 13- protofilament A-tubule and a partial 10- protofilament B-tubule. Motor proteins and various protein linkages generate force and sliding between doublet microtubules (DMTs) that lead to bending and motility. In the lumen of DMTs are a network of microtubule inner proteins that act as a stabilizing sheath against the mechanical stresses induced by the dynein motor arms and ciliary bending.

Here, I show that the 48-nm repeat of the native *Tetrahymena thermophila* DMT contains at least 28 evolutionarily conserved microtubule inner proteins, 13 microtubule inner proteins unique to parasitic ciliates, and filamentous microtubule-associated proteins on the outer surface. Sample preparation and mapping the architecture of the DMT was a team effort of which I was heavily involved. I then performed structural analyses and literature review to discover that the evolutionarily conserved CFAP77 and species-specific OJ2 proteins stabilize the outer junction region (OJ) of the axonemal DMT. Based on the results I gathered, collaborators performed molecular dynamics simulations on the OJ of the DMT, as well as genetic engineering to knock out CFAP77 in *Tetrahymena*. I then performed cryogenic electron tomography sample preparation, data collection, tomographic reconstructions, and subtomogram averaging of DMTs from wild-type and mutant strains. I analyzed the results and discovered that CFAP77 stabilizes the

axonemal DMT but is not necessary for assembly or motility. Loss of CFAP77 results in shorter cilia that beat and swim slower.

I also present several interesting areas with which to continue this research. Analysis of the reconstructed tomograms revealed that loss of CFAP77 resulted in an increase in tubulin polyglutamylation and the appearance of additional densities at the OJ of the axonemal DMT. This raises fundamental questions about the role of tubulin post-translational modifications in the constitution of the DMT and the axoneme.

Abstract (French)

Les cils et les flagelles sont des appendices cellulaires ressemblant à des tentacules qui constituent la base biologique de la motilité cellulaire et existent depuis le dernier ancêtre commun des eucaryotes. Le cytosquelette des cils et des flagelles est l'axonème, une structure à base de microtubules (MT) qui se compose d'un tubule A à 13 protofilaments complet et d'un tubule B, incomplete, à 10 protofilaments. Des protéines motrices et diverses liaisons protéiques génèrent une force et un glissement entre les doublets de microtubules (DMT) qui entraînent la flexion et la motilité. Dans le centre des DMT se trouve un réseau de protéines internes des microtubules qui agissent comme une gaine de stabilisation contre les contraintes mécaniques induites par les bras moteurs de la dynéine et la flexion ciliaire.

Ici, je montre que l'unité de répétition de 48 nm du DMT natif de Tetrahymena thermophila contient au moins 28 protéines internes des microtubules conservées sur le plan évolutif, 13 protéines internes des microtubules uniques aux parasites ciliés, ainsi que des protéines filamenteuses associées à la surface externe des microtubules. La préparation des échantillons et la cartographie de l'architecture du DMT ont été réalisées grâce à un effort d'équipe auquel j'ai largement participé. J'ai ensuite effectué des analyses structurales et une revue de la littérature pour découvrir que les protéines CFAP77 sont conservées sur le plan évolutif et que la protéine OJ2 est spécifique chez Tetrahymena et stabilise la région de la jonction externe (OJ) du DMT axonémal. Sur la base des résultats que j'ai obtenus, mes collaborateurs ont réalisé des simulations de dynamique moléculaire sur l'OJ du DMT, ainsi que de l'ingénierie génétique pour éliminer CFAP77

chez Tetrahymena. J'ai ensuite préparé des échantillons pour la tomographie électronique cryogénique, collecté des données, reconstruit les tomogrammes et obtenu la moyenne des sous-tomogrammes de DMTs provenant de souches sauvages et mutantes. J'ai analysé les résultats et découvert que CFAP77 stabilise le DMT axonémal mais n'est pas nécessaire pour l'assemblage ou la motilité. La perte de CFAP77 entraîne des cils plus courts qui battent et nagent plus lentement.

Je présente également plusieurs domaines intéressants pour poursuivre cette recherche. L'analyse des tomogrammes reconstruits a révélé que la perte de CFAP77 entraînait une augmentation de la polyglutamylation de la tubuline et l'apparition de densités supplémentaires au niveau de l'OJ du DMT axonémal. Cela soulève des questions fondamentales sur le rôle des modifications post-traductionnelles de la tubuline dans la constitution du DMT et de l'axonème.

Acknowledgments

This thesis was supported by CIHR funding from my supervisor's fund (Dr. Khanh Huy Bui, CIHR PJT-156354), as well as a Centre de recherche en biologie structural (CRBS) Studentship Award from 2021-2022.

To my supervisor Dr. Khanh Huy Bui, I thank for his world-class supervision. Dr. Bui's transparent and direct nature fostered an honest and effective research environment. In addition to learning technical and professional skills, I attended several workshops and conferences where I was able to build a network and plan future career moves.

I thank my mentor Dr. Dieter Reinhardt and committee members Dr. Alba Guarné and Dr. Susanne Bechstedt for their guidance, critical thinking, and honest feedback.

I would also like to thank Dr. Kelly Sears, Dr. Kaustuv Basu, Dr. Mike Strauss, and Dr. Joaquin Ortega of FEMR for their mentorship, training, and expertise. I would not have been able to collect a single dataset without them.

I thank past and present members of the Bui Lab (Dr. Thibault Legal, Avrin Ghanaeian, Phuong Huynh, Dr. Muneyoshi Ichikawa, Dr. Sky Yang, Ahmad Khalifa, Daniel Dai, and Katya Peri) for their training, collaborations, conversations, and friendship.

Melissa Valente-Paterno was instrumental in the success and efficiency of the Bui lab, all green lab initiatives, and surviving the Strathcona Anatomy and Dentistry Building.

My family - Shane, Colleen, Stella, Lois, Joel, Olivia, Ellie, Weston, Kuru chi, Wakame, Wasabi, Bode Bear (forever in my heart), and the Hayata's – were more supportive, generous, and loving than they will ever know.

I dedicate this thesis to the memory of Lorelie Black.

Preface

Contributions to original knowledge

I contributed to both published and unpublished work included in this thesis. The published work is found in the two following publications:

I Black CS, Dai DC, Peri K, Ichikawa M, Bui KH. Preparation of Doublet Microtubule Fraction for Single Particle Cryo-electron Microscopy. 2021 *Bio-protocol* 11(11): 10.21769/BioProtoc.4041.

II Kubo S, Black CS, Joachimiak E, Yang SK, Legal T, Peri K, Khalifa AAZ, Ghanaeian A, McCafferty CL, Valente-Paterno M, De Bellis C, Huynh PM, Fan Z, Macotte EM, Wloga D, Bui KH. 2023. Native doublet microtubules from *Tetrahymena thermophila* reveal the importance of outer junction proteins. *Nat Commun* 14: 2168.

In the first manuscript, I changed and optimized several methodologies that have since been adopted by several other groups in the field. I designed a more efficient and effective workflow for the growth and harvesting of *Tetrahymena thermophila* strains. I optimized the conditions for the purification of intact, membranated cilia from *Tetrahymena* cells; the purification of intact, crosslinked axonemes from cilia; and the purification of intact doublet microtubules (DMTs) from axonemes. I also optimized the sample preparation and data collection for both single particle cryogenic electron microscopy and cryogenic electron tomography. This effort has helped improve the workflow for all groups studying *Tetrahymena thermophila* cilia, and the peer-review process made it clear that it was useful.

In the second manuscript, I performed all the cryo-EM and cryo-ET sample preparation, and with the assistance of FEMR, I participated in data collection. In parallel with my supervisor Dr. Khanh Huy Bui, I actively processed all the cryo-EM and cryo-ET data. In parallel with my supervisor Dr. Khanh Huy Bui and postdoctoral fellow Dr. Shintaroh Kubo, I actively modeled and helped identify several microtubule inner proteins. In this way, I contributed to our understanding of the molecular architecture of the *Tetrahymena* DMT. I performed structural analyses to find structural evidence that the microtubule inner proteins CFAP77 and OJ2 stabilize the outer junction region (OJ) of the DMT. I also contributed toward data analyses, discussion points, literature review, bioinformatics, and manuscript writing.

In that manuscript, I made several contributions to original knowledge. I contributed to several findings in the manuscript including modeling and identifying novel microtubule inner proteins. It was previously unknown what, if any, proteins were present at the OJ of DMTs in cilia and flagella. I showed that there were two of them in *Tetrahymena thermophila* and that one of them is evolutionarily conserved.

Detailed contributions of each author

I actively participated in all aspects of the experiments, excluding molecular dynamics simulations conducted by postdoctoral fellow Dr. Shinataroh Kubo (Bui lab, McGill University); *in situ* crosslinking mass spectrometry conducted by the laboratory of Dr. Edward M. Marcotte (University of Texas, Austin, USA); and the genetic engineering and related quantification of *Tetrahymena* knockout strains conducted by the laboratory of Dr. Dorota Wloga (Nencki Institute of Experimental Biology, Poland).

In Kubo *et al.*, 2023, Corbin Black (me) greatly contributed to *Tetrahymena* growth, cilia purification, mass spectrometry sample preparation and data analysis, cryo-EM/ET sample preparation, cryo-EM/ET grid screening, cryo-EM/ET data collection, cryo-EM/ET data processing, protein structure modeling, and general data analyses.

Shintaroh Kubo and Shun Kai Yang greatly contributed to cryo-EM data processing and protein structure modeling. Shintaroh Kubo also performed all molecular dynamics simulations. Thibault Legal and Avrin Ghanaeian contributed to the processing and analysis of the cryo-ET data and subtomogram averaging. Katya Peri contributed to the sample preparation and analysis of mass spectrometry data. Ahmad Khalifa previously contributed to modeling and structural analysis of many MIPs that were used in model building. Chelsea De Bellis, Zhe Fan, and Phuong M. Huynh contributed to cryo-EM data processing and wrote some of the scripts used in data processing. Melissa Valente-Paterno contributed to culturing, storage, and growth of all *Tetrahymena* strains. Caitlyn L. McCafferty and Edward M. Marcotte performed all *in situ* crosslinking mass spectrometry. Ewa Joachimiak and Dorota Wloga performed all genetic engineering and related quantification of *Tetrahymena* knockout strains. Khanh Huy Bui conceptualized, advised, analyzed data, and contributed toward cryo-EM data processing and protein structure modeling. The publication was written by Khanh Huy Bui, Corbin Black(me), and the Wloga lab.

In Black *et al.*, 2021, Corbin Black (me) and Muneyoshi Ichikawa greatly contributed to method development. Daniel Chen Dai and Katya Peri contributed toward some of the

methods development. The publication was written by Khanh Huy Bui, Corbin Black (me) and Muneyoshi Ichikawa.

List of abbreviations and terms used in this thesis.

ADP	Adenosine diphosphate. In the context of inner and outer dynein arms, the ADP-bound state represents a microtubule-bound state after hydrolysis and phosphate release. Also used during purification of doublet microtubules from intact axonemes.
ATP	Adenosine triphosphate. In the context of inner and outer dynein arms, the ATP-bound state represents a microtubule-bound state prior to hydrolysis. Also used during purification of doublet microtubules from intact axonemes.
Axoneme	Cytoskeleton of the cilia that includes 9 DMTs connected by nexin linkers, inner and outer dynein arms, nexin-dynein regulatory complexes, radial spoke proteins, and central pair microtubules.
CFAP	Cilia and flagellar associated protein.
Cilia	Hair-like organelle that beats and generates motility or fluid flow.
Cryo-EM	Cryogenic electron microscopy.
Cryo-ET	Cryogenic electron tomography.
DMT	Doublet microtubule.
GTP	Guanosine triphosphate. In the context of microtubules, GTP is hydrolyzed by β-tubulin during polymerization of β-and α-tubulin heterodimers into microtubules. Also used in the *in vitro* polymerization of microtubules.
IFT	Intraflagellar transport.
FAP	Flagellar associated protein.
Flagella	Hair-like organelle that beats and generates motility or fluid flow.
MAP	Microtubule associated protein (external to microtubule).
MIP	Microtubule inner protein (internal to microtubule).
MT	Microtubule
OJ	Outer junction region (of the axonemal doublet microtubule).
PF	Protofilament
PTM	Post-translational modification

Introduction, rationale and research objectives

Introduction

Cilia and flagella are tentacle-like cellular appendages found across the tree of life and have existed since the last eukaryotic common ancestor.[1] These organelles are functionally motile or nonmotile. Motile cilia and flagella allow unicellular organisms to swim and multicellular organisms to generate fluid flow. Nonmotile or primary cilia are integral to cell signaling, mechanosensing, and breaking left-right symmetry during embryonic development.[1-3]

Defects in cilia are known as ciliopathies and are associated with diseases throughout the human body, including brain malformation, hearing loss, hepatic disease, infertility, mental retardation, organ laterality defects, respiratory diseases, retinal dystrophy, and skeletal anomalies.[4] There are hundreds of different molecules in every cilium and flagellum.[5] Understanding how those molecules interact will provide fundamental insight into evolutionary adaptations of motile organisms and provide a model for ciliopathies.

Inside the ciliary membrane is a microtubule-based cytoskeleton known as the axoneme. The axoneme consists of nine doublet microtubules (DMTs) arranged in rings that are connected by flexible linkers and that surround two singlet microtubules (MTs) in the center. Several other protein complexes and motor proteins are attached to the DMTs that generate shear force, sliding of DMTs, and bending of DMTs that are all part of motility.

The DMT resembles a figure-eight and consists of a complete 13- protofilament (PF) A-tubule and a partial 10-PF B-tubule attached to the A-tubule at two sites. The DMT has

two junctions connecting the two tubules, which are the two structurally weak points.[6] Thus, the stability of DMT is dependent upon the stability of the two junctions. Inside the lumen of both the A- and B-tubules are networks of interconnected microtubule inner proteins (MIPs) that stabilize the DMT against mechanical stresses.[6-8]

Cryogenic electron microscopy (cryo-EM) and data processing techniques have advanced tremendously over the last decade. Cryo-EM has been used to obtain countless cryo-electron microscopy density maps of macromolecular assemblies in their native and biologically active state. A cryo-EM density map is then used to build models of the atomic structures of the various components of the macromolecular assembly. The 2017 Nobel Prize in chemistry was awarded to Jacques Dubochet, Joachim Frank and Richard Henderson for their contributions to the field. In 2020, two separate research groups used cryo-EM on well-studied protein complexes to demonstrate that the technique is capable of producing density maps that have atomic resolution information.[9,10] The only other techniques capable of providing that level of structural resolution were X-ray crystallography and electron crystallography.[11] Cryo-EM has been employed with great success for the identification and structure determination of multi-megadalton dynamic protein complexes that include the nuclear pore complex,[12] ribosomes[13,14], and spliceosomes.[15] Cryo-EM has also been used to determine various structures of axonemal DMTs from *Chlamydomonas reinhardtii* flagella,[16] *Tetrahymena thermophila* cilia,[17,18] and mammalian respiratory cilia[19] and sperm.[20]

Rationale

Cryo-EM studies of DMTs in the axonemes of cilia and flagella have so far provided an incomplete architecture of MIPs inside DMTs. In addition, we lack knowledge on the molecular mechanism behind DMT assembly. Conventional electron microscopy studies of basal body assembly in paramecia showed that the A-tubule is first assembled, and then the B-tubule begins to form on the A-tubule where the A-tubule faces towards the ciliary membrane.[21] This region corresponds to the outer facing junction of the DMT.

Tetrahymena thermophila is a parasitic ciliate and has been an effective model organism for chromosome and chromatin biology, programmed genome rearrangement, secretion, cytoskeletal research, and more.[22] I chose to study *Tetrahymena* because it is amenable to genetic engineering,[22,23] it is evolutionarily distinct from both green alga and mammals,[24] it shares thousands of orthologs with humans, and it is abundant in cilia.[24] Accordingly, I wanted to use cryo-EM and complementary approaches to try to explain the molecular mechanism of DMT assembly using *Tetrahymena* as a model organism. My hypothesis was that there are proteins important for formation of the DMT and that these proteins are located at the OJ.

The research objectives of this thesis are as follows:

I Obtain a high resolution cryo-EM map of the doublet microtubule from axonemes of *Tetrahymena* cilia.

II Model the molecular architecture of the *Tetrahymena* DMT, compare the *Tetrahymena* DMT with DMTs from other species, and identify proteins at the outer junction region of the DMT.

III Study one or two outer junction MIPs to understand their function in cilia.

Chapter 1: Literature Review

1.1 Cilia and flagella

Cilia and flagella are tentacle-like cellular appendages found across the tree of life and have existed since the last eukaryotic common ancestor.[1] They can be largely separated into two groups: motile and nonmotile. Cilia and flagella have been integral to the success and evolution of almost all eukaryotic organisms. There have been ciliary/flagellar loss events multiple times across the tree of life, but those instances are incredibly rare.[25] Some unicellular organisms swim by using their one or two "flagella" that generate an undulating, wave-like motion.[26] "Cilia" typically refer to abundant surface extensions on protists and eukaryotes that are either motile or nonmotile.[27] Motile cilia generate a beating, whip-like waveform to either drive fluid flow or to drive cellular motility.[28] Nonmotile or primary cilia serve as chemical or mechanical sensors and function in the transduction of Hedgehog signaling.[29,30]

In mammals, there are several cell types throughout the body that have cilia or flagella. In early developing mammalian embryos, motile cilia at the node cavity generate leftward flow of extra-embryonic fluid that is sensed by immotile cilia of peri-nodal crown cells.[31] Bending of the mechanoresponsive crown cilia activates a signal cascade that leads to symmetry breaking on the left-right axis and subsequent left-right asymmetric development.[32] In the brain ventricular system[33,34] and central canal of the spinal cord,[35] ependymal cilia drive cerebrospinal fluid flow. The circulation of cerebrospinal fluid throughout the brain and spinal cord is integral to the development and migration of stem cells and general nervous system homeostasis.[36-38] In the epithelium of the mammalian

middle ear, multiciliated cells clear mucus from the middle ear cavity to the nasal cavity.[39,40] In the respiratory tract, ciliated epithelial cells beat in a metachronal pattern to clear gases, particulates and pathogens that have been dissolved or entrapped in mucus.[41,42] Last, mammalian sperm cells are propelled through the female reproductive tract by a flagellum.[43]

1.2 Ciliopathies

Any genetic disease associated with a mutated, truncated, or deleted ciliary protein that causes ciliary dysfunction is a ciliopathy. Ciliopathies arise from defects in motile and nonmotile ciliary activity. Nonmotile (primary) cilia have diverse sensory and signaling roles and are distributed throughout the body; mutations to the genes that encode that primary ciliary machinery can result in ciliopathies that affect a single tissue or several organs simultaneously.[44] Primary cilia in the kidney function to sense urinary flow and osmolarity.[45] Defects in fluid flow sensing or calcium transduction alter the differentiation of surrounding renal tubule epithelial cells and lead to polycystic kidney disease and nephronophthisis.[45] In embryonic ciliated cells, primary cilia are integral to Hedgehog signal transduction.[29] Hedgehog signaling is essential for the development of organs such as the eyes, lung, muscle, and skin.[46] Mutations that affect Hedgehog signaling can lead to severe developmental diseases.[29,46] Nonmotile ciliopathies are often caused by mutations or deletions in genes associated with signal transduction, such as ciliary membrane receptors that bind signal molecules, intraflagellar transport trains that carry receptors and signaling molecules from/to the cell, or the BBSome complex that functions

as a cargo adapter for signaling molecules such as G-protein coupled receptors or the smoothened protein.[29,47]

Ciliopathies resulting from dysfunction in motile cilia are classified as Primary Ciliary Dyskinesia (PCD).[48] PCD is a rare genetic disorder associated with chronic ear infections, chronic upper and lower respiratory tract infections, laterality defects (such as heterotaxy syndrome and *situs inversus*), and male infertility.[48] Unsurprisingly, most mutations associated with PCD cause dysfunction or dissociation of the inner and outer dynein motor proteins that are the force generators for ciliary beating.[49] Most of the remaining ciliary genes with PCD-linked mutations are interaction hubs for the ciliary cytoskeleton and are important for coordinating ciliary beating.[49]

In mammalian sperm cells, the normal non-planar and asymmetric beating waveform is occasionally broken by planar flagellar waves.[50] The mechanism of waveform modulation in mammalian sperm cells is not well understood, but it is thought that the sperm flagella cytoskeleton and sperm head may be involved.[51] Interestingly, the cytoskeleton of cilia and flagella is generally highly conserved across the tree of life.

1.3 *Tetrahymena thermophila* as a model organism

One of the advantages of studying a conserved biological system such as cilia and flagella is the option to study a model organism. The nematode *Caenorhabditis elegans* is an excellent model for studying kidney disease because the same proteins that are involved in kidney functions are associated with mechanosensation and signal transduction in *C. elegans*.[52] *Xenopus* is a useful model organism to study cilia during the development of a vertebrate organism because there are many different types of motile and primary cilia

that can be studied, and biological and imaging techniques are well established.[53] Zebrafish have recently been shown to possess motile cilia near their olfactory pit and are thus an appropriate model organism to study PCD using genetics and electron microscopy techniques.[54] Drawbacks to working with more complex organisms include difficult genetic engineering and physical differences between each specimen. Studying the unicellular green alga *Chlamydomonas reinhardtii* and the free living parasitic ciliate *Tetrahymena thermophila* has led to discoveries related to chromatin biology, endocytosis, meiosis, nuclear pore complex, phagocytosis, photosynthesis, response to stimuli, ribosomes, RNA enzymes, the cytoskeleton, and, of course, ciliary/flagellar motility.[22]

Why use *Tetrahymena thermophila* to study cilia and flagella? A single *Tetrahymena* cell is covered in over 1000 cilia that they rely on for motility and survival. There are methods to isolate cilia and flagella from cells, and the yield from an easily prepared *Tetrahymena* culture would be 500 times greater than *Chlamydomonas reinhardtii* and 1000 times greater than a mammalian sperm cell.[55] *Tetrahymena* is a ciliate with a transcriptionally silent germline genome in a micronucleus[56] and an expressed somatic genome in macronuclei.[24] Another advantage of *Tetrahymena* as a model organism is that germline and somatic genomes have been targeted for genetic engineering using different approaches including mutagenesis,[57] forward genetics,[58] homologous recombination,[59] and CRISPR–Cas9-mediated genome editing.[60]

As you will see in the next section, the cytoskeleton of *Tetrahymena* cilia looks essentially identical to the cytoskeleton of humans and mammals. Furthermore, many of the proteins involved in cellular organelles and processes that are present in both *Tetrahymena* and humans are conserved.[24] In fact, there are more orthologs shared between humans and *Tetrahymena* than humans share with the yeast *Saccharomyces cerevisiae* or *Tetrahymena* shares with the parasitic protozoan *Plasmodium falciparum*, despite the phylogenetic relationship between *Tetrahymena* and humans being much farther apart than animals and fungi or ciliates and apicomplexans.[24] With 2280 orthologs present in humans, the ciliate Tetrahymena is a powerful model organism to study cilia and flagella in both ciliates and mammals.[24]

1.4 Architecture of the cilium and the axoneme

In the 1950s and 1960s, Irene Manton, Keith Porter, and Peter Satir used electron microscopy to show that inside cilia and flagella is a cytoskeleton consisting of long double filaments anchored by a basal body and rootlet structures (Fig. 1.1). [2,61,62] Remarkably, almost 70 years ago, these men determined that motile cilia, including algal flagella, mollusk epithelial cilia, and mammalian sperm, have a “9+2” double filament arrangement and that sensory cilia found in insects and invertebrates have a “9+0” arrangement. [2,61,62]

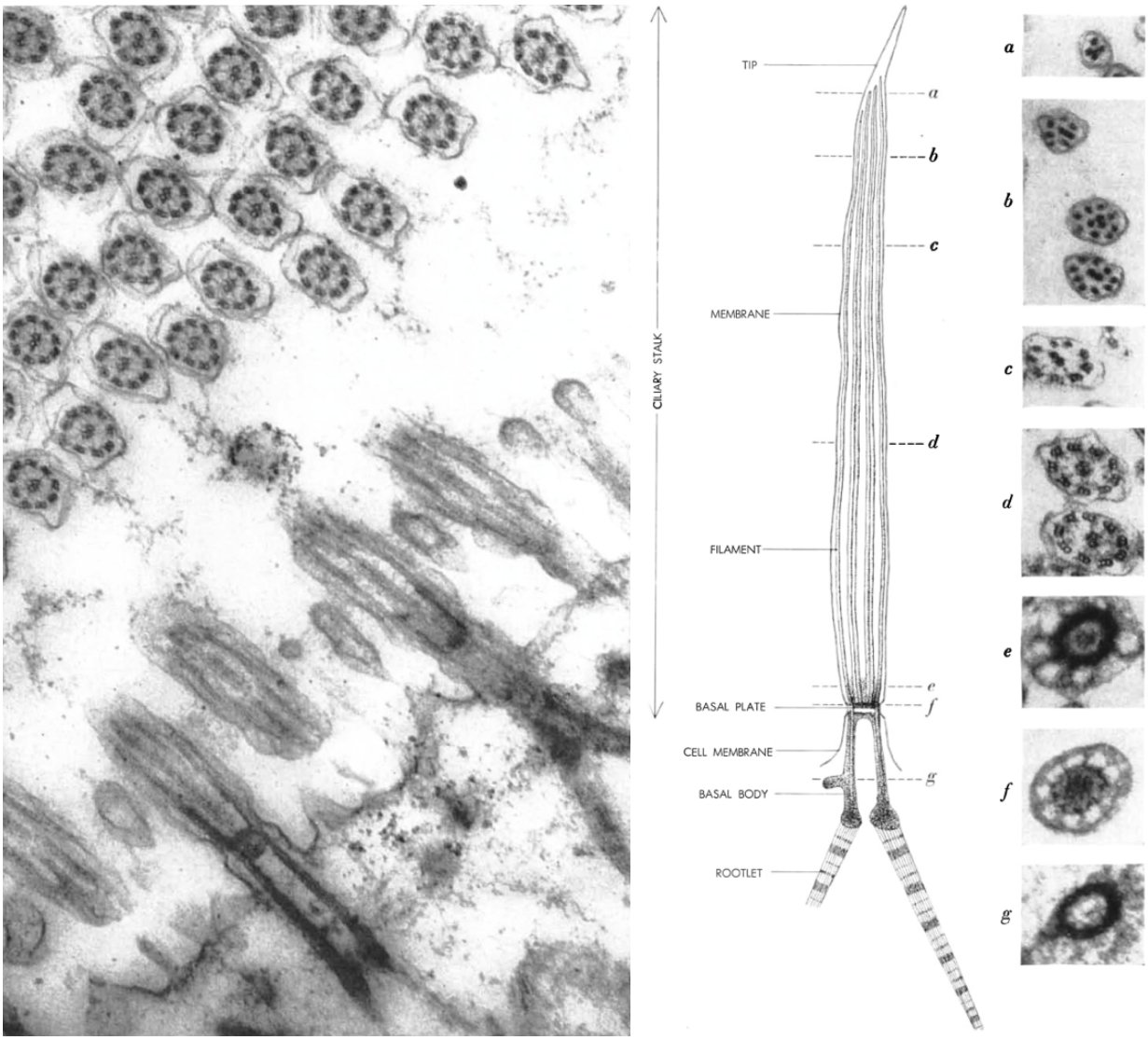

Figure 1.1. Electron micrographs and drawings of cilia from mussel-gill epithelium. ***Left:*** *(upper left) cross-section of epithelial cilia and 9+2 arrangement of double filaments (MTs) surrounding two central filaments (central pair). (bottom right) Longitudinal sections of ciliary stalks with rootlets, basal body that transition to filaments and membrane that extend from the cell surface.* ***Right:*** *drawing of a longitudinal view of a cilium accompanied by corresponding electron micrographs of epithelial cilia. These images were adapted from Satir, 1961.*[2]

Briefly, basal bodies formed from centrioles fuse with vesicles at the distal end and form a "vesicle cap" as they migrate to the cell membrane surface.[63] Rootlets that extend toward the nucleus and stabilize the eventual cilium are attached to the basal body at the proximal end (Fig. 1.1).[2] Then, the vesicle-capped basal body docks to the actin-rich

cortex.[63] The vesicle cap fuses with the cell membrane; the ciliary membrane is continuous with the cell membrane, but the ciliary membrane is made from different lipids and receptors that are specific to ciliary signaling and function.[63-65] From the distal end of the basal body, the C-tubule does not extend, and only DMTs continue from the A- and B-tubules (Fig. 1.2A, B). The DMTs extend from the basal body for approximately 70 nm and then become part of the transition zone (Fig. 1.2D). The transition zone contains an inner stellate fiber structure and outer Y-links that interconnect the DMTs and connect them to the ciliary membrane; in doing so, the transition zone also imposes a structural blockade on the cilium that gates ciliary traffic (Fig. 1.2D).[66] After the stellates and Y-links terminate, the DMTs are enveloped in a ~76-nm long protein sleeve before transitioning to the axoneme.[66]

Cilia and flagella are supported by a microtubule-based cytoskeleton called the axoneme (Fig. 1.2A-C). The axoneme predominantly consists of nine DMTs, nexin linkages, inner and outer dynein motors, radial spoke complexes, nexin-dynein regulatory complex, and central pair MTs.[27,67,68] Beyond the axoneme, outermost MTs cease, and singlet MTs continue to the tip (Fig. 1.1).[2]

A

Motile cilia across exist across the tree of life:

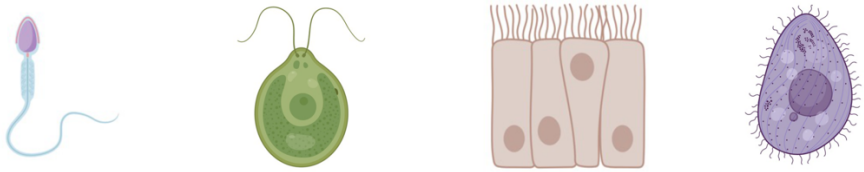

Mammalian sperm | *Chlamydomonas reinhardtii* | Mammalian respiratory epithelial cells | *Tetrahymena thermophila*

B

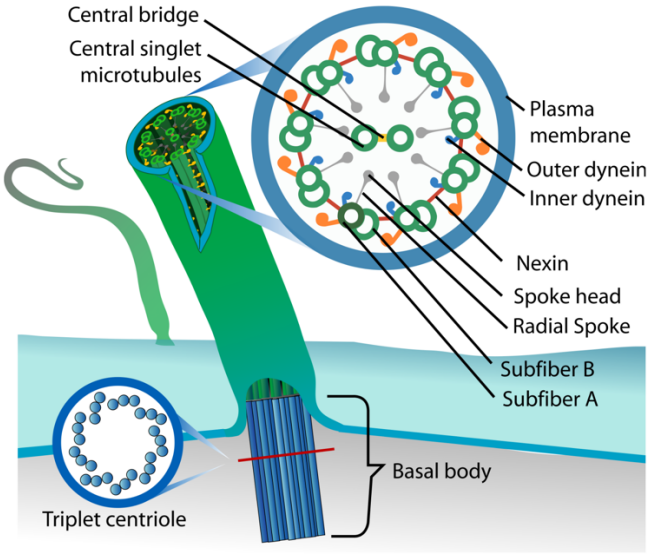

C

In situ structure of 96-nm repeat unit of *Tetrahymena* ciliary axoneme (EMD-9023):

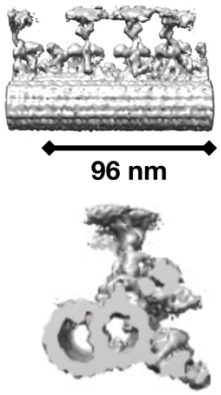

D

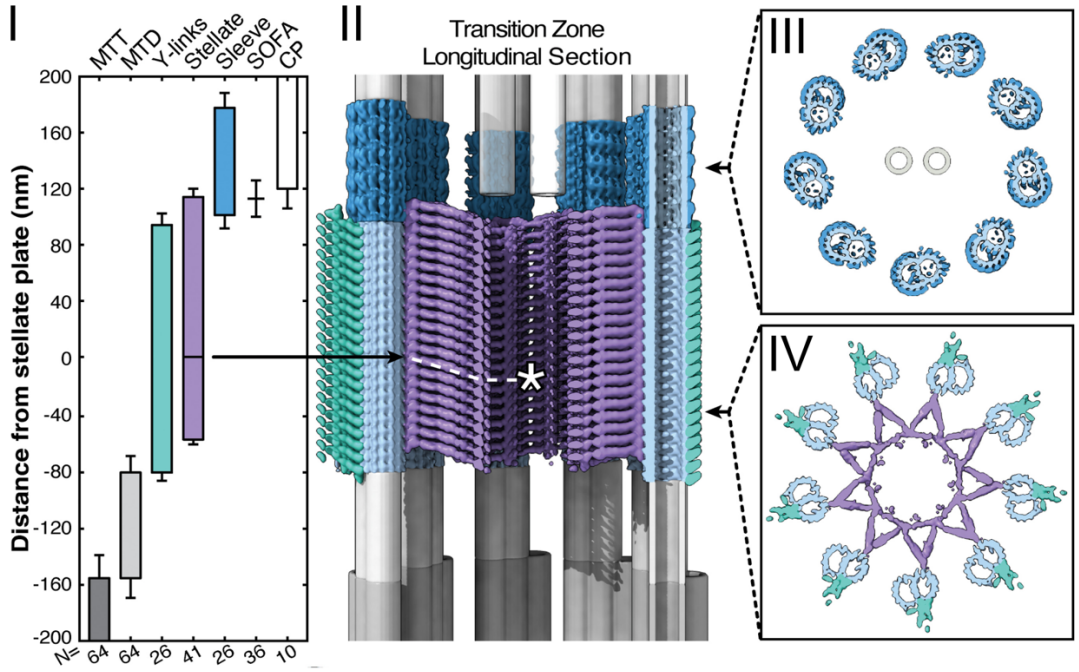

Figure 1.2. Cilia and flagella, the axoneme, and DMTs. (A) Examples of flagella in mammalian sperm and *Chlamydomonas reinhardtii* as well as cilia in mammalian airway epithelial cells and *Tetrahymena thermophila*. **(B)** Graphical depiction of a cilium. A ciliary membrane envelops 9 DMTs linked by nexin that surround 2 central pair MTs. The inner and outer dynein arms connected to the A-tubule of one DMT transiently walk along the neighboring B-tubule. Radial spoke proteins extend from the inner-facing A-tubules and transiently interact with the central pair of MTs. From Wikimedia Commons, the free media repository. **(C)** Cryo-EM map of the 96-nm repeating unit of an intact axonemal DMT from *Tetrahymena* with associated radial spoke proteins and inner and outer dynein motor arms with resolution up to 12 Å.[68] **(D)** *In situ* cryo–electron tomography revealed the native structures of the transition zone region in *Chlamydomonas*. (I) Position of the transition zone relative to the basal body and axoneme. Distances are measured relative to the stellate plate (see Fig. S6), defined as the "0 nm" origin point. SOFA, site of flagellar autotomy, where the cilium is cleaved (see Figs. S6 and S7). CP, central pair. Error bars indicate standard deviation. (II) Longitudinal section view of the complete composite model, assembled according to the measured lengths and positions of each component, with 21 Y-link repeats, 21 stellate repeats (7 proximal of the plate, 14 distal), and 5 DMT sleeve repeats. (III-IV) Cross-sectional views through the indicated regions of the composite model, showing (III) DMTs encased in the helical sleeve, with the CP in the middle, and (IV) the nine-pointed stellate cylinder attached to DMTs decorated with Y-links. Adapted from Den Hoek *et al.*, 2022.[66]

1.5 Doublet microtubules and tubulin post-translational modifications

β- and α-tubulin heterodimers are the building blocks of the cytoskeleton of the cell. Tubulin is a major component of ciliary structure and function,[2,61,62] cell division,[69] cell shape,[70] and intracellular trafficking.[71] Depending on the cellular process, tubulin may require different properties, such as stability, high dynamicity, recruitment, and repulsion of MT-interacting elements.[72]

In cilia, axonemal DMTs are made from tubulin protofilaments (PFs). DMTs consist of a 13-PF complete "A-tubule" MT and a partial 10-PF "B-tubule" MT built atop the A-tubule (Fig. 1.3). Thus, there are two points where the B-tubule is anchored to the A-tubule: the inner and outer junctions (Fig. 1.3). The junctions are named as such because they describe how the inner junction faces toward the center of the axoneme and the outer

junction faces the ciliary membrane (Fig. 1.2 and Fig. 1.3). Early electron microscopy studies of basal body formation in paramecium[21] and rhesus monkey oviduct epithelial cells[73] revealed that the A-tubule is first formed, followed by sequential assembly of the B- and C-tubules.[21,73] Assembly of the B- and C-tubules occurs at the outer-facing region of the A-tubule.[21,73] Almost 50 years later, the Guichard and Hamel lab showed that partial DMTs can be assembled *in vitro*.[74] If MTs were polymerized *in vitro*, then treated with the protease subtilisin to cleave the β- and α-tubulin C-terminal tails, the addition of fresh tubulin to those MTs resulted in formation of partial B-tubules that resembled the outer junction.[74] Taken together, these studies suggest that the outer junction is the site of DMT assembly.

DMTs function as structural support for the organelle, a scaffold for accessory complexes, and tracks for intraflagellar transport (IFT) in motile and nonmotile cilia.[75] DMT sliding and bending are the mechanisms for the initiation and propagation of ciliary bending in motile cilia.[76] Tubulin and MTs are evolutionarily conserved across animals, fungi, and plants; so too are the lateral and longitudinal interactions that stabilize MTs.[77] MTs are subject to bending, compressive and tensile mechanical stresses.[78] A microtubule protofilament is a series of β- and α-tubulin heterodimers arranged in a head-to-tail fashion (Fig. 1.3A,B). The head-to-tail interactions are longitudinal, while interactions between tubulin subunits of neighboring PFs are lateral.

Longitudinal interactions consist of intradimer interactions between β- and α-tubulin subunits and interdimer interactions between an α-tubulin subunit of a heterodimer on the growing end and a β-tubulin subunit of the heterodimer behind it.[79] Prior to polymerization,

β- and α-tubulin subunits each bind to a Mg^{2+} ion and subsequently a GTP molecule.[80] Upon binding these cofactors, the tubulin heterodimer adopts a conformation that favours PF and MT assembly.[81] Once incorporated into the MT, the β-tubulin subunit catalyzes GTP hydrolysis and releases the phosphate group and the Mg^{2+} ion. The α-tubulin subunit only binds to the Mg^{2+} ion and GTP cofactor and does not have enzymatic activity.[82] The GDP-bound state of β-tubulin is associated with weak interdimer interactions and MT instability.[82] Thus, GTP hydrolysis affects MT dynamics.[82]

Lateral interactions between adjacent tubulin PFs provide MT resistance to mechanical stresses (Fig. 1.3B,C). Canonically, a loop between β-sheet 7 and α-helix 9 called the M-loop (microtubule loop) extends outward laterally from every β- and α-tubulin subunit along a PF and interacts with an α-helix (H3) and two loops (H2-S3 and H1-S2) of the adjacent tubulin subunit (Fig. 1.3C).[79]

Post-translational modifications are covalent and enzymatic modifications of proteins. Post-translational modifications of tubulin modify MT stability and behavior and include acetylation, phosphorylation, polyamination, detyrosination, polyglycylation, and polyglutamylation.[72] Acetylation of lysine 40 of an unstructured loop on α-tubulin is associated with tubulin lattice flexibility and increased MT stability, but it remains unclear whether it is the cause or the result.[83] Acetylation of lysine 40 limits the structural conformations that the unmodified loop would otherwise sample.[83]

Phosphorylation of tubulin by various kinases multimodally regulates MT behaviour. Tyrosine phosphorylation of α-tubulin prevents incorporation of free tubulin heterodimers into growing MT s in human T lymphocytes.[84] Similarly, phosphorylation of serine 172 of

β-tubulin inhibits incorporation of tubulin into polymers.[85] Phosphorylation of an unidentified residue(s) on the carboxyl (C)-terminus of β-tubulin isotype III is required for polymerization *in vitro* in a microtubule-associated protein MAP2-dependent manner.[86]

Polyamination of glutamine residues in tubulin by transglutaminases is associated with increased MT nucleation and stability *in vitro*.[87] Neuronal tubulin purified from human and mouse brains both revealed that glutamine 15 of β-tubulin was polyaminated.[87] Furthermore, purified neuronal MTs that are polyaminated are highly stable and resistant to destabilizing treatments including cold and antimitotic drugs.[87,88]

Detyrosination by carboxypeptidases exclusively occurs on the C-termini of post-polymerized α-tubulin subunits.[89,90] Detyrosinated α-tubulin differentially localizes along neuronal MTs: tyrosinated α-tubulin is concentrated at growth cones while detyrosinated α-tubulin is localized to the proximal axonal regions.[91] In sea urchin sperm, detyrosinated α-tubulin is predominantly found on the B-tubule of axonemal DMTs.[92] While detyrosination does not directly affect MT stability,[93] it does regulate activity of kinesin motor proteins[94] and affinity of microtubule-associated proteins (MAPs) as the plus-end tracking protein EB1.[95]

Polyglycylation is catalyzed by tubulin tyrosine ligase-like glycylases that link variable glycine chains to glutamine residues near the C-terminal tails of β- and α-tubulin.[96] Polyglycylation exclusively modifies axonemal tubulin found in cilia and flagella.[97] Polyglycylation of glutamine residues on the C-terminal tails of β-tubulin is essential for DMT and axonemal assembly and motility in *Tetrahymena*.[98] In human epithelial cells,

polyglycylation regulates ciliary beating.[99] One of the proposed functions of polyglycylation is to counter and inhibit polyglutamylation in cilia.[100]

Polyglutamylation is catalyzed by tubulin tyrosine ligase-like glutamylases.[101] Like polyglycylation, polyglutamylation targets the glutamine residues near the end of C-terminal tails of β- and α-tubulin but instead adds variable glutamine chains.[102] Polyglycylation and polyglutamylation target the same C-terminus glutamine residues of axonemal tubulin but polyglutamylation is also abundant in centrioles[103] and neurons.[104] Polyglutamylation introduces more electronegativity to the MT surface and thus affects the recruitment of various MT-interacting proteins. Polyglutamylation selectively increases activity of kinesin motor proteins[105] and katanin severing enzymes.[106] Polyglutamylation has also been shown to increases the recruitment of diverse MAPs such as glycogen synthase kinase 3 and tau.[107] By recruiting MT-interacting proteins such as severing enzymes or MAPs that affect MT dynamics, polyglutamylation indirectly regulates MT dynamics and stability.

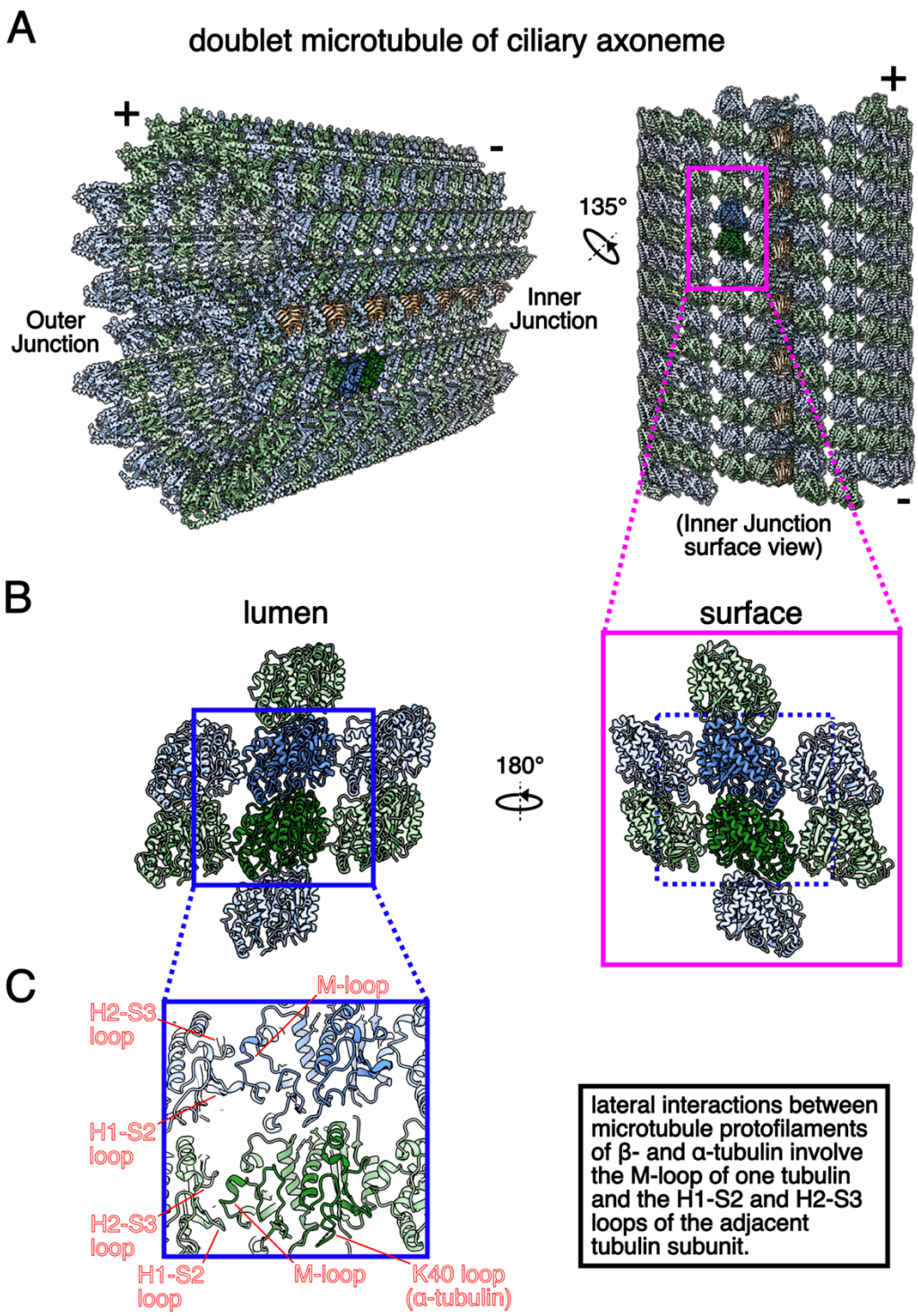

Figure 1.3. DMT in cilia. (A) The DMT of the ciliary axoneme. Microtubule protofilaments consist of β- and α-tubulin heterodimers arranged head-to-tail. **(B)** The DMT lattice is stabilized by lateral interactions between adjacent tubulin subunits. **(C)** The canonical tubulin lateral interaction involves the microtubule loop, or M-loop, of one tubulin subunit and the H1-S2 and H2-S3 loops of the adjacent subunit.[79] (+) and (–) signs indicate the plus (distal) and minus (proximal) ends of the DMT.

Attached to the DMTs are inner and outer dynein motor proteins, radial spoke complexes, and nexin-dynein regulatory complexes that are required for motility.[108] The power stroke of the inner and outer dynein arms generates sliding between neighboring DMTs.[109] During ciliary beating, cilia violently whip and bend; consequently, DMTs are constantly under high shear forces and bent conformations.[78] Thus, the stability of DMTs is integral to cilia function. Inside each DMT is a network of interconnected microtubule inner proteins (MIPs) that appear to form a stabilizing sheath.[6-8] MIPs likely act as a stabilizing sheath that provides the structural integrity necessary to withstand the dynein motor arm-induced mechanical stresses that act on the MT lattice.[6-8]

1.6.1 Microtubule-associated proteins

Microtubule-associated proteins (MAPs) bind to the surface of the MT and often change the properties of that MT. MAPs may change the stability, growth rate, catastrophe rate, or recruitment of motor proteins.[110,111] MAPs have important roles in various diseases, including cancer and neurodegenerative disorders.[112] For example, plus-end tracking end-binding (EB) proteins have an N-terminal calponin homology domain that binds to MT plus-ends and a C-terminal coiled-coil domain that mediates dimerization and interaction with other proteins.[113] EB-family proteins are overexpressed in various types of cancer and play important roles in tumor progression and metastasis.[114] EB-family proteins also play important roles in the development and maintenance of neuronal synapses, and their dysregulation has been linked to various neurodegenerative disorders, such as Alzheimer's disease and Huntington's disease.[115] The tumor overexpressed gene (TOG) family has been shown to promote MT assembly by

stabilizing the ends of growing MTs or promoting nucleation.[116] TOG/XMAP215 family proteins have been implicated in various developmental disorders, such as microcephaly and ciliopathies, which are characterized by abnormal MT organization and function.[117]

The katanin family of MT severing enzymes function to regulate cytoskeletal MT dynamics and length.[118] Dysregulation of katanin is associated with defective cell migration, cell proliferation, and cell shape.[119,120] In cilia, katanin function to sever old and post-translationally modified tubulin segments.[121] Gene knockout of katanin in *Tetrahymena* results in inhibition of polyglycylation and polyglutamylation, shorter cilia, and immotility.[121] Tau forms dynamic condensates along neuronal MTs that act as selectively permissive barriers to motor proteins involved in axonal transport and protect against MT-severing enzymes.[122] Tau is implicated in several neurodegenerative diseases, including Alzheimer's disease, where it accumulates in the form of insoluble aggregates.[123] Tau is permissive to dynactin-activated dynein motor proteins[122] but inhibits kinesin-1 and kinesin-3 motor proteins.[124,125] MAP9 inhibits the dynein-dynactin-BicD complex and kinesin-1 but is permissive to kinesin-3 due to a positively charged K-loop motif of kinesin-3.[111] MAP7 is essential for kinesin-1 transport in *Drosophila*.[126]

There are hundreds of cytosolic MAPs.[127-129] The mitotic spindle protein CKAP2 has recently been shown to help nucleate MT growth and increase the stability of polymerized MTs.[130] MAPs have also been shown to differentially affect the landing and processivity of dynein and kinesin motor proteins.[111] Dynein and kinesin motor proteins move along MTs and transport cargos to different subcellular locations. Kinesin and dynein motor proteins are involved in various cellular processes, including mitosis, intracellular

transport, neuronal development, and IFT.[131] Motor proteins have MT binding domains for landing and processivity, motor domains for ATP hydrolysis, which generates mechanical force, a coiled-coil domain that mediates dimerization and cargo binding, and a tail domain that determines the specificity of cargo binding.[132] In cilia, kinesin motor proteins transport cargo to the ciliary tip during anterograde transport, and dynein motor proteins transport cargo from the tip to the cell body during retrograde transport.[133] Diffusion can only sustain cilia length for a very short distance; consequently, ciliary development is dependent upon IFT.[134] Dr. Wallace Marshall's laboratory suggests that cilia length is dependent upon the rates of assembly and disassembly and that as cilia length increases, the rate of assembly decreases until they become equal.[135]

In *Chlamydomonas reinhardtii*, mutations to the genes that encode FAP59 or FAP172 resulted in cells with short immotile flagella.[136] Biochemical and cryogenic electron microscopy studies revealed that FAP59 and FAP172 proteins form a complex, localize to the cilia, are required for cilia length, and define the 96-nm periodicity by which all ciliary components are arranged.[136] The mammalian homologs of FAP59 and FAP172 and CCDC39 and CCDC40, respectively. Mutations in CCDC39 or CCDC40 are associated with loss of ciliary motility, axonemal disorganization, laterality defects, and primary cilia dyskinesia in dogs, humans, mice, and zebrafish.[137,138] CCDC39 and CCDC40 are examples of MAPs that are essential for axoneme assembly, motile cilia function and are PCD genes.

1.6.2 Microtubule inner proteins

Ciliary DMTs are incredibly stable filaments that must endure changing sliding and bending forces. MTs consist of β- and α-tubulin heterodimers that form PFs which further assemble into a hollow cylindrical structure. Microtubule inner proteins, or MIPs, are a class of proteins that interact with MTs and regulate their stability and isolate damage or defects caused by ciliary bending.[139] MIPs are proteins that bind to the lumen of MTs (Fig. 1.4A, B). Cryogenic electron microscopy (cryo-EM) techniques revealed that DMTs isolated from sea urchin sperm and *Chlamydomonas* flagella contained cryo-EM densities for MIPs.[7,140] At this point in time, there was an abundance of biochemical and mass spectrometry data to suggest potential MIP candidates,[141] but there was no possibility of assigning an identity or building a protein model with the low resolution data. Scientists theorized that these MIPs may be important to stabilize DMTs during ciliary beating.

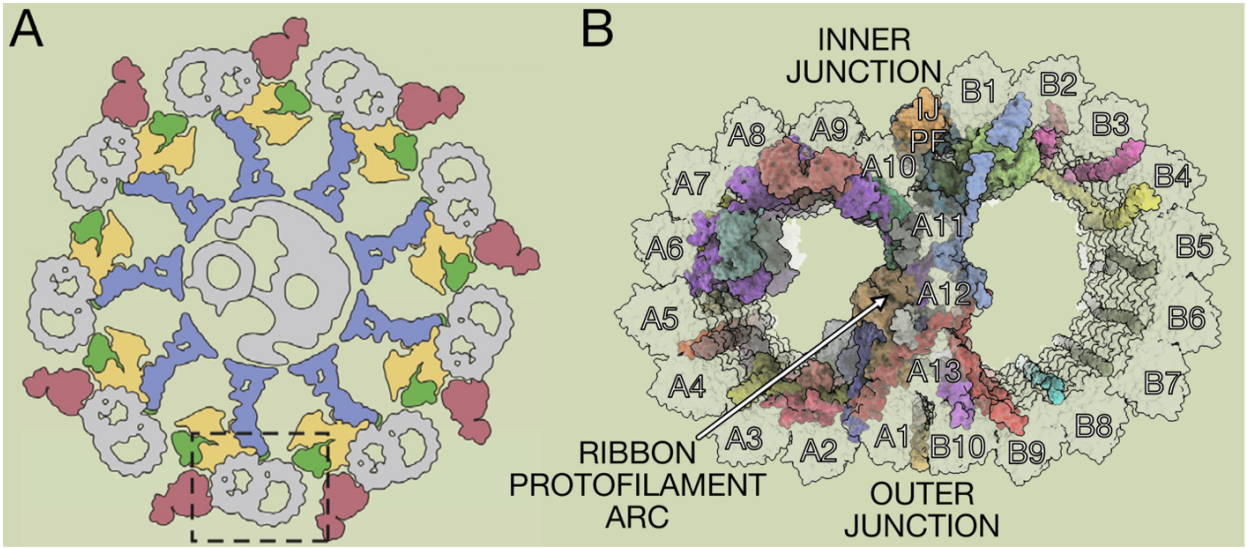

Figure 1.4. Cartoon representation of the axoneme, axonemal DMT, and microtubule inner proteins. (A) Cartoon representation of a cross-section of the axoneme of motile cilia and flagella. Axonemal components are labeled by color: DMTs (gray); outer (red) and inner (yellow) dynein arms; nexin-dynein regulatory complex (green); radial spoke proteins (blue); central pair microtubules (gray). Adapted from Ma *et al*., 2019.[16] **(B)** Cartoon representation of a cross-section of the axonemal DMT. Tubulin protofilaments (A1-A13, B1-B10), inner junction protofilament, ribbon protofilament arc, and inner and outer junctions are labeled. MIPs are colored. Visualization was performed with ChimeraX using model coordinates related to Kubo *et al*., 2023.[142]

MIPs CFAP182A and CFAP182B (Pierce1 and 2 in mammals) are important for outer dynein arm assembly, ciliary motility, and embryonic development in mammals and zebrafish.[16,19] RIB72 (EFHC in mammals) is a conserved ciliary protein with a C-terminal EF-hand domain important for *Tetrahymena* motility[143,144] and is implicated in juvenile myoclonic epilepsy.[145,146] Tektins are a family of mammalian MIPs that localize to the ribbon PF arc region of the axonemal DMT and are involved in the formation and stabilization of the DMTs.[147] Mutations in tektin genes have been linked to several ciliary disorders, including primary ciliary dyskinesia, a genetic disorder characterized by defective cilia that leads to chronic respiratory infections and infertility.[148,149]

In 2017, Muneyoshi Ichikawa and Huy Bui used cryogenic electron microscopy to study MIPs in *Tetrahymena* cilia.[8] They revealed that inside ciliary DMTs is an interwoven network of heterogenous MIPs (Fig. 1.4B). Furthermore, that study showed that MIPs have diverse structural domains, are positioned throughout both tubules of the DMT, and occur with different periodicities along the length of the cilium.[8] In 2019, the Bui lab published the first atomic model of a MIP bound to the lumen of a DMT.[17] In that study they showed that two MIP variants, RIB43A-short and RIB43A-long, bind to the A-tubule and regulate tubulin lattice length and curvature.[17] The Bui lab later modelled the

molecular architecture of the inner junction of the DMT, identifying three new MIPs FAP106, FAP126, and FAP276.[18] Together with FAP45 and FAP52, these MIPs stabilize the FAP20/PACRG non-tubulin PF that connects the B-tubule with the A-tubule at the inner junction (Fig. 1.4B). Gene knockout of CFAP45 and CFAP52 destabilizes DMTs and causes a reduced swimming phenotype in both *Tetrahymena* and *Chlamydomonas* cells.[139] In humans, mutations in MIPs such as CFAP52 and PACRG lead to cilia-related diseases.[150] The identities, structures, and localization of more than 40 MIPs from *Tetrahymena*,[17,18,151] *Chlamydomonas*,[16] mammalian respiratory cilia,[19] and mammalian sperm[20] have since been discovered using cryo-EM techniques.

The DMT has both an inner and outer junction, and both of those junctions have atypical and weaker lateral interactions that are vulnerabilities that require stability against shear forces (Fig. 1.4B). Conventional EM studies on basal body formation in paramecia, together with biochemical and cryo-EM studies of *in vitro* partial DMT assembly, provide overwhelming evidence that DMT assembly initiates at the outer junction.[21,74] At the outer junction, β- and α-tubulins from PF B1 of the B-tubule form non-canonical interactions with β- and α-tubulins from PF A10 of the A-tubule (Fig. 1.4).[8] B-tubule formation *in vitro* first requires cleavage of the C-terminal tails of β- and α-tubulins of polymerized singlet MTs by the serine protease subtilisin.[74] In contrast, mammalian C-terminal tails must not be sterically hindered or lack PTMs for cilia function *in vivo*.[152,153]

Cryo-EM studies have provided a structural framework to understand the consequences of mutations to inner junction MIPs. Yet there is a distinct lack of understanding for outer junction MIPs. B-tubule assembly likely requires the C-terminal tails of β- and α-tubulins

of the A-tubule to be suppressed. I hypothesize that there are one or more proteins localized to the outer junction that are responsible for suppression of C-terminal tails of β- and α-tubulins of the A-tubule. These proteins are important for the formation and/or stability of the DMT.

1.7 Cryogenic electron microscopy, data processing, and protein structure modelling

Electron microscopy studies in the 1950s and 1960s provided a general understanding of the ultrastructure of cilia and flagella (Fig. 1.1). Sample preparation of biological material for conventional transmission electron microscopy required dehydration and heavy metal staining.[154] Technological advancements to electron microscopes, next-generation direct-electron cameras, cryogenic sample preparation, and computer systems have improved the resolution and biological information that is obtained from biological samples. Cryogenic electron microscopy (cryo-EM) and cryogenic electron tomography (cryo-ET) coupled with subtomogram averaging are standard techniques to study macromolecular assemblies.[155] These techniques allow for the reconstruction of 3D molecular structures of biological molecules in their native, biologically active states.[156]

Cryo-EM sample preparation and data processing is optimized for every experiment, but there is a general workflow that I will describe very briefly. First, purified biological molecules in a buffer solution are applied to a very thin copper or gold grid that is coated by a layer of carbon (Fig. 1.5A). The sample is then very quickly frozen in a thin layer of vitreous ice.[157] The grid is inserted into an electron microscope and exposed in brief intervals to an electron beam.[158] Electrons that pass through the sample are recorded as 2D projection images using a direct electron detector or other recording medium.[159] The

raw micrographs contain several image artifacts such as electron beam-induced motion that are corrected during data processing.[160,161] At this point, the 2D particle projections appear relatively weak because they have a low signal-to-noise ratio.[160] Highly similar particle projections/orientations are combined to form 2D class averages with a high signal-to-noise ratio.[161] The 2D classes are then assigned angular orientations relative to each other and combined to reconstruct a single 3D cryo-EM map (Fig. 1.5B).[161]

Cryo-EM data processing was historically complicated, requiring many different scripts and programs. All of the different programs were built into an open source program called RELION[162] that has since seen several iterations and improvements.[163] Sjors Schere's lab and Holger Stark's lab both showed in 2020 that with certain protein samples, it is possible to achieve near-atomic resolution with cryo-EM.[9,10]

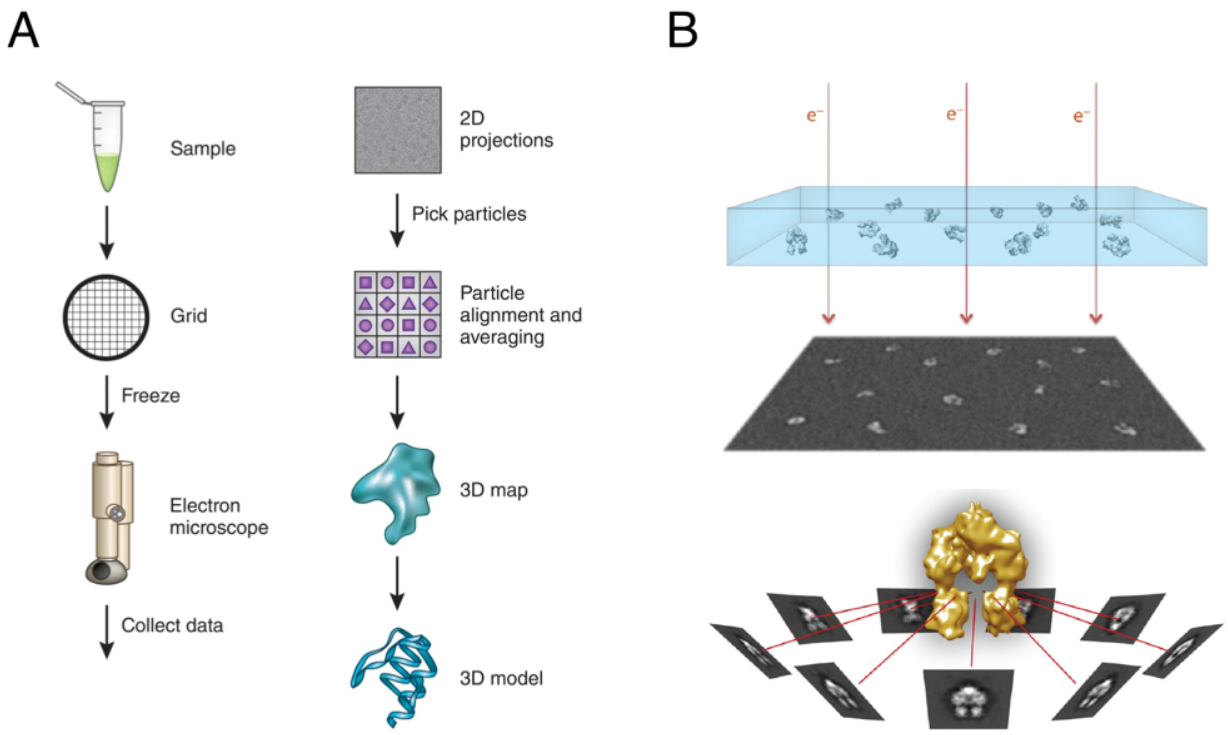

Figure 1.5. Examples of cryo-EM sample preparation, data collection, and data processing. (A) General overview of cryo-EM analysis. Adapted from Doerr, 2016.[164] **(B)** Example of cryo-EM data collection, 2D classification, and reconstruction of a cryo-EM map. Adapted from Skiniotis and Southworth, 2016.[165]

A cryo-EM map represents the space occupied by the corresponding molecule. This map will inform about the relative positions of protein domains, secondary structures, and amino acid sidechains depending on the quality of the resolution of the map. Using various modelling software, an atomic model of the molecule is computationally built inside the cryo-EM map.[161] If the resolution of the cryo-EM map is sufficient, the model of the biomolecule can be built *de novo*.[166] The model is then refined to satisfy stereochemistry restraints of all the atoms of the amino acids of the model.[167,168] But if the resolution of the cryo-EM is too poor, or if the map is ambiguous because of heterogeneity associated with either multiple conformations or paralogous proteins, other strategies must be employed to generate a suitable model. Artificial intelligence (AI) has changed and improved cryo-EM data processing and protein structure modelling. AI-assisted structure modelling is particularly useful for proteins that adopt heterogenous conformations within the same sample. In the context of cilia, there could be paralogous MIPs that adopt similar structures, or a particular MIP adopts unique conformations along the length of the DMT because it interacts with different molecules.

DeepTracer is a software tool predominantly used to automatically generate a backbone model, or polyalanine trace from a user-provided cryo-EM map that can then be used for further structure editing and refinement.[169] AlphaFold2 is AI software that predicts the structure of an amino acid sequence by using a neural network that was trained on over 170,000 deposited models of protein structures.[170,171] DeepTracer-ID is an improvement

on DeepTracer which will predict the structure and sequence of the model of the protein using the user-provided cryo-EM map and then searching the entire AlphaFold2 library for all predicted structures from the user-provided organism identity.[172] FindMySequence is an AI software that will predict the sequence and identity of a protein model using the user-provided backbone trace and cryo-EM map.[173] FindMySequence is also useful for validating the sequence/identity assignment of a protein model determined from any method. ModelAngelo is another neural-network approach to automatically build and predict a complete protein structure using a user-provided cryo-EM map.[174] Lastly, the AI software AlphaLink combines experimentally determined crosslinking mass spectrometry data with AI-predicted protein structure models to better predict protein structures, protein interaction interfaces, and arrangement of multimolecular assembles.[175]

1.8 Advances in doublet microtubule cryogenic microscopy sample preparation

The ideal cryo-EM dataset of DMTs would include high quality micrographs of DMTs sampling all necessary orientations and containing all associated MIPs, MAPs, and MT associated protein assemblies. Historically, two hurdles prevented this from happening: the first was breaking the axoneme into intact DMTs; the second was preferred orientation because DMTs laid flatly in vitreous ice.[176,177] Takashi Ishikawa's group overcame the first hurdle by using well-established protocols to chemically detach cilia from cell bodies, detergent to dissolve the ciliary membrane, and centrifugation to isolate the axonemes.[7] Then they invented a protocol to prepare DMTs for cryo-EM data collection: they added ATP to activate inner and outer dynein motors, which caused the axoneme to fall apart in absence of a basal body and ciliary membrane.[176,177] Unfortunately, technological

restraints at the time combined with preferred orientation meant that it was very difficult to obtain high resolution information.[176,177] Muneyoshi Ichikawa and Huy Bui overcame the preferred orientation problem by using a different approach.[8] Once the intact axoneme was purified, they treated it with high salt to disrupt the protein interactions that held the axoneme together and free the DMTs.[8] The DMTs were dialyzed to dissociate dynein arms from the DMTs then sonicated to break them into shorter segments that were more likely to sample many different orientations.[8] In 2017 they published the first single particle cryo-EM structure of the DMT.[8] The Bui lab would use this method to publish the first structures of MIPs bound to the lumen of *Chlamydomonas* and *Tetrahymena* DMTs using cryo-EM, mass spectrometry, and *de novo* protein structure modelling.[17,18]

There were methods to isolate intact DMTs and methods to prepare DMTs that sampled sufficient orientations, but they had not been successfully combined. In 2019, the Brown and Zhang labs prepared DMTs by treating intact axonemes with both ATP and the protease subtilisin.[16] They published a high resolution structure of the DMT from *Chlamydomonas* but the sample preparation resulted in digestion and dissociation of protein assemblies attached to the DMT surface.[16] In 2020, there was no high resolution cryo-EM model of an intact DMT. Technological advancements in electron microscopes, improvements in DMT sample preparation, complementary techniques such as crosslinking mass spectrometry, and AI-guided protein structure modelling would fundamentally change our understanding of the DMT.

Chapter 2: Molecular architecture of the DMT of *Tetrahymena thermophila*

In this chapter, I present research focused on the molecular architecture of the DMT from *Tetrahymena* axonemes. I used a combination of cryo-EM, mass spectrometry, and artificial intelligence to model the *Tetrahymena* DMT. I found filamentous and globular proteins present at various periodicities in the lumen of the DMT as well as filamentous proteins along the outer surface of the DMT. Generally, MIPs are thought to be integral for the stability of the DMT, while filamentous proteins on the surface interact with IFT motor proteins.

I helped develop certain methodologies from this chapter that have been published in the journal Bio-Protocol Journal.[178] Much of the results and discussion have been published in the journal Nature Communications.[142] The reason the methods paper was published is that I can prepare axonemal DMTs in their native state with all microtubule-bound protein complexes intact. Studying native DMTs using cryo-EM is necessary to obtain cryo-EM densities for weakly associated proteins that would dissociate with exposure to high salt or mechanical disruption. In addition, my method to purify intact DMTs led to the reconstruction of other intact subcomplexes on the surface of the DMT from the Bui lab such as the outer dynein arms[179] and nexin-dynein regulatory complex.[180]

2.1 Methods – Sample preparation of *Tetrahymena* DMTs for mass spectrometry analysis and cryo-EM

2.1.1 Growth of *Tetrahymena* strain CU428

Tetrahymena strain *CU428* (*Tetrahymena* Stock Center #SD00178) was stored as bean media with the assistance of Melissa Valente-Paterno.[181] I inoculated 40 mL of SPP

media (1% proteose peptone, 0.1% yeast extract, 0.2% glucose, 0.0003% FeEDTA) with 10 μL of bean media in a 250 mL Erlenmeyer flask. I let the culture grow on the bench at room temperature for approximately one week, observing the culture on a glass slide under a light microscope daily. I then transferred 2 mL of the one week 40 mL *Tetrahymena* culture to 100 mL of SPP media in a 500 mL Erlenmeyer flask and grew overnight with shaking at 150 rpm and 30°C in a Thermo Fisher Scientific MAXQ8000 shaker incubator. The following morning, I transferred 100 mL of overnight culture to 750 mL SPP media in a 2 L Erlenmeyer flask and grew for approximately 48 hours with shaking at 150 rpm and 30°C in a Thermo Fisher Scientific MAXQ8000 shaker incubator. I harvested the culture when the measured optical density (OD_{600}) was 0.6-0.8 AU. I performed several preparations so that there was an abundance of sample for cryo-EM data collection and 3 individual biological replicates for mass spectrometry analyses (for both salt washed, and non-salt washed preparations, see below).

2.1.2 Cilia purification from *Tetrahymena* strain *CU428*

Once the *Tetrahymena* culture was ready to harvest, I poured it into a 1 L Beckman Coulter JLA 8.000 centrifuge tube. The culture was centrifuged for 15 minutes at 1000 x g and 20°C using a Beckman Coulter Avanti J-20 XP. The cell pellet was delicate, so I carefully discarded the supernatant, resuspended the cell pellet in fresh SPP media to a total volume of 24 mL and transferred the culture to a 250 mL Erlenmeyer flask. The *Tetrahymena* culture was ready for deciliation through dibucaine treatment (Fig. 2.1A).[178] I added 1 mL of SPP media supplemented with 25 mg dibucaine and proceeded to gently swirl the dibucaine-treated culture for 1 minute. I then immediately added 75 mL of ice-

cold SPP media supplemented with 0.5 mM EGTA to dilute and slow the dibucaine activity. I then split the 100 mL dibucaine-treated culture into two 50 mL conical tubes (VWR) and centrifuged for 10 minutes at 2000 x g and 4°C in a Thermo Fisher Scientific Sorvall ST 16R. Using a pipet gun, I aspirated the cilia-containing supernatant without disturbing the mucus and cell debris layers under the supernatant. I transferred the supernatant to two Beckman Coulter JA 25.50 centrifuge tubes and centrifuged for 45 minutes at 25000 x g and 4°C using a Beckman Coulter Avanti J-20 XP. I aspirated the supernatant and gently washed away the thin mucus film around each pellet with a few hundred microliters of ice-cold Cilia Wash Buffer (Table 2.1). I resuspended each pellet in 250 μL ice-cold Cilia Wash Buffer and combined them both in a 1.5 mL microcentrifuge tube. I centrifuged the tube for 10 minutes at 700 x g and 4°C using an Eppendorf Centrifuge 5415 D and then transferred the cilia-containing supernatant to a clean 1.5 mL microcentrifuge tube. The intact membranated cilia were snap-frozen in liquid nitrogen and stored in a -80°C freezer.

Table 2.1. Cilia wash and final buffers used for *Tetrahymena* cilia purification.

Component	Cilia Wash Buffer	Cilia Final Buffer
HEPES, pH 7.4	50 mM	50 mM
$MgSO_4$	3 mM	3 mM
EGTA	0.1 mM	0.1 mM
DTT	1 mM	1 mM
Sucrose	250 mM	-
Trehalose	-	0.5%

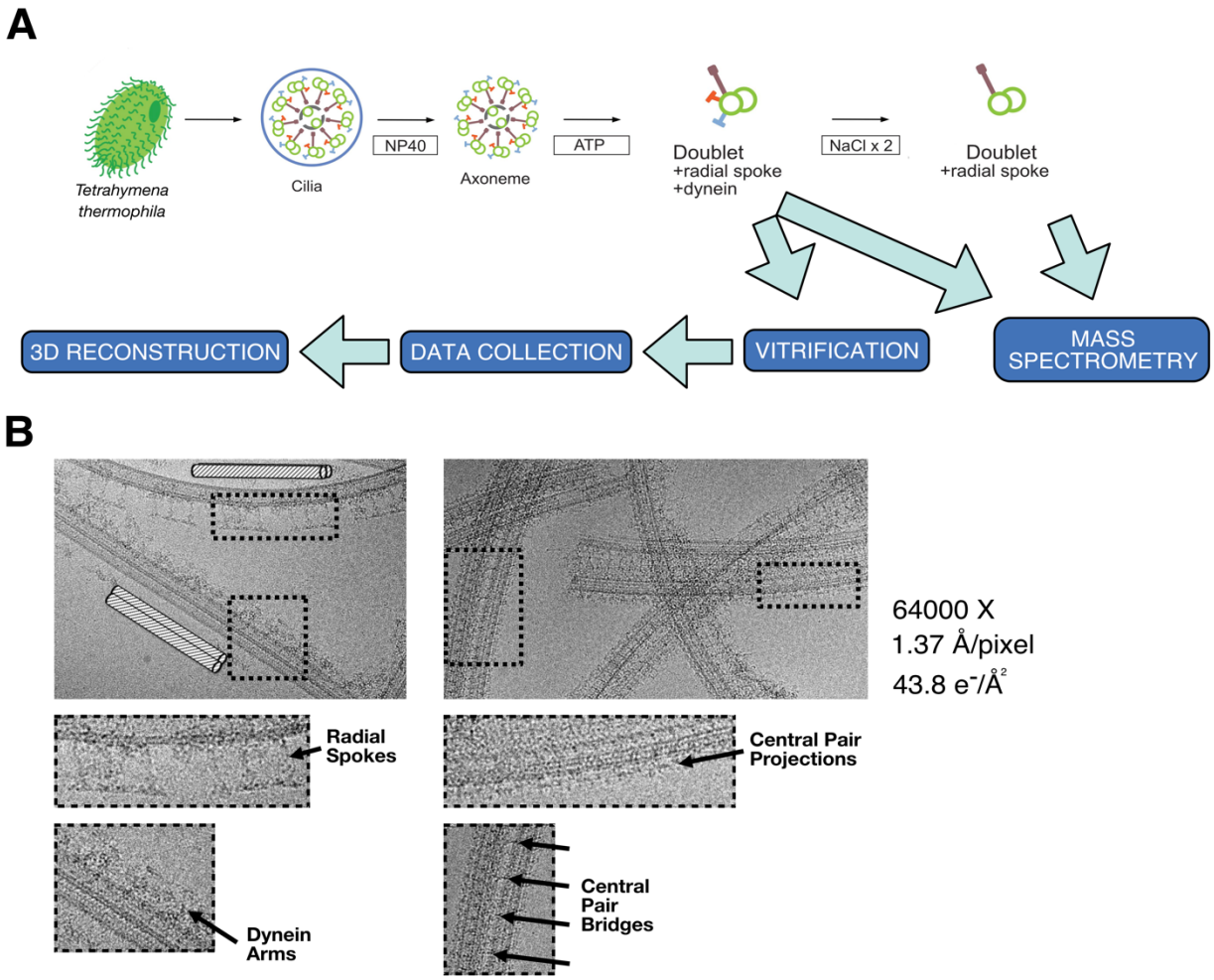

Figure 2.1. Cryo-EM sample preparation and representative electron micrographs. **(A)** Workflow for cryo-EM sample preparation of *Tetrahymena* axonemal DMTs. **(B)** Representative raw electron micrographs from the dataset used to reconstruct the 48-nm native axonemal DMT from *Tetrahymena* strain *CU428*. Adapted from Black *et al.*, 2021.[178]

2.1.3 DMT preparation from purified *Tetrahymena* cilia

The snap-frozen, membrane-bound cilia were thawed on ice and centrifuged for 10 minutes at 7800 x g and 4°C using an Eppendorf Centrifuge 5415 D, and the Cilia Wash Buffer supernatant was removed. I resuspended the pellet in 250 μL Cilia Final Buffer (Table 2.1) and added 44.1 μL 10% NP-40 alternative (final concentration 1.5%) then incubated the sample for 30 minutes on ice to de-membranate the cilia (Fig. 2.1). I then

centrifuged the sample for 10 minutes at 7800 x g and 4°C using an Eppendorf Centrifuge 5415 D, resuspended in fresh 250 μL Cilia Final Buffer, added 44.1 μL 10% NP-40 alternative, and incubated once more on ice for 30 minutes. I centrifuged the sample, resuspended the intact axoneme pellet in 247 μL of Cilia Final Buffer, added 2.5 μL of ADP to a final concentration of 0.3 mM and incubated it at room temperature for 10 minutes to activate dynein motor proteins, induce MT sliding, and disassemble the axoneme into intact DMTs (Fig. 2.1A). I then added 2.5 μL of ATP to a final concentration of 0.1 mM and incubated it at room temperature for 10 minutes for complete axoneme disassembly (Fig. 2.1A).

2.1.4 Salt treatment for mass spectrometry analyses of DMTs purified from *Tetrahymena* strain *CU428* cilia

This step was only performed for mass spectrometry analysis of salt washed DMTs. For cryo-EM and mass spectrometry sample preparation of fully intact DMTs, please skip to Methods 2.1.5.

I centrifuged the intact DMTs (post ADP and ATP treatment) for 10 minutes at 7800 x g and 4°C using an Eppendorf Centrifuge 5415 D and resuspended the DMTs in fresh 250 μL Cilia Final Buffer. I then added 62.5 μL of 3 M NaCl (final concentration 0.6 M) and incubated on ice for 30 minutes to cause separation and loss of proteins bound to the surface of the DMTs, including dynein motor proteins and MAPs. I then centrifuged the sample for 10 minutes at 7800 x g and 4°C using an Eppendorf Centrifuge 5415 D, resuspended in fresh 250 μL Cilia Final Buffer, added 62.5 μL of 3 M NaCl, and incubated once more on ice for 30 minutes. I then centrifuged the sample and resuspended the salt-

treated DMTs in Cilia Final Buffer to a final concentration of 2.2 mg/mL. I measured the total protein concentration by Bradford assay (Bio-Rad) using a Thermo Fisher Scientific 840-208100 UV/Vis spectrophotometer. The sample was then snap frozen in liquid nitrogen and stored in a -80°C freezer until it was sent to the Proteomics and Molecular Analysis Platform at the Research Institute of the McGill University Health Centre (RI-MUHC) for data collection and analysis.

2.1.5 DMT preparation from purified *Tetrahymena* strain CU428 cilia for cryo-EM and non-salt washed mass spectrometry

This section continues from Methods 2.1.3. I centrifuged the intact DMTs (post ADP and ATP treatment) for 10 minutes at 7800 x g and 4°C using an Eppendorf Centrifuge 5415 D and resuspended the DMTs in fresh Cilia Final Buffer to a final protein concentration of 2.2 mg/mL. The DMT sample was then used for vitrification for cryo-EM and mass spectrometry analysis (non-salt washed).

Purification and subsequent ADP- and ATP-driven splitting yielded native axonemal DMT and central pair MTs with associated structures still intact. This methodology has been published in Bio-Protocol Journal[178] and was integral to sample preparation for several projects published in the Bui lab.[142,179]

2.1.6 Mass spectrometry sample preparation of cilia from *Tetrahymena* RIB72 knockout strains *RIB72B-KO* and *RIB72A/B-KO*

Samples for mass spectrometry analysis were also prepared for *Tetrahymena* RIB72 knockout strains *RIB72B-KO* and *RIB72A/B-KO*. *Tetrahymena* cell culturing and harvesting were performed as per Methods 2.1.1. Cilia were purified and stored as per

Methods 2.1.2. Finally, the DMTs were isolated and prepared for mass spectrometry data analysis as per Methods 2.1.3 and 2.1.5.

2.2 Methods – Mass spectrometry data collection of *Tetrahymena* strains *CU428*, *RIB72B-KO*, and *RIB72A/B-KO*

2.2.1 Mass spectrometry data collection of *Tetrahymena* strains *CU428*, *RIB72B-KO*, and *RIB72A/B-KO*

I prepared the DMT samples at 2.2 mg/mL as described above (salt washed and non-salt washed) and sent them to the Proteomics and Molecular Analysis Platform at the Research Institute of the McGill University Health Centre (RI-MUHC) for data collection and analysis. At the proteomics center, each sample (~30 μg of protein) was loaded onto a single stacking gel band for removal of detergents, lipids, and salts. The gel band was reduced with DTT, alkylated with iodoacetic acid, and then digested with the serine protease trypsin. The extracted peptides were solubilized in 0.1% aqueous formic acid and then loaded onto a Thermo Acclaim Pepmap (Thermo, 75 μM ID X 2 cm C18 3 μM beads) precolumn and then onto an Acclaim Pepmap Easyspray (Thermo, 75 μM X 15 cm with 2 μM C18 beads) analytical column separation using a Dionex Ultimate 3000 uHPLC at 250 nl/min with a gradient of 2-35% organic (0.1% formic acid in acetonitrile) over 3 hours. The peptides were then analyzed using a Thermo Orbitrap Fusion mass spectrometer operating at 120,000 resolution (FWHM in MS1) with HCD sequencing (15,000 resolution) at top speed for all peptides with a charge of 2+ or greater. The raw data were converted into *.mgf format (Mascot generic format) for searching using the Mascot 2.6.2 search engine (Matrix Science) against the *Tetrahymena* protein dataset from UniProt. The database search results were imported into Scaffold Q+ Scaffold_4.9.0

(Proteome Sciences) software for statistical treatment and data visualization. I acknowledge the RI-MUHC Proteomics and Molecular Analysis Platform for mass spectrometry data collection as well as assistance with data analysis.

2.2.1 Mass spectrometry data analysis of *Tetrahymena* strains *CU428*, *RIB72B-KO*, and *RIB72A/B-KO*

We (myself, Dr. Bui, Daniel Dai, and Katya Peri) then analyzed mass spectrometry data using Scaffold_4.8.4 (Proteome Software Inc.) software. DMT samples from *Tetrahymena* strains *CU428* (wild-type or WT) and RIB72 knockout strains *RIB72B-KO* and *RIB72A/B-KO* were all analyzed by mass spectrometry. We used peptide counts to screen for MIPs and MAPs. Only proteins with exclusive unique peptide counts of 2 or more in the wildtype mass spectrometry results were included in the data analysis. Raw mass spectrometry data were normalized by total spectra. One-way analysis of variance (ANOVA) was applied to WT, *RIB72A/B-KO* and *RIB72B-KO* mass spectrometry results using biological triplicates. To help identify appropriate MIP candidates, we used emPAI score calculation to filter by molecular weight and distribution/periodicity. We also compared emPAI scores between salt-treated and non-salt-treated samples to identify and exclude proteins that are on the surface of MTs rather than inside.

2.3 Methods – Cryo-EM sample preparation of DMTs from *Tetrahymena* strain *CU428*

All cryo-EM sample preparation, screening, and data collection were performed at the Facility for Electron Microscopy Research (FEMR). Cryo-EM sample preparation, data screening, and data collection would not be possible without the assistance of Dr. Kaustuv Basu (Titan Krios operator) and Dr. Kelly Sears (research manager).

I treated C-Flat Holey thick carbon grids (Electron Microscopy Services #CFT312-100) with chloroform and left them to dry overnight. The grids were negatively glow discharged for 15 seconds at 10 mA (EMS100x Glow Discharge Unit, Electron Microscopy Sciences). Vitrobot Mk IV was used for vitrification (Thermo Fisher Scientific). I applied 4 μL of sample at a concentration of 2.2 mg/mL to the grid, which was subsequently incubated for 15 seconds in a 100% humidity chamber at 22°C. The grid was blotted with a calibrated blot force of 1 for 3 seconds, plunge frozen in liquid ethane and stored in liquid nitrogen.

2.4 Methods – Cryo-EM data collection (single particle analysis)

I screened the samples using an FEI Tecnai G2 F20 200 kV Cryo-STEM (FEMR). The purpose of the screen was to ensure the sample was ready for cryo-EM data collection. There were several important characteristics that I needed to observe before attempting data collection. I was looking for a grid that had a thin layer of vitreous ice, as well as an even and sufficient distribution of DMTs in the holes of the TEM grid. If the ADP/ATP treatment failed, then I would see bundles of axonemes and little to no free DMTs. If the sample was too concentrated, perhaps the vitreous ice would be too thick which reduces high resolution information obtained during data collection; or maybe the high concentration would mean DMTs are overlapping so there are less unobstructed particles for downstream processing. If the sample was too dilute, there might not be enough particles for downstream processing. Once two grids passed the screen, I proceeded with data collection.

Cryo-EM data from screened grids were collected on a Titan Krios 300 keV FEG electron microscope (Thermo Fisher Scientific) equipped with a direct electron detector K3 Summit (Gatan, Inc.) and the BioQuantum energy filter (Gatan, Inc.) and SerialEM software.[182] Micrographs/movies were collected at a magnification of 64000 X, a pixel size of 1.37 Å, a total dose of 45 electrons per $Å^2$ over 40 frames, and a defocus range of –3.0 to –1.0 µm at an interval of 0.25 µm (Table 2.2). We collected 18384 movies that were then processed by single particle analysis to eventually generate a 4.1 Å cryo-EM density map of the 48-nm repeating unit of the DMT from *Tetrahymena* strain *CU428*. Raw micrographs from this dataset reveal native DMTs and central pair MTs with associated protein complexes intact (Fig. 2.1B).

2.5 Methods – Cryo-EM data processing (single particle analysis)

I imported the raw movies into Relion version 3.1[183] and ran motion correction and dose-weighting through the Relion 3.1-integrated MotionCor.[184] The contrast transfer function parameters were estimated using Gctf[185] in Relion 3.1. With enough information about each micrograph, I then discarded those with poor contrast transfer function estimation, drift, and ice contamination.

I manually picked particles from every micrograph using e2helixboxer. Continued processing of these data revealed that my manual picking was suboptimal and provided insufficient data of certain orientations of the DMT. Therefore, the data were repicked using a combination of manual and automatic picking. The 2D views of the DMT-overlapping, or "top," particles were manually picked with e2helixboxer, and the 2D views of the side-by-side particles were automatically picked using Topaz.[186] Topaz had

previously been trained from a dataset containing side-by-side 2D views. The integration of Topaz into my data processing pipeline was done by Dr. Bui and Zhe Fan (undergraduate student). We then converted the Topaz-outputted coordinates into filament coordinates for subsequent processing using custom clustering and line fitting Python scripts written by Dr. Bui that were based on the RANSAC algorithm.

Those filament coordinates were used to extract particles that had 8-nm overlaps from the micrographs with an extraction box size of 512 X 512 pixels. The particles were then binned twice and aligned using the Iterative Helical Real Space Reconstruction script[187] in SPIDER[188] that was modified for non-helical symmetry. We then imported those alignment parameters into Frealign[189] and ran a 6-iteration alignment before converting the aligned particles into Relion 3.1. In Relion 3.1 I ran per-particle defocus refinement and Bayesian polishing steps iteratively for the 8-nm particles. At this point, the particles were very well aligned based on the tubulin dimer densities. Continued processing and refinement steps would yield excellent resolution of the tubulin heterodimers, but further workflow described below were required to obtain high-resolution information about the MIPs, many of which have 48-nm periodicity.

To that end, we subtracted each particle from its tubulin lattice signal and then ran 3D classification with two classes to obtain the 16-nm repeat particles. We ran 3D classification on those 16-nm repeat particles with 3 classes to obtain the 48-nm repeat particles. When I refined the 48-nm particles, I obtained a global resolution of 4.1 Å (Table 2.2). The 48-nm repeating unit of the DMT is a multi-megadalton asymmetric structure and thus requires a local refinement strategy.

I performed focused refinements of different and slightly overlapping regions by using a different mask for each region. Each mask covered approximately 24 nm, 2 PFs and all associated MIPs. After all local refinements were performed, all of the maps were merged into a single composite map using Phenix combine_focused_maps.[190] The composite map was then post-processed with DeepEmhancer software[191] that generated a cryo-EM map with greater interpretability for some local regions. The 48-nm repeating unit cryo-EM map of the DMT from *Tetrahymena* strain *CU428* had a global resolution of 4.1 Å, with some of the locally refined regions having resolutions as high as 3.6 Å (Table 2.2).

2.6 Methods – Protein structure modeling and model validation

The 48-nm cryo-EM with a global resolution of 4.1 Å contained only a few densities suitable for *de novo* protein modeling. Thus, we needed to use multiple approaches to model all tubulin and MIPs. The Bui lab has published several models of *Tetrahymena* β- and α-tubulin.[8,17,18] For tubulin in our model of DMT, I took one previously modeled *Tetrahymena* β- and α-tubulin heterodimer and propagated and refined those models in the 48-nm *CU428* map. For all conserved MIPs, we used homology modeling to obtain initial models. Then, we refined the models in the 48-nm *CU428* map.

For species-specific proteins, the only option for modeling and identification was a *de novo* method. Since this represented many models, the approach could not be traditional (manual polyalanine tracing followed by residue-by-residue mutation) and instead employed artificial intelligence. Species-specific MIPs were modeled using ModelAngelo[174] or DeepTracer[192] software in combination with either ColabFold software[170,193] or FindMySequence software.[173] We first extracted every MIP density from

the 48-nm *CU428* map. For some MIPs, we used ModelAngelo to generate a predicted protein structure model that we manually adjusted with COOT[194] and refined using Phenix Real-space refinement.[190] For other MIPs, we used DeepTracer to generate a backbone (polyalanine) model using that extracted density. We then used ColabFold to first generate AlphaFold-predicted structures for all proteins detected in the DMT from mass spectrometry.

We now had a database of DeepTracer backbone models of every MIP density as well as a database consisting of ColabFold predicted structures of the *Tetrahymena* DMT proteome. We ran the PyMOL cealign program[195] program to find structure matches for all the DeepTracer backbone models from the ColabFold *Tetrahymena* DMT proteome database. We took those ColabFold structure matches for each DeepTracer backbone model and fit them into the corresponding density. Then, we refined those models in the 48-nm *CU428* map. In other cases, we fed the DeepTracer backbone model and the extracted MIP density into FindMySequence software to identify the MIP protein and generate a model with complete sequence and side chains.

We validated all MIP models using both artificial intelligence software and *in situ* cross-linking mass spectrometry. *In situ* cross-linking mass spectrometry was performed by Drs. Caitlyn L. McCafferty and Edward M. Marcotte. We ran FindMySequence on every single MIP model and the corresponding cryo-EM density. We then verified that the hmmsearch[196] E-values for every density and corresponding sequence were below $1x10^{-7}$, which is the cutoff for the probability of correct identity being 95% or greater (Table 2.2).[197] We also used *in situ* crosslinking mass spectrometry data to independently

validate the positioning and fit of all side chains detected in the crosslink data[142] and Marcotte lab [unpublished]. The machine learning algorithm IntPred[198] was used for the prediction of protein-protein interactions.

We were able to model, identify, and validate all tubulin and 41 MIPs in the *Tetrahymena CU428* DMT. Our model represents the most comprehensive 48-nm DMT structure published to date and includes models for MIP paralogs with unique periodicities.

Table 2.2. Cryo-EM data collection and refinement parameters for all datasets used in this thesis. Adapted from Kubo *et al*., 2023.[142]

Method	Single Particle Analysis			Subtomogram Averaging	
Dataset	WT (CU428)	K40R	96 nm combined	WT (CU428)	CFAP77A/B-KO
Microscope	Titan Krios	Titan Krios	Titan Krios	Titan Krios	Titan Krios
Electron Detector	Gatan K3	Gatan K3	Gatan G3	Gatan K3	Gatan K3
Zero-loss filter (eV)	30	30	30	20	20
Magnification	64,000	64,000	64,000	42,000	42,000
Voltage (keV)	300	300	300	300	300
Electron exposure (e/A^2)	45	45 & 73	45 & 73	160	160
Defocus range (μm)	1.0-3.0	1.0-3.0	1.0-3.0	2.5-3.5	2.5-3.5
Pixel size (Å)	1.37	1.37	1.37	2.12	2.12
Tilt range (increment)	-	-	-	-60° - 60° (3°)	-60° - 60° (3°)
Tilt scheme	-	-	-	dose symmetric	dose symmetric
Movies acquired	18,384	25610	43994	-	-
Particles number	148365	182355	172223	-	-
Tilt series acquired	-	-	-	58	20
Subtomograms averaged	-	-	-	2608	1702
Symmetry imposed	C1	C1	C1	C1	C1
Repeat unit (nm)	48	48	96	96	96
Map resolution	3.6 – 4.0	3.3 – 3.5	3.75	19	22

2.7 Results and discussion

2.7.1. Cryo-EM map of the *Tetrahymena* DMT

I needed to obtain a cryo-EM map with the highest possible resolution of the 48-nm repeating unit of the *Tetrahymena CU428* DMT. I performed data processing (single-particle analysis) followed by focused refinements on overlapping regions of the 48-nm

CU428 DMT map to generate a global resolution of 4.1 Å (Table 2.2). Dr. Sky Yang (Bui lab) followed the same workflow with the *Tetrahymena* mutant strain *K40R* to obtain a 3.7 Å resolution map (Table 2.2). The *Tetrahymena* mutant strain *K40R* has a lysine to arginine mutation at residue 40 of α-tubulin to prevent acetylation.[179,199] This mutation did not affect the overall architecture or any of the MIPs. Therefore, we predominantly used the 3.7 Å K40R map for initial modeling of tubulin and MIPs.

2.7.2. *Tetrahymena* DMT consists of conserved and non-conserved MIPs

We (myself, Dr. Bui, Dr. Sky Yang, and Dr. Shintaroh Kubo) modeled and identified 41 MIPs (Fig. 2.2 and Table 2.3). Of those, 28 MIPs are found in DMTs in other species, including *Chlamydomonas reinhardtii* and mammals, while 13 are *Tetrahymena*-specific (Table 2.3 and Table 2.4). These conserved MIPs include proteins at the inner junction (CFAP20, CFAP45, CFAP52),[139,140] PACRG,[18,200,201] the outer junction (CFAP77), and the ribbon PF arc (RIB43a and RIB72A/B).[202,203] Conserved and species-specific MIPs decorate every region of the DMT. The region with the most divergence is the ribbon PF arc (Fig. 1.4B).

I observed several species-specific MIPs. In bovine (mammalian generally) respiratory cilia, the ribbon PF arc is occupied by a tektin bundle in addition to RIB43a (RIBC2) and RIB72A/B (EFHC1/2).[19] Interestingly, novel *Tetrahymena* MIPs were present throughout the DMT and ranged from globular (TtRIB22, TtRIB35) to filamentous (fMIPs along PFs B3-B6).

These findings led me to hypothesize that MIPs belong to one of two groups: evolutionarily conserved MIPs and species-specific MIPs. Conserved MIPs have

universal functions in cilia, whereas species-specific MIPs have evolved in response to specific stability requirements as a result of a unique ciliary movement in a specific organism or organ system.

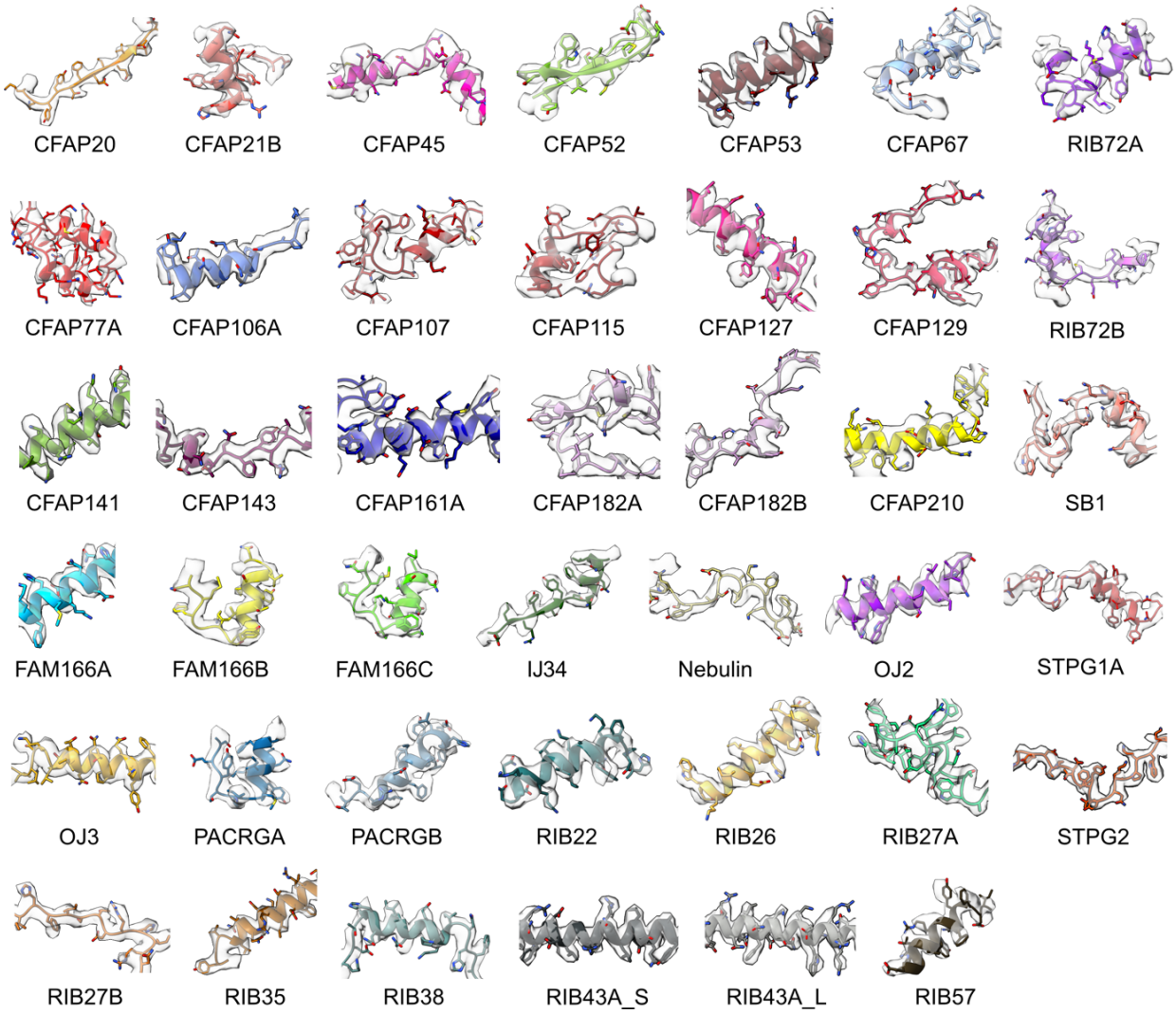

Figure 2.2. Visualization of side-chain densities of MIPs and crosslinks with tubulin. Examples of cryo-EM maps and the respective atomic models of all *Tetrahymena* MIPs modeled in this study. Adapted from Kubo *et al.*, 2023.[142]

Table 2.3. Identification of *Tetrahymena* proteins based on side chain fitting of our cryo-EM map. The E-value is reported from the FindMySequence search of the C-alpha backbone against the K40R cryo-EM map with proteins in the ciliome. Adapted from Kubo *et al.*, 2023.[142]

MIP	UniProt ID	E-value	2nd match	E-value (2nd)	3rd match	E-value (3rd)
CFAP20	Q22NU3	2.60E-52	Q22SL3	6.70E-03		
CFAP21B	I7MLS4	6.30E-80	I7MK20 (CFAP21A)	7.90E-05		
CFAP45	W7XCX2	7.10E-10				
CFAP52A	Q22ZH2	8.40E-164	I7MJ23 (CFAP52B)	7.10E-21	Q24C92 (CFAP52C)	4.00E-13
CFAP53	Q23YQ8	3.00E-60	A4VD76	1.20E-01		
CFAP67	W7XGD1	5.20E-126	I7M7Q3	2.10E-85	Q23U54	6.00E-09
CFAP77A	Q22WR6	4.90E-31	Q239Q2 (CFAP77B)	6.30E-21		
CFAP106A	I7M279	5.20E-53	I7LU20 (CFAP106B)	4.60E-23	Q238Q9 (CFAP106C)	7.30E-21
CFAP107	Q237T1	7.50E-20				
CFAP112A (B3B4_fMIP)	Q23A15	1.70E-06				
CFAP112B (B5B6_fMIP)	I7MEK6	8.20E-06				
CFAP115	Q23KF9	9.20E-105	W7XC24	1.40E-04		
CFAP127	I7LV70	1.40E-37				
CFAP129	I7M9I4	1.40E-18				
CFAP141	A4VCU8	2.70E-27				
CFAP143	A4VD56	1.70E-39				
CFAP161A	Q22WJ6	3.40E-95	I7M8Z8 (CFAP161B)	5.10E-41	I7ME23 (RIB57)	1.60E-06
CFAP182A	Q24BV4	1.80E-17				
CFAP182B	I7MLW3	6.90E-20				
CFAP210	Q23EX8	2.10E-22	W7XDG5	2.10E-03	Q22GH8	2.20E-02
FAM166A	Q238X3	6.80E-21	Q235M9 (FAM166B)	4.70E-05		
FAM166B	Q235M9	1.90E-20	Q238X3 (FAM166A)	1.20E-06		
FAM166C	Q22B75	1.10E-43	Q238X3 (FAM166A)	1.70E-01		
IJ34	I7M9T0	1.50E-95				
Nebulin	Q231B6	4.50E-06				
OJ2	Q236L2	1.90E-37	I7MAL9	5.70E-14	Q24DL2	5.50E-11
PACRGA	I7MLV6	5.10E-72	I7M312 (PACRGC)	3.10E-49		
PACRGB	I7M317	3.80E-57	I7MLV6 (PACRGA)	2.10E-39		
RIB22	I7LT67	3.80E-54	I7ME23 (RIB57)	1.20E-10	I7M8Z8 (CFAP161B)	5.00E-10
RIB26	Q232I6	2.20E-83				

RIB27A	I7LUL4	7.40E-23	Q22CT6 (RIB27B)	5.10E-11	Q22B75 (FAM166C)	1.10E-01
RIB27B	Q22CT6	1.30E-04	I7LUL4 (RIB27)	1.40E-02		
RIB35	I7ME81	1.20E-73	I7LT67 (RIB22)	1.60E-09	I7M8Z8 (CFAP161B)	9.60E-09
RIB38/Tex36B	Q23JL9	1.00E-76	Q233Y0	4.80E-25		
RIB43A_S	A4VDZ5	9.50E-41	Q240R7 (RIB43A_L)	8.50E-08		
RIB43A_L	Q240R7	3.30E-64	A4VDZ5 (RIB43A_S)	3.60E-04	W7XC77 (PG-rich)	4.00E-04
RIB57	I7ME23	1.30E-127	I7LT67 (RIB22)	5.50E-08	I7M8Z8 (CFAP161B)	9.80E-07
RIB72A	I7M0S7	1.10E-204	I7MCU1 (RIB72B)	2.30E-50		
RIB72B	I7MCU1	3.00E-164	I7M0S7 (RIB72A)	6.00E-53		
SB1 (SeamBinding1)	Q231B2	3.90E-31				
STPG1A	Q24GM1	2.80E-28	I7MF67 (STPG1B)	7.60E-17		
STPG2	I7M2G0	6.70E-16				

Interestingly, many of the conserved MIPs present as a single ortholog in other species were determined to have several paralogs in *Tetrahymena* (Table 2.3). MIP paralogs alternate along the length of the MT with different periodicities and patterns depending on the paralog (Fig. 2.3A-I). It is important to note that a weakness with these findings was that I was limited by the resolution of the map and the sensitivity of the mass spectrometry data. It is possible that some paralogs may have different periodicities than we found. Some of the MIPs had very clear periodicities and locations in the DMT, namely, TtCFAP182, TtFAM166, TtPACRG, TtRIB27, and TtRIB72 (Fig. 2.3 and Fig. 2.4A-I). Some of the MIPs had paralogs with sequences that were too similar to distinguish from their cryo-EM density, such as TtCFAP77 and TtCFAP106. In those cases, we deferred to the mass spectrometry data and modeled only the paralog that had the greatest abundance (Table 2.3). In a few instances, MIPs had paralogs detected in the mass

spectrometry data, but the stoichiometry overwhelmingly favored a single paralog; this was the case for TtCFAP52A and not TtCFAP52B or TtCFAP52C (Table 2.3). Those paralogs with lesser stoichiometry are likely more abundant in DMTs near the ciliary base or tip.

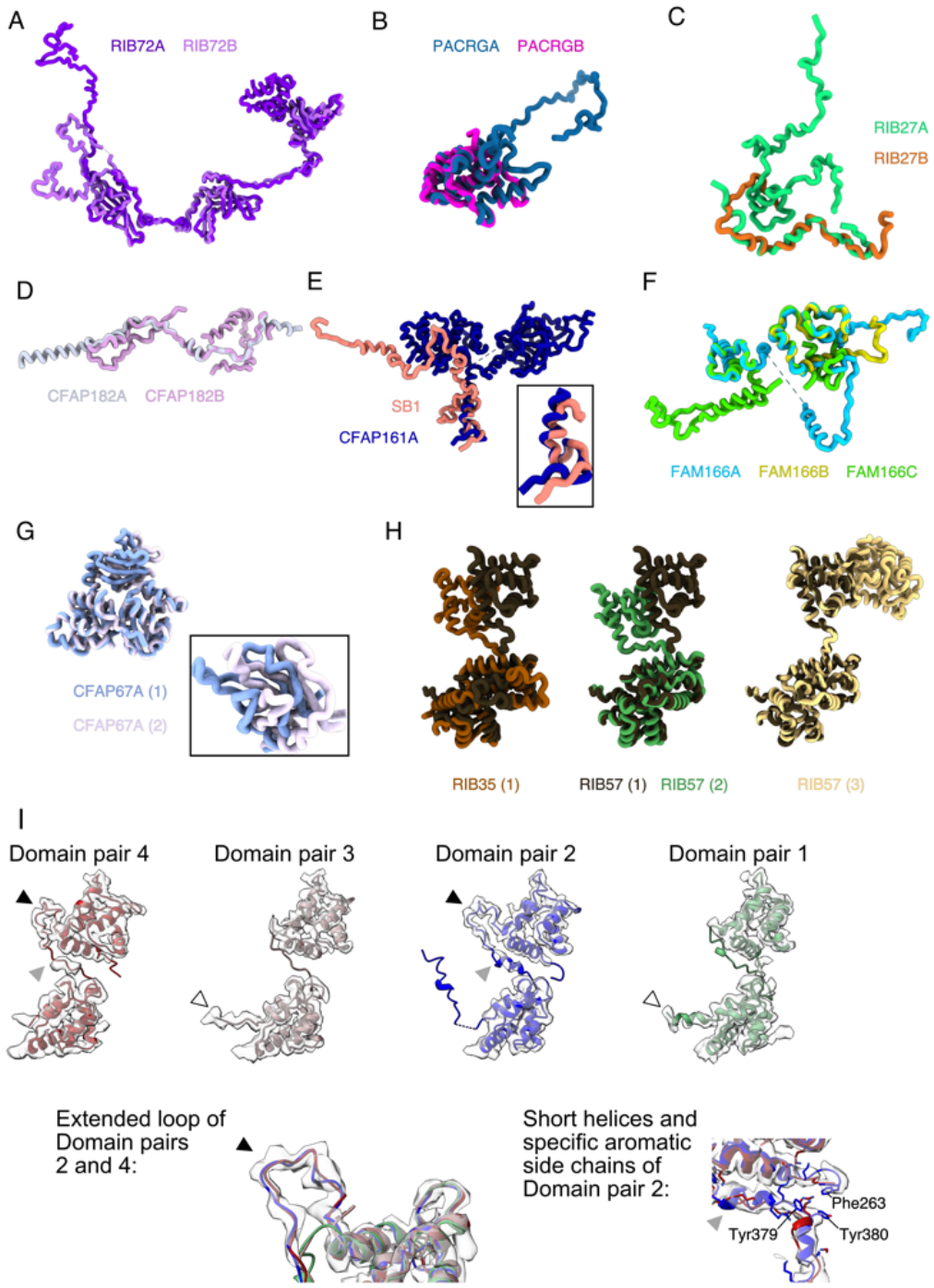

Figure 2.3. Paralogs and unique conformations of *Tetrahymena* MIPs. (A-H) Structural comparisons of paralogs and unique conformations of *Tetrahymena* MIPs. (A) RIB72A and RIB72B. **(B)** PACRGA and PACRGB. **(C)** RIB27A and RIB27B. **(D)** CFAP182A and CFAP182B. **(E)** SB1 and CFAP161A. **(F)** FAM166A, FAM166B, and FAM166C. **(G)** CFAP67 repeats 1 and 2. **(H)** The EF-hand of repeat 1 of RIB57 is aligned with repeats 2 and 3, as well as with RIB35. **(I)** CFAP115 EF-hand domain pairs 1 and 3 are similar to each other, as are EF-hand domain pairs 2 and 4. However, a short central helix and nearby aromatic side chains are unique to EF-hand domain pair 2. Adapted from Kubo *et al*., 2023.[142]

The ribbon PF arc region of the DMT is interesting evolutionarily because it is the least conserved region (Fig. 1.4B). This raises an interesting question of how species-specific ciliary/flagellar beating action and MIP conservation are related. One of the most conserved and well-studied ribbon PF arc proteins is RIB43a (RIBC2 in mammals), which has 2 paralogs in *Tetrahymena*: RIB43aS and RIB43aL (Fig. 2.3A-I and Table 2.3). RIBC2/RIB43a is important for the stability of the ribbon PF arc[17,202] and is required for motility in *Xenopus laevis* multiciliated epithelial cells.[204] Hypermethylation of RIBC2 is associated with ulcerative colitis,[205] and differential expression of RIBC2 is associated with many different cancers, including breast cancer and kidney renal clear cell carcinoma.[205,206] In metazoans, the ribbon PF arc region is occupied by a tektin bundle[19] that is not present in *Tetrahymena* or *Chlamydomonas* (Fig. 1.4B, Fig. 2.4C and Fig. 2.5A,B).[16,142]

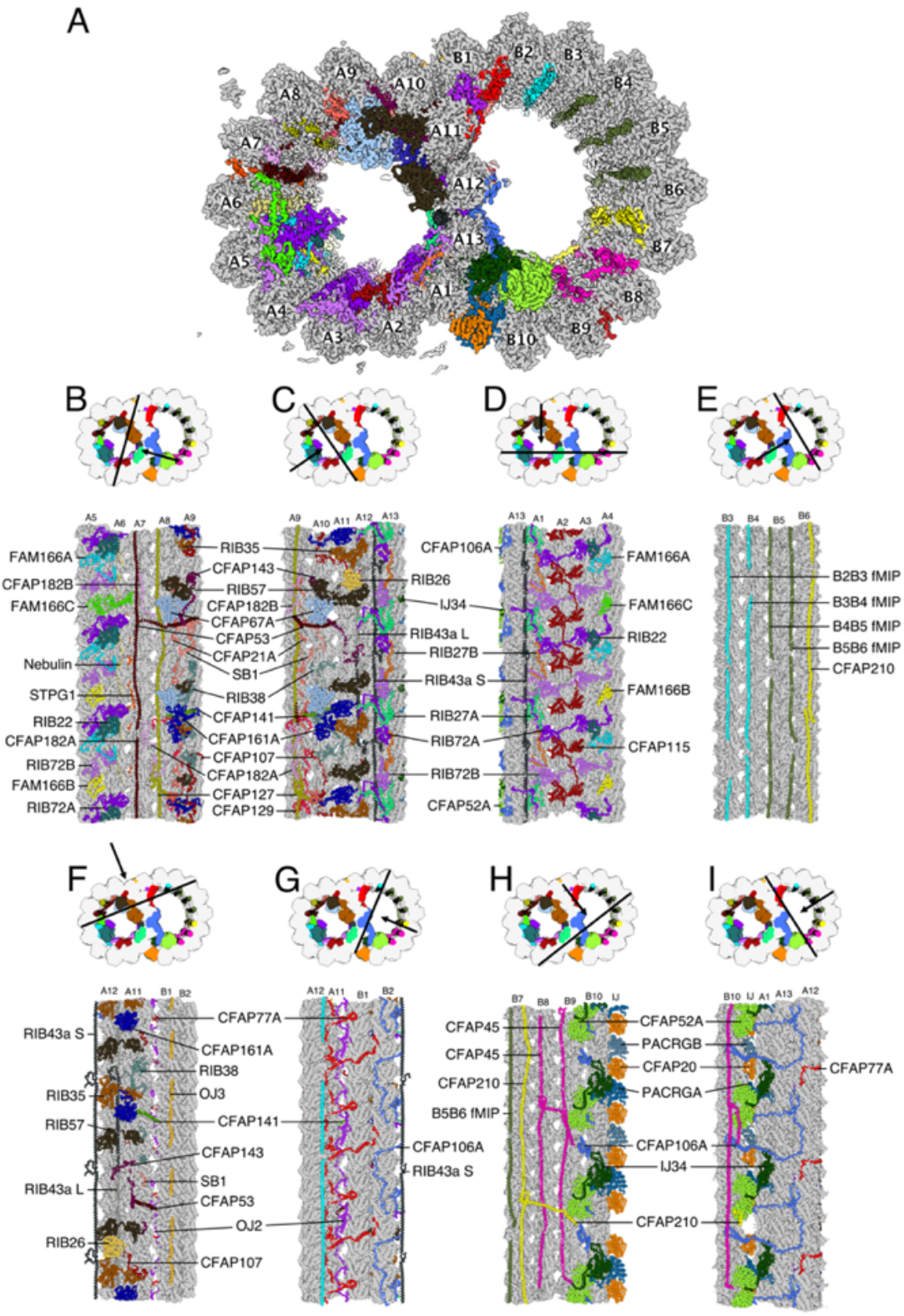
A
A9
A10
B1
B2
B3
B4
A8
A11
B5
A7
A12
B6
A6
A13
B7
A5
A1
B8
A4
A2
B9
A3
B10
B
C
D
E
A5 A6 A7 A8 A9
A9 A10 A11 A12 A13
A13 A1 A2 A3 A4
B3 B4 B5 B6
FAM166A
CFAP182B
FAM166C
Nebulin
STPG1
RIB22
CFAP182A
RIB72B
FAM166B
RIB72A
RIB35
CFAP143
RIB57
CFAP182B
CFAP67A
CFAP53
CFAP21A
SB1
RIB38
CFAP141
CFAP161A
CFAP107
CFAP182A
CFAP127
CFAP129
RIB26
IJ34
RIB43a L
RIB27B
RIB43a S
RIB27A
RIB72A
RIB72B
CFAP52A
CFAP106A
FAM166A
FAM166C
RIB22
FAM166B
CFAP115
B2B3 fMIP
B3B4 fMIP
B4B5 fMIP
B5B6 fMIP
CFAP210
F
G
H
I
A12 A11 B1 B2
A12 A11 B1 B2
B7 B8 B9 B10 IJ
B10 IJ A1 A13 A12
RIB43a S
RIB35
RIB57
RIB43a L
RIB26
CFAP77A
CFAP161A
RIB38
OJ3
CFAP141
CFAP143
SB1
CFAP53
OJ2
CFAP107
CFAP106A
RIB43a S
CFAP45
CFAP45
CFAP210
B5B6 fMIP
CFAP52A
PACRGB
CFAP20
PACRGA
CFAP106A
IJ34
CFAP210
CFAP77A

Figure 2.4. The structure of the native DMT from *Tetrahymena*. A A cross-section of the DMT map. Each color denotes an individual MIP. Tubulins are in gray. **B–I** Views of the lumen of the DMT from different angles as indicated by the black arrow. The cutting plane is indicated by black lines. Adapted from Kubo *et al*., 2023.[142]

The core ribbon PF arc proteins are CFAP21, CFAP53, CFAP67 (NME7), CFAP107, CFAP127 (MNS1), CFAP141, CFAP143 (SPAG8), RIB43a (RIBC2), and RIB72 (EFHC1) (Fig. 2.5B and Table 2.3). Species-specific differences include bovine tektin; *Chlamydomonas* FAP166, FAP222, FAP273, FAP363, and RIB21; and *Tetrahymena* TtCFAP182, TtRIB26, TtRIB27, TtRIB35, TtRIB38, TtRIB57, and TtSB1 (Fig. 2.5A, B and Table 2.4). Interestingly, TtRIB57 is present every 16 nm of the axonemal DMT and adopts three different conformations within 48 nm (Fig. 2.3H and Fig. 2.5B). The structural flexibility of TtRIB57 explains how the AlphaFold2 predicted model of TtRIB57 conflicts with the intra-molecular crosslinks observed for TtRIB57 based on *in situ* crosslinking mass spectrometry.[207]

Table 2.4. Species-specific MIPs in *Tetrahymena*, *Chlamydomonas* and *Bovine cilia*. Adapted from Kubo *et al.*, 2023.[142]

Tetrahymena	Reference (cilia)	Chlamydomonas	Reference (cilia)	Bovine	Reference (cilia)
TtB3B4_fMIP	This study	FAP68	[208]	EFCAB6	[19,209]
TtB4B5_fMIP	This study	FAP85	[210]	TEKTIN 1	[19,211,212]
TtB5B6_fMIP	This study	FAP90	[208]	TEKTIN 2	[19,211,212]
TtIJ34	This study	FAP166	[208]	TEKTIN 3	[19,211,212]
TtOJ2	This study	FAP222	[208]	TEKTIN 4	[19,211,212]
TtOJ3	This study	FAP252	[208,213]	TEKTIP1	[19]
TtRIB22	This study	FAP273	[214]		
TtRIB26	This study	FAP363	[16]		
TtRIB27A	This study	RIB21	[16]		
TtRIB27B	This study	RIB30	[16]		
TtRIB35	This study				
TtRIB38	This study				
TtRIB57	This study				
SB1	This study				
STPG1A	This study				
STPG1B	This study				
STPG2	This study				
Nebulin	This study				

The non-conserved proteins of the ribbon PF arc undoubtedly function to stabilize the DMT. It would be interesting to compare the relative stability of the ribbon PF arc between species. Perhaps these proteins have evolved because of species-specific ciliary/flagellar waveforms and motility. The non-conserved proteins may also function to provide ciliated organisms with unique regulatory mechanisms.

The strength of the DMT is dependent upon the stability of the inner and outer junctions (Fig. 1.4). The *Tetrahymena* inner junction MIPs include the inner junction PF proteins CFAP20 and PACRG (paralogs A and B), CFAP52, CFAP106, and IJ34 (Fig. 2.5A). The PF protein PACRG has two paralogs in *Tetrahymena*; PACRGA has an extended N-terminal region that projects toward the lumen and contains an α-helix that is proximal to

CFAP52 (Fig. 2.5A). Interestingly, DMTs purified from *Tetrahymena* are uniquely sensitive to salt treatment[8]; the inner junction becomes unstable, and single particle analysis of salt-treated *Tetrahymena* DMTs results in cryo-EM maps that lack density for the inner junction PF.[8,17,18] Perhaps the PACRGB paralog, which lacks the lumen-interacting N-terminal domain of PACRGA and PACRG homologs in *Chlamydomonas* and bovine cilia, contributes to species-specific salt sensitivity.[142]

IJ34 (CCDC81) is the only *Tetrahymena*-specific inner junction MIP (Fig. 2.5A). IJ34 is positioned around PF A1 and CFAP52 and acts as a stabilizing tether for CFAP52. Interestingly, CFAP52 is stabilized by a species-specific MIP for *Chlamydomonas* (FAP276)[16,18] and bovine respiratory cilia (EFCAB6).[19] These three CFAP52 tethers are examples of a functional homolog.

In 2021, the Agard and Winey laboratories published a 12 Å cryo-EM map of the *Tetrahymena* DMT using cryo-ET and subtomogram averaging.[151] They observed several filamentous and globular densities of unidentified MIPs.[151] One of those unidentified MIPs is localized to the inner junction, has a density that looks like the letter “X,” and spans PFs from both the A- and B-tubules.[151] I was not able to observe densities for any of those unidentified MIPs; this may be explained by low abundance or sample preparation.

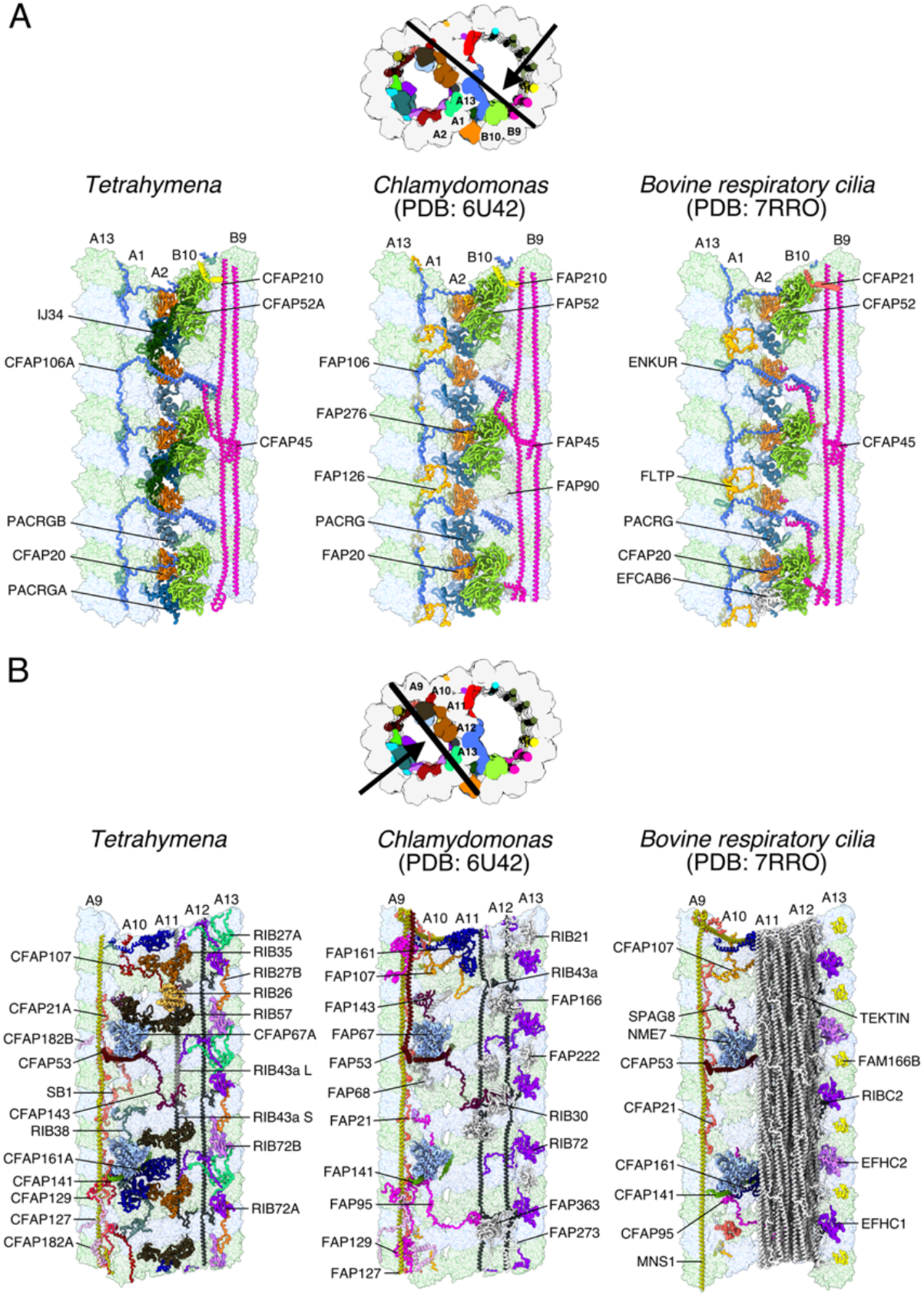
A
A13
A1
A2
B10
B9
Tetrahymena
Chlamydomonas
(PDB: 6U42)
Bovine respiratory cilia
(PDB: 7RRO)
CFAP210
CFAP52A
IJ34
CFAP106A
CFAP45
PACRGB
CFAP20
PACRGA
FAP210
FAP52
FAP106
FAP276
FAP45
FAP126
FAP90
PACRG
FAP20
CFAP21
CFAP52
ENKUR
CFAP45
FLTP
PACRG
CFAP20
EFCAB6
B
A9
A10
A11
A12
A13
Tetrahymena
Chlamydomonas
(PDB: 6U42)
Bovine respiratory cilia
(PDB: 7RRO)
RIB27A
RIB35
CFAP107
RIB27B
RIB26
CFAP21A
RIB57
CFAP182B
CFAP67A
CFAP53
RIB43a L
SB1
CFAP143
RIB43a S
RIB38
RIB72B
CFAP161A
CFAP141
CFAP129
RIB72A
CFAP127
CFAP182A
RIB21
FAP161
RIB43a
FAP107
FAP166
FAP143
FAP67
FAP222
FAP53
FAP68
RIB30
FAP21
RIB72
FAP141
FAP95
FAP363
FAP273
FAP129
FAP127
CFAP107
TEKTIN
SPAG8
NME7
FAM166B
CFAP53
RIBC2
CFAP21
CFAP161
EFHC2
CFAP141
EFHC1
CFAP95
MNS1

Figure 2.5. Comparison of the DMT structure from *Tetrahymena*, Chlamydomonas and bovine respiratory cilia. A The inner junction; note that the architecture is well conserved. **B** The PF ribbon region; note many species-specific MIPs. Adapted from Kubo *et al.*, 2023.[142]

2.7.3 MIP distribution in Tetrahymena has 96-nm periodicity

In *Chlamydomonas* and bovine models of DMTs, MIPs have a 48-nm periodicity,[16,19] while in *Tetrahymena,* MIPs have a 96-nm periodicity.[142] Tubulin heterodimers and CFAP20 have a periodicity of 8 nm.[200] MIPs TtRIB22 and RIB72A/B are present every 16 nm (Fig. 2.4B and Fig. 2.5B). Many MIPs have periodicities of 48 nm, including CFAP45, CFAP53, and CFAP143 (Fig. 2.4F, H). In *Chlamydomonas*, CrFAP115 is a 26.6 kDa MIP with an EF-hand pair domain that sits between PFs A1 and A3 and has a periodicity of 8 nm.[16] In *Tetrahymena*, TtCFAP115 is a 110.5 kDa MIP (Fig. 2.3I and Fig. 2.6A, B). TtCFAP115 has 4 EF-hand domain pairs and a periodicity of 32 nm (Fig. 2.3I). There are MIPs in *Tetrahymena* with periodicities of 8, 16, 32, and 48 nm. The least common multiple of those numbers is 96. Thus, the periodicity of *Tetrahymena* MIPs is 96 nm.

Modeling CFAP115 in the 48-nm DMT was difficult. The ColabFold predicted structure of CFAP115 included 4 very similar EF-hand pair domains. Since *Chlamydomonas* FAP115 is approximately 26 kDa, has 1 EF-hand domain pair, and has a periodicity of 8 nm, I assumed that *Tetrahymena* CFAP115 has a periodicity of 32 nm because it is approximately 4 times the mass and has 4 times the domain pairs. When I looked at the 3.7 Å cryo-EM map in the A1-A3 region, I found densities for EF-hand pair domains and partial densities for unstructured connecting regions (Fig. 2.3I and Fig. 2.4D). Since the CFAP115 model has 4 very similar EF-hand domain pairs, the correct placement of each domain with respect to every other protein in the 48-nm DMT required scrutiny. To be as

confident as possible, I closely examined the structural features of each of the domains and the corresponding densities. First, the second and fourth domain pairs have a short α-helix positioned between each EF-hand domain (Fig. 2.3I). In addition, every second density for a CFAP115 EF-hand domain pair has a corresponding density for that short α-helix (Fig. 2.3I). Furthermore, the second and fourth domain pairs have an extended loop that connects the EF-hand domains. Again, every second density for a CFAP115 EF-hand domain pair has a corresponding density for that extended loop (Fig. 2.3I). With this information, I only had a 50% chance of correctly placing CFAP115 in the 48-nm DMT (Fig. 2.4D). I then fit both the second and fourth EF-hand domain pairs in the same density and looked at side chain fitting. While both models fit reasonably well, it was clear that the second domain pair was a better fit. One side chain that helped differentiate the correct placement was Tyr380 of the second domain pair (Fig. 2.3I).

2.7.4 RIB72A and RIB72B are differentially required for the stability of several A-tubule MIPs

Once I was confident about the model, I was curious about the role of TtCFAP115 and interactions with other MIPs (Fig. 2.4D). Our model shows that a single CFAP115 molecule likely interacts with 2 molecules each of RIB72A and RIB72B (Fig. 2.4D). To validate the interaction based on proximity in our model, I used a genetics approach. Beyond its interaction with CFAP115, RIB72 (EFHC) is a well-conserved MIP required for motility in *Tetrahymena*[144] and associated with human disease.[205,206] We acquired RIB72 knockout strains from Dr. Jacek Gaertig's laboratory and performed mass spectrometry analysis of *Tetrahymena* strains *CU428*, *RIB72B-KO*, and *RIB72A/B-KO* (Fig. 2.4D, Fig. 2.6A-C and Table 2.5). Proteins with the highest abundance in both *CU428* (WT) and

RIB72B-KO belonged to MIPs RIB72A, CFAP115, FAM166B, FAM166C, RIB22, RIB27A, and RIB27B (Fig. 2.3, Fig. 2.4, and Table 2.5). In support of a RIB72 interaction, CFAP115 was absent in the proteome of the RIB72 double knockout (Fig. 2.4D, Fig. 2.6C and Table 2.5). RIB72A, RIB72B, FAM166C, FAM166B, RIB22, RIB27A, and RIB27B were also all absent. The loss of CFAP115 in the *RIB72A/B-KO* proteome was supported by previous studies that showed the same.[16,143,144,151] Interestingly, only RIB27B was significantly reduced in the *RIB72B-KO* proteome, while CFAP115 and the other MIPs were all relatively abundant (Table 2.5). Although it was not the primary objective, these results also validated the models of CFAP115, FAM166B, FAM166C, RIB22, RIB27A, and RIB27B protein structures, which had been modeled and identified using only the wild-type strain (Table 2.5). While we were reasonably confident in the protein models, comparative proteomics supported the possible interactions we observed. To further investigate the roles of CFAP115 and RIB72, it would be worthwhile to perform mass spectrometry analysis on the RIB72A knockout strain.

When mass spectrometry analysis was performed on a *Tetrahymena* CFAP115-KO strain, both RIB72 paralogs were abundant.[143] Cryo-ET studies have shown that CFAP115 knockout resulted in defects in cryo-ET densities of the ribbon PF arc and the inner junction regions.[143,151] Those structural defects observed from cryo-ET could explain the ciliary action defects seen with *Tetrahymena CFAP115-KO* cells.[143] *CFAP115-KO* cilia have a slow power stroke and consequently swim slowly compared to wild-type cilia.[143]

Table 2.5. Mass spectrometry analysis of wild-type (WT), RIB72B and RIB72A/B knockout mutants showing the missing proteins. Only proteins with quantitative values > 1 are shown. Adapted from Kubo *et al.*, 2023.[142]

UniprotID	WT (CU428)			RIB72B-KO			RIB72A/B-KO		
	S1	S2	S3	S1	S2	S3	S1	S2	S3
I7MCU1 (RIB72B)	217.4	199.6	212.8	0.0	0.0	0.0	0.0	0.0	0.0
I7M0S7 (RIB72A)	172.9	189.0	181.7	246.0	245.9	242.0	0.0	0.0	0.0
Q23KF9 (FAP115)	300.3	313.5	297.0	294.5	281.9	281.9	0.0	0.0	0.0
Q238X3 (FAM166C)	101.3	102.4	115.2	84.5	89.0	102.7	0.0	0.0	0.0
Q235M9 (FAM166B)	35.8	34.4	44.3	33.8	39.2	38.8	0.0	0.0	0.0
I7LT67 (RIB22)	31.4	30.9	37.2	16.9	21.2	21.7	0.0	0.0	0.0
I7LUL4 (RIB27A)	28.8	20.3	31.9	13.7	27.6	30.8	0.0	0.0	0.0
Q22CT6 (RIB27B)	27.9	36.2	39.0	1.1	4.2	3.4	0.0	0.0	0.0
W7XC77 (PG-rich)	13.1	11.5	16.0	7.4	8.5	12.6	0.0	0.0	0.0
I7LV80	10.5	12.4	9.8	0.0	0.0	1.1	0.0	0.0	0.0
Q22TY0	9.6	8.8	8.9	0.0	0.0	0.0	0.0	0.0	0.0
I7LVP2	8.7	11.5	9.8	0.0	1.1	2.3	0.0	0.0	0.0
Q231F9	5.2	1.8	7.1	1.1	0.0	1.1	0.0	0.0	0.0
Q22CT4	5.2	4.4	3.5	0.0	0.0	1.1	0.0	0.0	0.0
I7M2F8	2.6	4.4	2.7	0.0	41.3	3.4	0.0	0.0	0.0
I7M6E1	2.6	3.5	1.8	0.0	0.0	0.0	0.0	0.0	0.0
Q22KN2	1.7	2.6	1.8	0.0	0.0	0.0	0.0	0.0	0.0
Q22HI8	1.7	0.9	0.9	0.0	0.0	0.0	0.0	0.0	0.0
I7MDS6	1.7	0.9	1.8	0.0	0.0	0.0	0.0	0.0	0.0
I7LWU5	1.7	0.9	1.8	1.1	1.1	0.0	0.0	0.0	0.0
Q22S92	1.7	0.0	0.9	0.0	0.0	0.0	0.0	0.0	0.0

My results show that the stability of CFAP115, FAM166C, FAM166B, RIB22, and RIB27A all depend upon the presence of RIB72A; interestingly, RIB27B is dependent upon both RIB72A and RIB72B (Fig. 2.5B and Table 2.5). Studies using *Tetrahymena CFAP115-KO* cells have shown that CFAP115 stabilizes the MT lattice and is important for motility. Together with other studies, this work suggests that the assembly of MIPs is highly regulated and ordered.[215,216]

2.7.5 Organization of the inner and outer microtubule proteins in *Tetrahymena* axonemal DMTs is uncoupled

Attached to the DMT outer surface are inner and outer dynein arms, the nexin-dynein regulatory complex and radial spoke proteins (Fig. 1.2 and Fig. 2.6D).[217] The outer surface of the DMT has 96-nm periodicity.[218] Studies have shown that CCDC39 (FAP59) and CCDC40 (FAP172) are MAPs that form a 96-nm long complex and act as molecular ruler for the length of the axonemal DMT (Fig. 2.6D and Fig. 2.6E).[136] The CCDC39/40 complex also defines the positions of various MAPs.[49] Through experimentation and a literature review, I have demonstrated that the periodicity of the *Tetrahymena* axonemal DMT is 96 nm for both MIPs and the rest of the axonemal proteins. For all other species studied, it appears that MIPs have a periodicity of 48 nm, while the outer proteins repeat at 96 nm.[16,19] One of the most interesting questions in the field right is now how the periodicity of MIPs is linked to the CCDC39/40 molecular ruler. Cryo-EM and mass spectrometry analyses have not yet provided that information. One possible explanation is that in the *Tetrahymena* axoneme, the organization of the proteins inside and on the surface of the MTs is uncoupled. In *Chlamydomonas* and mammals, it has been shown that different periodicities coexist between inner and outer proteins, while in *Tetrahymena,* they happen to be the same.[16,19,136] It is possible that merely the head-to-tail arrangement of axonemal proteins is sufficient to regulate their periodicity.

The structural and proteomic investigation of *Tetrahymena* CFAP115 and RIB72 paralogs informed us of the intricate assembly of MIPs and demonstrated the importance of complementary techniques. Sample preparation, single particle analysis, mass

spectrometry, genetic knockouts, and artificial intelligence were all integral to gaining insight into MIPs and protein interactions.

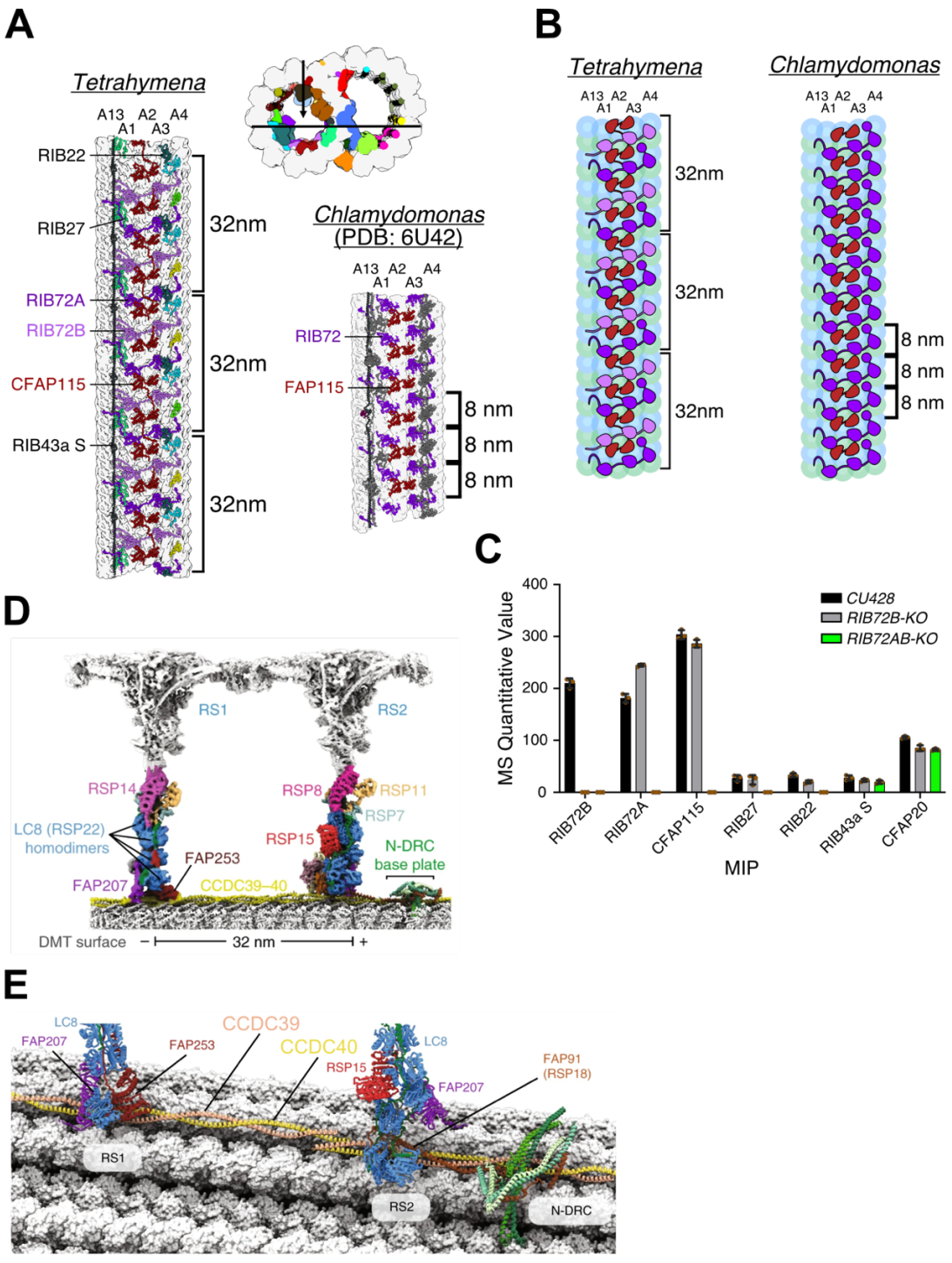

Figure 2.6. MIPs in *Tetrahymena* exhibit 96-nm periodicity. (A) TtCFAP115 shows 32-nm repeats leading to the true 96-nm periodicity of the MIPs of *Tetrahymena*. FAP115 in *Chlamydomonas* only repeats with 8-nm periodicity, leading to the normal 48-nm repeat. **(B)** Cartoon of *Tetrahymena* and *Chlamydomonas* PFs A13-A4 showing the arrangement of FAP115 and RIB72. **(C)** Quantitative value of mass spectrometry (normal total spectra value) of WT, RIB72B-KO, and RIB72A/B-KO cilia showing that TtCFAP115 is still intact after the knockout of RIB72B. n = 3 biological replicates for WT and each mutant. Data are presented as the mean values +/– standard deviation. Values for each replicate are shown in brown circles. Adapted from Kubo *et al*., 2023.[142] **(D)** Orthogonal views of an atomic model for the 96-nm repeat of the DMT. The model combines atomic models of the DMT-bound stalks of RS1 and RS2, and the stalk, neck and spoke head of isolated RS1 with the model of DMT (PDB 6U42). Adapted from Gui *et al*., 2021.[19] **(E)** Overview showing the bases of RS1 and RS2 bound to the DMT. The radial spoke subunits (LC8, FAP91, FAP207, FAP253 and RSP15), the CCDC39–40 molecular ruler, and the subunits of the N-DRC base plate are shown as cartoons. Tubulin is shown in surface representation. Adapted from Gui *et al*., 2021.[19]

2.7.6 The outer surface of the intact DMT is associated with many filamentous proteins

The architecture of ciliary complexes associated with the DMT surface has been mapped with the use of crosslinking mass spectrometry, cryo-EM, and cryo-ET followed by subtomogram averaging (Fig. 2.4).[16,219-222] The CCDC39/40 complex is a coiled-coil structure that weaves around the DMT surface, the nexin dynein regulatory complex (N-DRC), and radial spoke proteins (Fig. 2.6D and Fig. 2.6E). Radial spoke structures extend outward from the surface to the central pair apparatus (Fig. 2.6D). The inner and outer dynein arms both extend outward from the A-tubule toward the neighboring B-tubule (Fig. 1.2B, C). The N-DRC is a plate-like structure consisting of coiled-coil regions that link the inner and outer dynein arms with radial spokes (Fig. 2.6D, E).

In addition to the mechanoregulatory protein complexes associated with the DMT, we also observed several densities of ciliary MAPs in our cryo-EM map (Fig. 2.7A, B). Coupled with mass spectrometry data and AI-assisted protein structure predictions, our map has sufficient high-resolution information to identify some or all the MAPs bound to

the *Tetrahymena* DMT. I already *de novo* modeled the backbone of a MAP located at A10-B1 of the OJ, which we named OJ3 (Fig. 2.2, Fig. 2.4F, and Fig. 2.7B). Admittedly, the OJ of our cryo-EM map had the highest resolution, and the rest of the MAPs will require more effort. The relatively low resolution of the cryo-EM map for these regions is most likely a result of partial decoration or flexibility. The investigation of the identity and function of those ciliary MAPs has not been done and represents an impactful pursuit.

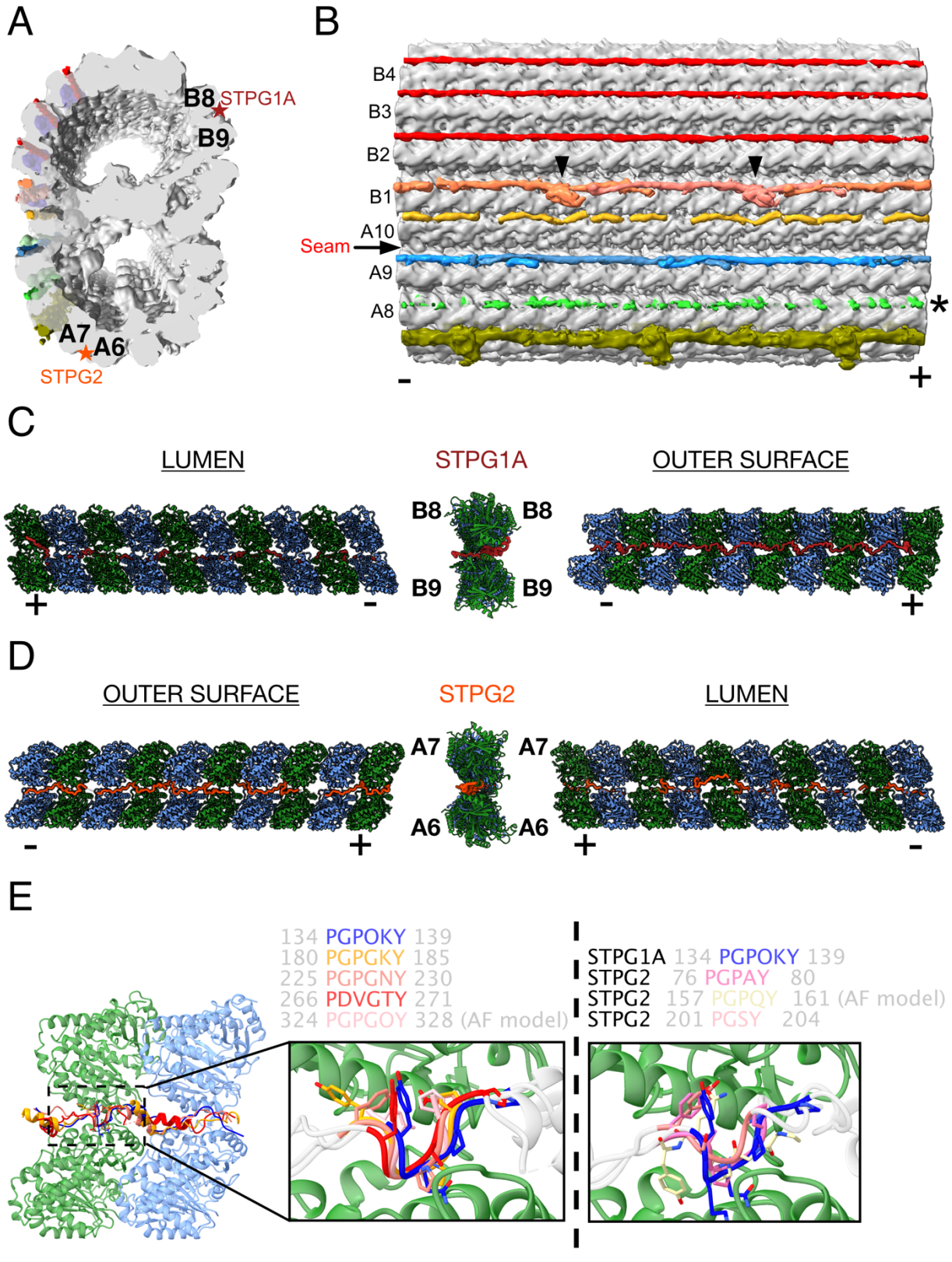
A
B8
STPG1A
B9
A7
A6
STPG2
B
B4
B3
B2
B1
Seam
A10
A9
A8
*
-
+
C
LUMEN
STPG1A
OUTER SURFACE
B8
B8
B9
B9
+
-
-
+
D
OUTER SURFACE
STPG2
LUMEN
A7
A7
A6
A6
-
+
+
-
E
134 PGPOKY 139
180 PGPGKY 185
225 PGPGNY 230
266 PDVGTY 271
324 PGPGOY 328 (AF model)
STPG1A 134 PGPOKY 139
STPG2 76 PGPAY 80
STPG2 157 PGPQY 161 (AF model)
STPG2 201 PGSY 204

Figure 2.7. The outer surface filaments on the native DMT. (A, B) Cross-sectional **(A)** and longitudinal **(B)** views of the outer surface filaments on the native *Tetrahymena* DMT. The filaments are bound to adjacent pairs of PFs from A8 to B5. The filaments between PFs B2-B3, B3-B4, and B4-B5 appear similar and have a 48-nm periodicity. In contrast, the filaments between PFs A9-A10, A10-B1 (OJ3), and B1-B2 appear to have a 24-nm periodicity. These filaments have a clear head-to-tail periodic arrangement between PFs A9-A10 and B1-B2. The filament between PFs B1B2 has a globular domain (black arrowheads). The density of the filament between PFs A8-A9 is very weak, probably due to partial decoration. (–) and (+) signs indicate the minus and plus ends of the MT, respectively. **(C)** STPG1A is a filamentous protein that is woven between PFs B7-B8, bound to the surface and the lumen. **(D)** STPG2 is a filamentous protein that is woven between PFs A6-A7, present on the outer surface and the lumen. **(E)** The PG-rich repeat motifs of STPG2 (left) and STPG1A (right) are structurally similar. Adapted from Kubo *et al*., 2023.[142]

The ciliary DMT MAPs appear as filamentous densities positioned near the wedge-shaped junction of neighboring PFs (Fig. 2.7A, B). *Tetrahymena* ciliary MAPs seem to bind very similarly to human MAP7.[223] MAP7 shares a binding site with kinesin-1, recruits and activates kinesin-1,[111,224] does not affect dynein,[111] and selectively inhibits kinesin-3 processivity.[111,225] MAP7 binds MTs as an extended α-helix that spans intra- and interdimer interfaces of tubulin PFs (~8 nm periodicity) and is positioned between the outermost ridge of the PF and the site of lateral interaction between adjacent tubulin (Fig. 2.8A, B).[223] I observed 8 *Tetrahymena* ciliary MAPs located between PFs A7-A10 of the A-tubule and B1-B5 of the B-tubule (Fig. 2.7A, B). The MAPs between A9-A10, A10-B1 (OJ3), and B1-B2 all appear to have 24-nm periodicities (Fig. 2.7A, B). The resolution of the rest of the MAPs is insufficient to interpret periodicity. Interestingly, A7-A10 of the A-tubule and B1-B5 of the B-tubule have been shown to be tracks for retrograde and anterograde transport, respectively (Fig. 2.8C-E).[75,226]

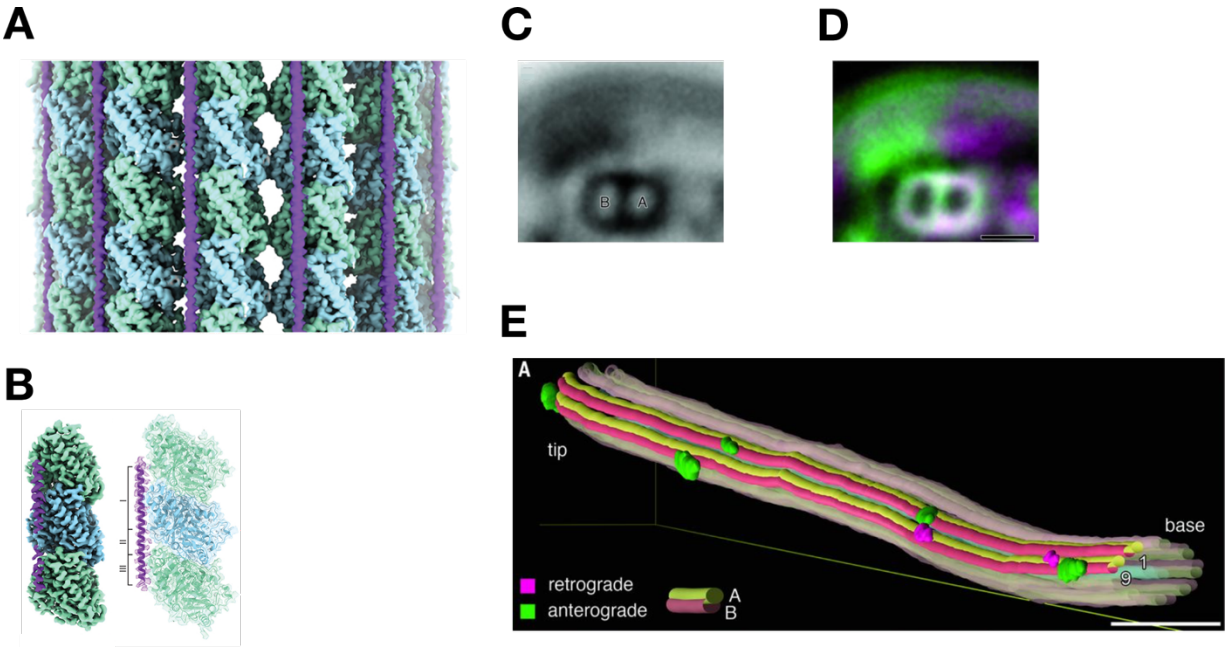

Figure 2.8. Anterograde and retrograde trains use different microtubules of the same DMT, which may be regulated by microtubule-associated proteins such as MAP7. (A) Cryo-EM map (without symmetry expansion) of an MT decorated with MAP7; α-tubulin, β-tubulin, and MAP7 are shown in green, blue, and purple, respectively. **(B)** Improved MAP7-MT cryo-EM map after symmetry expansion and PF-based density subtraction (see Methods). MAP7 binds across both inter- and intra-dimer interfaces, although weaker density is seen for the region over the intra-dimer interface (segment II), indicative of more flexibility and weaker interaction. Only one repeat of MAP7 and its neighboring tubulins is shown for clarity. Adapted from Ferro *et al.*, 2022.[223] **(C)** Average of 50 anterograde train positions on the DMT. The A- and B-tubules are indicated. **(D**) Position of anterograde (green) and retrograde (magenta) trains with respect to the DMT. **(E)** Segmentation of an axoneme, showing anterograde and retrograde trains moving simultaneously on DMT labeled "9". IFT trains are not shown on other DMTs for clarity. Adapted from Stepanek and Pigino, 2016.[75]

My hypothesis is that filamentous ciliary MAPs regulate IFT in *Tetrahymena*. I have found commonalities between the filamentous MAPs and MAP7 that lend support to that hypothesis. The motor proteins associated with IFT in *Tetrahymena* are kinesin-2 (anterograde) and dynein-2 (retrograde). Localization experiments in *Chlamydomonas* have shown that these motor proteins use the regions of the A- and B-tubules that are also occupied by MAPs (Fig. 2.8C-E).[75] Docking kinesin-2 to the B-tubule (anterograde)

and dynein-2 to the A-tubule (retrograde) revealed steric clashes with filamentous MAPs, possibly indicating competition for the same MT binding sites (Fig. 2.9A-D). MAP7 shares a binding site with kinesin-1 and recruits and activates it while inhibiting other motor proteins.[111,223] Filamentous MAPs may function in a similar manner. The low resolution of the cryo-EM densities for MAPs could be a result of partial decoration and flexibility related to conformational changes caused by binding of intraflagellar motor proteins. MAP7 has been shown to have concentration-dependent effects on kinesin-1.[111,223] At low concentrations, MAP7 recruits and improves kinesin-1 activity, while at high concentrations, MAP7 recruits and inhibits kinesin-1 processivity.[223] Perhaps MAPs only partially decorate DMTs in *Tetrahymena* cilia and have similar effects on intraflagellar motor proteins. The cryo-EM map of MAP7 bound to a MT was weakest where the MAP7 α-helix crossed the tubulin intradimer interface, which the authors attributed to motor protein-induced conformational rearrangements.[223] In addition to partial decoration, *Tetrahymena* ciliary MAPs may be highly flexible.

2.7.7 The PG-rich motif is a novel microtubule-binding domain

The *Tetrahymena* DMT surface contained two unique densities for non-filamentous MAPs positioned between PFs A6-A7 and B8-B9 (Fig. 2.7A-C). Both proteins are wedged between the adjacent PFs near the site of lateral interaction (Fig. 2.7A-D). The proximity to the DMT and the stability of these proteins meant that their cryo-EM densities had sufficient resolutions for *de novo* protein structure modeling and identification. STPG1A is positioned between B8-B9 of the B-tubule, and sperm tail proline- and glycine-rich repeat protein STPG2 is positioned between A6-A7 of the A-tubule (Fig. 2.7C, D).

STPG1A and STPG2 have 48-nm periodicities and have short α-helices and unstructured regions. Both proteins are part of the sperm tail proline- and glycine-rich repeat protein family (STPG), which contains multiple repeats of a proline (P)- and glycine (G)-rich motif (Fig. 2.7E and Fig. 2.9E).[227] STPG1A has 5 PG-rich motifs that are spaced out by linkers that are each approximately 40 amino acids (Fig. 2.9E). STPG2 has 3 PG-rich motifs interspersed with linkers ranging from 39 to 76 residues (Fig. 2.7E). The STPG1A PG-rich motif is P-G-P-G-x-Y, and the STPG2 PG-rich motif is P-G-P-x-Y, where "x" is one of many amino acids or none. A single STPG1A molecule spans 48 nm, with each ~40 amino acid linker spanning 8 nm. STPG1A PG-rich motifs occur every 8 nm at the lateral interaction between adjacent α-tubulin PFs (Fig. 2.7C-E). STPG2 also spans 48 nm, and its PG-rich motifs bind the same site, but the PG-rich motifs are spread over greater distances. When I superimposed all five STPG1A PG-rich motifs, it was clear that the PG-rich motif is in fact a MT-binding motif (Fig. 2.7E). The MT-bound STPG2 PG-rich motif is structurally similar to the MT-bound STPG1A PG-rich motif (Fig. 2.7E). Interestingly, STPG1A and STPG2 weave between the inner and outer DMT, binding to the DMT surface and lumen (Fig. 2.7C, D). STPG1A and STPG2 thread through the outer surface and lumen; these proteins are predominantly present at the outer surface wedge, do not appear to interact with other MIPs or MAPs and do not appear to link the inner and outer registries of MIPs and MAPs. In contrast, CFAP182A (Pierce1) and CFAP182B (Pierce2) are short partially helical proteins at the A-tubule that occupy the outer surface and lumen equally (Fig. 2.2 and Fig. 2.5B).

Along with STPG1A and STPG2, we detected 3 additional PG-rich motif proteins in the *Tetrahymena* cilia proteome for which we do not have cryo-EM densities: STPG1B (STPG1A paralog) and two Outer Dense Fiber 3-Like (ODF3L-1 and ODF3L-2) proteins (Fig. 2.9E). STPG1B is similar to STPG1A; the PG-rich motif pattern is P-G-P-G-x-Y, and the motifs are separated by ~40 amino acid linkers (Fig. 2.9E). The two ODF3L proteins have 12 P-G-P-G-x-Y motifs that would translate to occupying 12 α-tubulin lateral sites and span 96 nm along the DMT surface. *In situ* crosslink mass spectrometry analysis revealed crosslinks between the ODF3L proteins and residue 326 of α-tubulin, which is positioned in the PF wedge near the α-tubulin lateral interaction.[142]

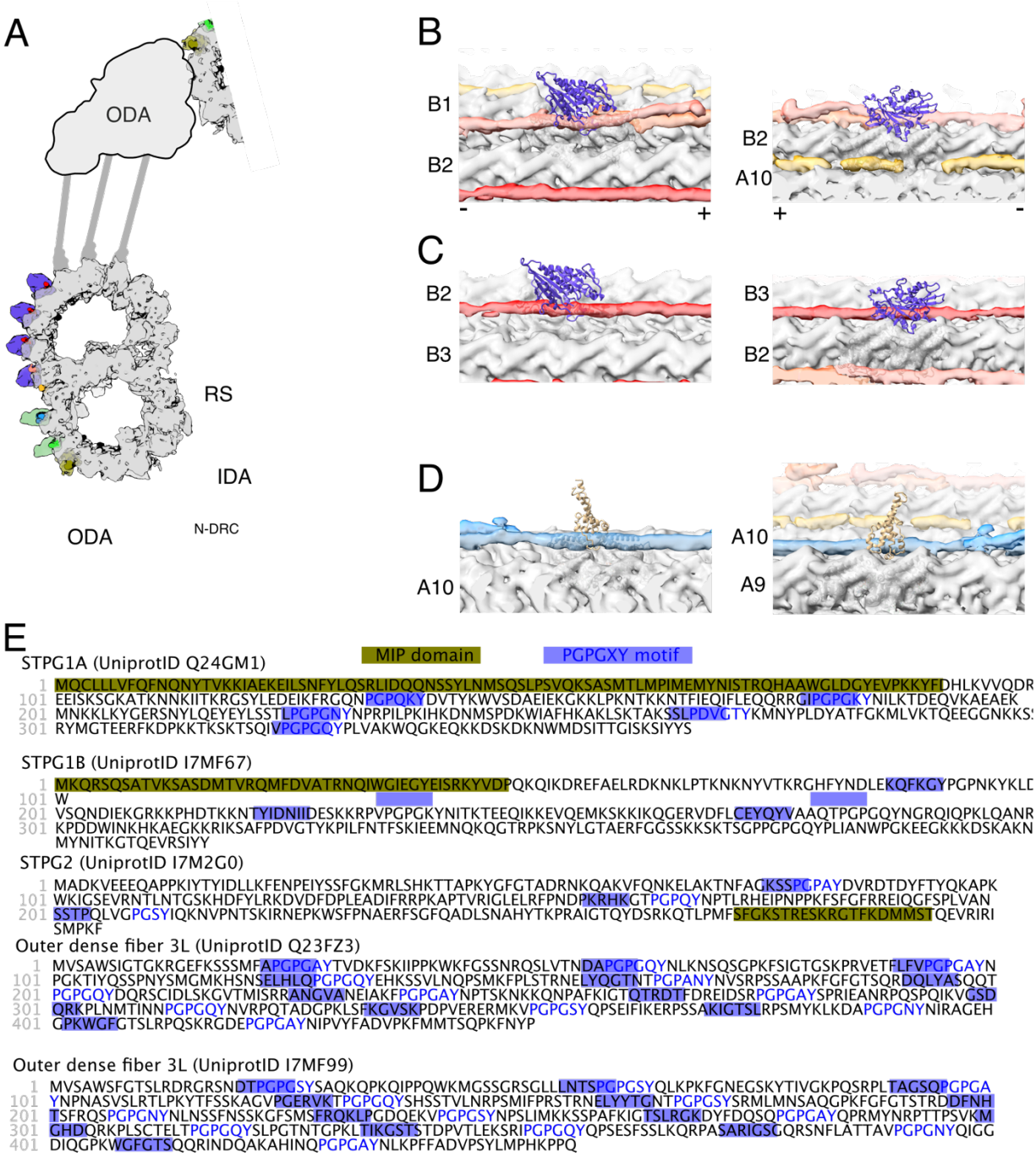

Figure 2.9. The outer surface filament presents steric clashes with dynein and kinesin. (A) A cartoon of the DMT showing the putative regions for IFT between A8- A10 and B1-B5. Violet densities: docking of kinesin MT-binding domain onto the B-tubule PFs, green densities: docking of dynein MT-binding domain onto the A8 and A9. ODA: Outer dynein arm; RS: Radial spoke; IDA: Inner dynein arm; N-DRC: Nexin-dynein regulatory complex. **(B-D)** Docking of kinesin (PDB 6OJQ) onto the outer surface filaments B1B2

(B) and B2B3 **(C)** showing a clear clash. **(D)** Docking of the dynein-2 MT-binding domain (PDB 6RZB) onto filament A9A10 showing the clear steric clash of the MT-binding domain. **(D)** Docking of the dynein-2 MT-binding domain (PDB 6RZB) onto filament A9A10 showing the clear steric clash of the MT-binding domain. (-) and (+) signs indicate the minus and plus ends of the MT, respectively. **(E)** Amino acid sequences for STPG1A, STPG1B, STPG2, and two outer dense fiber candidates. PG-rich repeat motifs (purple) and MIP domains (olive) are highlighted. (-) and (+) signs indicate the minus and plus ends of the MT, respectively. Adapted from Kubo *et al*., 2023.[142]

In my introduction, I set out to accomplish the following three research goals:

I Obtain a high resolution cryo-EM map of the doublet microtubule from axonemes of *Tetrahymena* cilia.

II Model the molecular architecture of the *Tetrahymena* DMT, compare the *Tetrahymena* DMT with DMTs from other species, and identify proteins at the outer junction region of the DMT.

III Study one or two outer junction MIPs to understand their function in cilia.

In this chapter, I used cryo-EM and complementary techniques to obtain a 4.1 Å resolution cryo-EM map of the DMT from axonemes of *Tetrahymena* cilia. Together with some members of the Bui lab, we then identified almost all the proteins stably associated with the 48-nm repeating unit of the Tetrahymena axonemal DMT. In the next chapter, I will investigate the outer junction region of the DMT to identify proteins and possible protein-protein interactions that are important for either assembly or stability of the DMT.

Chapter 3: Structural and functional characterization of the CFAP77 knockout mutant

The axonemal DMTs in *Tetrahymena* have at least 41 MIPs that form a network of luminal interactions and act as a stabilizing sheath (Fig. 2.4). One of the most interesting questions in the cilia field right is now how DMTs are formed. Current evidence points to proteins located at the outer junction region (OJ) being responsible for the assembly and stability of the B-tubule.[21,73,74,152,228] Specifically, one or more proteins suppress the C-terminal tails of β- and α-tubulins of the A-tubule, which allows stable recruitment of B-tubule tubulins.

In this chapter, I investigate ciliary proteins proximal to the OJ of the DMT, which is thought to be the site of DMT formation.[21,73,74,152,228] In Chapter 2, I reconstructed the DMT cryo-EM map. Then, I identified and modeled OJ MIPs CFAP77 and OJ2 and modeled the backbone of the OJ MAP OJ3 (Fig. 2.2, Fig. 2.4F and Fig. 2.7B). In this chapter, I performed structural and bioinformatics analyses to understand the mechanism and conservation of the OJ proteins. Based on that information, I collaborated with postdoctoral fellow Dr. Shintaroh Kubo to perform molecular dynamics simulations on the OJ MIPs CFAP77 and OJ2. I also collaborated with Dr. Ewa Joachimiak and Dr. Dorota Wloga to generate *Tetrahymena* CFAP77 knockout strains and perform subsequent cryo-ET and subtomogram averaging.

Here, I examined possible luminal interactions of the OJ MIPs CFAP77 and OJ2 (Fig. 3.1). I showed that the conserved OJ protein CFAP77 contributes to the stability of the B-tubule more than OJ2 based on molecular dynamics simulations. I also showed that loss of CFAP77 results in reduced swimming in *Tetrahymena*, as well as infrequent damage

to the OJ of axonemal DMTs. These results and discussion have been published in the journal Nature Communications.[142]

3.1 Methods – Sample preparation of *Tetrahymena* axonemes for cryo-ET

3.1.1 Growth of *Tetrahymena* strains *CU428* and *CFAP77A/B-KO*

There were two *Tetrahymena* strains used for cryo-ET analysis: *CU428* (*Tetrahymena* Stock Center #SD00178) and *CFAP77A/B-KO* (Wloga lab, Nencki Institute of Experimental Biology). Please refer to Section 2.1.1 in Chapter 2 for all details concerning storage in bean media, inoculation of SPP media, growth, and harvesting. All details included in Section 2.1.1 in Chapter 2 were followed exactly. I harvested 4 L of culture for both *CU428* and *CFAP77A/B-KO Tetrahymena* strains. This provided greater sample quantity for cryo-EM sample preparation and individual biological replicates for mass spectrometry analyses.

3.1.2 Cilia purification from *Tetrahymena* strains *CU428 and CFAP77A/B-KO*

Please refer to Section 2.1.2 in Chapter 2 for all details concerning harvesting of *Tetrahymena* cultures, dibucaine treatment, cilia isolation, and resuspension of intact, membranated cilia. I prepared suspensions of intact, membranated cilia exactly as per Section 2.1.2 in Chapter 2. From 2 pellets of cell culture (2 L), I had 500 μL of resuspended cilia in Cilia Wash Buffer. The intact membranated cilia were ready for the next step.

3.1.3 Intact axoneme preparation from purified *Tetrahymena strains CU428 and CFAP77A/B-KO* cilia

The membrane-bound cilia were centrifuged for 10 minutes at 7800 x g and 4°C using an Eppendorf Centrifuge 5415 D, and the Cilia Wash Buffer supernatant was removed. I

resuspended the pellet in 250 μL Cilia Final Buffer (Table 2.1) and added 44.1 μL 10% NP-40 alternative (final concentration 1.5%) then incubated the sample for 30 minutes on ice to de-membranate the cilia. I then centrifuged the sample for 10 minutes at 7800 x g and 4°C using an Eppendorf Centrifuge 5415 D, resuspended in fresh 250 μL Cilia Final Buffer, added 44.1 μL 10% NP-40 alternative, and incubated once more on ice for 30 minutes. The intact axoneme was resuspended the intact axoneme pellet in Cilia Final Buffer to a concentration of 4 mg/mL.

3.2 Methods – Cryo-ET sample preparation of *Tetrahymena* cilia

All cryo-EM sample preparation, screening, and data collection were performed at the Facility for Electron Microscopy Research (FEMR). Cryo-EM sample preparation, data screening, and data collection would not be possible without the assistance of Dr. Kaustuv Basu (Titan Krios operator) and Dr. Kelly Sears (research manager).

I treated C-Flat Holey thick carbon grids (Electron Microscopy Services #CFT312-100) with chloroform and left them to dry overnight. The grids were negatively glow discharged for 15 seconds at 10 mA (EMS100x Glow Discharge Unit, Electron Microscopy Sciences). Vitrobot Mk IV was used for vitrification (Thermo Fisher Scientific).

To maintain the native structure of the axoneme during cryo-EM grid application and vitrification, I needed to crosslink the intact axonemes. I added 25% glutaraldehyde to a final concentration of 0.15% and incubated the sample on ice for 40 minutes followed by the addition of 1 M HEPES (3X volume of glutaraldehyde) to quench the crosslinking reaction. I then diluted the intact, crosslinked axonemes to approximately 3.6 mg/mL. Lastly, I added 10 nm gold beads conjugated to protein A in a 1:1 ratio such that the final

concentration of the axonemes was approximately 1.8 mg/mL. I applied 4 μL of sample at 1.8 mg/mL to the grid, which was subsequently incubated for 15 seconds in a 100% humidity chamber at 22°C. The grid was blotted with a calibrated blot force of 1 for 3 seconds, plunge frozen in liquid ethane and stored in liquid nitrogen.

3.3 Methods – Cryo-ET data collection

I screened the samples using an FEI Tecnai G2 F20 200 kV Cryo-STEM (FEMR).

The purpose of the screen was to ensure the sample was ready for cryo-ET data collection. There were several important characteristics that I needed to observe before attempting data collection. I was looking for a grid that had a thin layer of vitreous ice, as well as a sufficient number of round, unperturbed axonemes in the holes of the TEM grid. I also needed to make sure the fiducial markers were sufficiently abundant and evenly distributed throughout the holes of the grid. Even if the sample was otherwise perfect, insufficient gold particles would cause the tracking to fail during tomogram data collection and limit downstream tomogram reconstruction. If the crosslink treatment failed, then I might see axonemes that are unusually wide because the surface tension during cryo-ET sample preparation flattened the axonemes. If the sample was too concentrated, perhaps the vitreous ice would be too thick which reduces high resolution information obtained during data collection; or maybe the high concentration would mean axonemes are overlapping so there are less unobstructed particles for downstream processing. If the sample was too dilute, there might not be enough particles for downstream processing. Once two grids passed the screen, I proceeded with data collection.

Cryo-EM data were collected on a Titan Krios 300 keV FEG electron microscope (Thermo Fisher Scientific) equipped with a direct electron detector K3 Summit (Gatan, Inc.) and the BioQuantum energy filter (Gatan, Inc.) and SerialEM software.[182] Tilt series were collected from -60° to +60° at 3° increments using a dose-symmetric tilt-scheme. Movies for each view consisted of 10-13 frames. Data were collected at a magnification of 42000 X and a pixel size of 2.12 Å. The total dose for each tilt series was 160 electrons per $Å^2$ and a defocus range of –3.5 to –2.5 µm (Table 2.2).

3.4 Methods – Cryo-ET data processing

I aligned the frames of each tilt series using Alignframes software,[229] which is part of the IMOD software package.[230] I then manually inspected each aligned tilt series and excluded tilt series with poor quality, insufficient tilt angles, and insufficient fiducials.

For all tomograms that passed the screen, I reconstructed them with the batchruntomo program using the Etomo interface,[229] which is part of the IMOD software package. For every reconstruction, to varying degrees, I provided manual input to supplement the fiducial tracking that would occasionally fail throughout the tilt series. I would also exclude tilt frames that lost fiducials. I then continued the batchruntomo program to finish reconstructing all of the tomograms. I ended up with 58 reconstructed tomograms for *Tetrahymena* strain *CU428* and 20 reconstructed tomograms for *CFAP77A/B-KO* (Table 2.2). These tomograms were used for both subtomogram averaging and visualization.

To generate subtomogram averaged cryo-ET density maps with optimal resolution, I needed to have accurate CTF estimation, good particle picking, and an optimal subtomogram averaging and cryo-ET map refinement workflow. I used the tilt series pre-

processing pipeline in the WARP program[231] for CTF estimation of every tilt series. I imported each tilt series into WARP, along with a corresponding gain reference and parameters related to frames, tilt angles, and exposure dose information. I followed the standard WARP tilt series pre-processing workflow: motion correction and CTF estimation of each frame of the tilt series, then IMOD alignment of each tilt series, then CTF estimation of each tilt series. After I exported the CTF estimation parameters, I converted it into CTFFIND format so it is compatible with Relion 4.0 software[163] and sent a copy of each CTF parameter to its corresponding tomogram directory.

Using IMOD software, I went through every reconstructed tomogram and manually picked all the DMTs from the axonemes by defining start and end points within the tomographic volumes. All of the particles were picked from the base to the tip in relation to the direction of the axoneme. Axoneme Align[232] is an open-source software consisting of approximately 15 scripts, some ran iteratively, for subtomogram averaging of axonemal DMTs. Through a series of particle alignments, re-picking of particles, and particle averaging, Axoneme Align was ran to generate an 8-nm, a 16-nm, and finally a 96-nm subtomogram average from all of the DMTs picked from all tilt series.[232] This was done for both *Tetrahymena* strains *CU428* and *CFAP77A/B-KO*.[142]

Using the merged 96-nm particles from Axoneme Align, I ran a script to generate two .star files; one contained information for all coordinates of the particles of the subtomogram average, and the other connected the coordinates to the directories of the reconstructed tomograms. Importantly, each directory also contained CTF estimations from WARP.

I imported those two .star files into Relion 4.0 software for refinement of the subtomogram averaged maps. There were 2608 and 1702 subtomograms averaged for the *CU428* and *CFAP77A/B-KO* DMTs, respectively. I followed the subtomogram analysis workflow and obtained resolutions of 18 Å and 21 Å for 96-nm subtomogram averaged density maps of the DMTs for *CU428* and *CFAP77A/B-KO*, respectively.[142]

For visualization of the reconstructed tomograms, I used the deep learning-based software IsoNet.[233] After training on a related dataset, IsoNet improves structural interpretability of reconstructed tomograms through CTF deconvolution, missing wedge correction, and denoising of the reconstructed tomograms. I ran IsoNet on 20 randomly chosen reconstructed tomograms for *CU428* and all 20 tomograms of *CFAP77A/B-KO*.

As a check for quality and shape, I compared some reconstructed tomograms from crosslinked *CU428* and *CFAP77A/B-KO* axonemes with previously reconstructed tomograms of non-crosslinked *CU428* axonemes. The only difference observed was that non-crosslinked axonemes were less round, likely due to deformity caused by surface tension at the air-water interface.[234]

Visualization of the subtomogram averaged maps of *CU428* and *CFAP77A/B-KO* DMTs was done in ChimeraX.[235]

3.5 Methods – Coarse-grained molecular dynamics simulations and angular elasticity

Postdoctoral fellow Dr. Shintaroh Kubo performed all molecular dynamics (MD) simulations.[142] Coarse-grained MD simulations were performed using CafeMol software.[236] From the DMT, only OJ PFs A10-A12 and B1-B2 were used, as well as OJ2 and CFAP77A. Each amino acid was represented as a single bead at the Cα position.

The energy function of the AICG2+ model, electrostatic and excluded volume interactions were used to predict dynamics.[237] Dr. Kubo then ran coarse-grained MD simulations 20 times each to simulate OJ stability with and without OJ2 and CFAP77 molecules.[142]

For the angular elasticity calculations, the center point used to create two vectors was lysine 401 of the central α-tubulin in PF A10. From there, a vector was made to lysine 401 of the central α-tubulin in PF A12 as well as PF B2.[142]

3.6 Methods – CFAP77 gene knock-ins and knock-outs in *Tetrahymena*

Scientists Dr. Ewa Joachimiak and Dr. Dorota Wloga performed all CFAP77 gene knock-ins and knock-outs in *Tetrahymena*.[142] Using an existing plasmid with a 3HA fusion gene and neo4 resistance cassette used for a study that targeted CFAP44,[238,239] they engineered CFAP77A-3HA and CFAP77B-3HA plasmids. These plasmids allow for both (i) the expression of the C-terminally 3HA-tagged CFAP77 paralogs under the control of their own promoters and (ii) the selection of positive clones based on resistance to paromomycin.[238,239]

For CFAP77A and CFAP77B gene knockout, the Wloga lab used the germline gene disruption approach.[59,240] Fragments of the targeted genes with added restriction sites were exploited for subsequent deletion of each CFAP77 paralog gene. For the *CFAP77A/B-KO* double knockout strain, the *CFAP77A-KO* and *CFAP77B-KO* heterokaryotic strains were crossed.[57] For every knockout mutant, at least two independent clones were generated and maintained.

3.7 Methods –Phenotypic and localization studies of *Tetrahymena* wild-type and CFAP77-KO mutant strains

Scientists Dr. Ewa Joachimiak and Dr. Dorota Wloga performed all phenotypic and localization studies of *Tetrahymena* wild-type and CFAP77-KO mutant strains.[142]

Swimming was analyzed using video of *Tetrahymena* cells recorded with a Zeiss Discovery V8 Stereo microscope (Zeiss, Germany) equipped with Zeiss Plans 10× FWD 81 mm objective and Axiocam 506 camera and ZEN2 (blue edition) software.[241]

Cilia length, ciliary beating, waveform, and amplitude were analyzed using high-speed videos of *Tetrahymena* cells recorded with a high-speed camera (Andor Zyla 5.5 sCMOS) mounted on a Leica DMI 6000 microscope (63x oil immersion lens, numerical aperture 1.4) with an Andor DsD2 unit.[241]

For localization experiments, *Tetrahymena* cells were applied to coverslips and then fixed using a mixture of NP-40 and PFA in PHEM buffer or Triton-X-100 and then PFA.[142] Cells were incubated with anti-HA antibodies (Cell Signaling Technology, Danvers, MA, USA), washed, incubated with polyG antibodies,[241] washed, and then incubated with secondary antibodies (anti-mouse IgG conjugated with Alexa-488 and anti-rabbit IgG conjugated with Alexa-555 (Invitrogen, Eugene, OR, USA).[142] The coverslips were then mounted in Fluoromount-G (Southern Biotech, Birmingham, AL, USA) and viewed using a Zeiss LSM780 (Carl Zeiss Jena, Germany) or Leica TCS SP8 (Leica Microsystems, Wetzlar, Germany) confocal microscope. Expression of the 3HA-tagged CFAP77 paralogs was verified by Western blot.[142] Table 3.1 contains all antibodies used in this thesis.[142]

Table 3.1. Antibodies used in this thesis. Adapted from Kubo *et al.*, 2023.[142]

Antibody	Source
HA-Tag (C29F4) Rabbit mAb	catalog number #3724 (Cell Signaling Technology)
Goat anti-Mouse IgG	catalog number #A-10680 (Invitrogen)
Goat anti-Rabbit IgG	catalog number #A-21428 (Invitrogen)
Rabbit anti-polygly	catalog number #ABPEP-20 (Alpha Diagnostic International, San Antonio, TX). [242]
GT335 polyE anti-polyglutamate primary antibody	no catalog number available.[243]
12G10 Mouse anti-alpha-tubulin mAb	catalog number #nAB_1157911 (DSHB).[244]

3.8 Methods – Quantification of polyglutamylation in *Tetrahymena* wild-type and CFAP77-KO mutant strains

Scientists Dr. Ewa Joachimiak and Dr. Dorota Wloga performed all quantifications of polyglutamylation in *Tetrahymena* wild-type and CFAP77-KO mutant strains.[142] Wild-type and *CFAP77A/B-KO* cells were fixed according to Wloga *et al.*, 2006,[245] and both cell strains were stained with polyE anti-polyglutamic acid primary antibody.[142] Wild-type and *CFAP77A/B-KO* cells were placed close to each other on a slide and imaged with a confocal microscope.[142] The intensity of the polyE signal in wild-type and *CFAP77A/B-KO* cilia was measured using the ImageJ program.[246]

The Wloga lab performed western blotting according to Janke *et al.*, 2005.[247] The following primary antibodies were used: GT335 anti-glutamylated tubulin mAb; 12G10 anti-α-tubulin mAb; and polyE antibodies (Table 3.1). ImageJ software was used to measure the intensity of the bands that were detected. The data were then visualized as a graph that shows the ratio of glutamylated tubulin to α-tubulin.[142]

3.9 Results and discussion

3.9.1 Overview of the *Tetrahymena* outer junction proteins

I identified and modeled the OJ MIPs CFAP77 and OJ2 in *Tetrahymena* cilia (Fig. 3.1A, B). I also de novo modeled a backbone trace of the MT surface protein OJ3 (Fig. 2.2, Fig. 2.4F and Fig. 2.7B). OJ3 is an MAP positioned at A10-B1 and may function in IFT regulation (Fig. 3.1B). OJ3 spans 24 nm, or 3 β- and α-tubulin heterodimers (Fig. 3.1B). The structure of OJ3 consists of 4 α-helices interspersed with intrinsically disordered regions (Fig. 3.1B). The 4 OJ3 α-helices range from 18-28 amino acids, and the total α-helical content represents approximately 16 nm of the 24 nm length (Fig. 3.1B). There are similar filamentous densities at A10-B1 in the cryo-EM maps of DMTs from *Chlamydomonas* flagella (EMD-20631) and bovine respiratory cilia (EMD-24664), but they have not been identified.[16,19] Regulation of IFT is essential for cilia growth and maintenance.[248] *Tetrahymena* OJ3 and the similarly positioned filamentous proteins from *Chlamydomonas* flagella and bovine respiratory cilia are likely functional homologs even if they are not conserved.

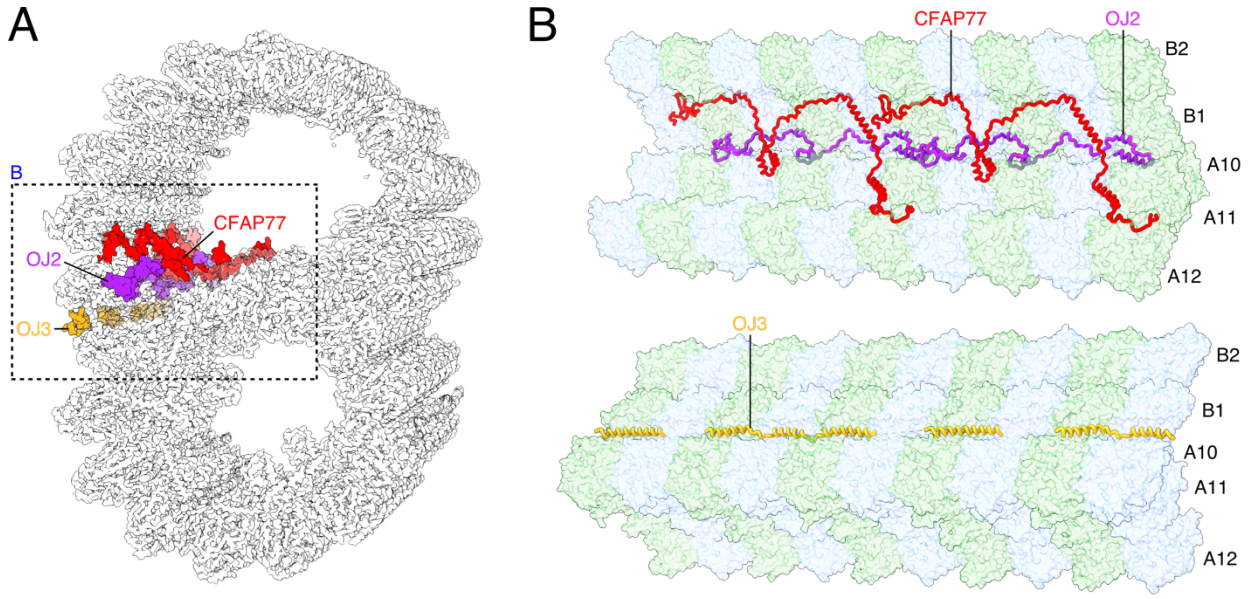

C

TtCFAP77A	... N R T Q N T L L L K	22	... R D F A K L N K M S L T Q G L H K S N Q F S D Y R K 98
TtCFAP77B	... R N K H N K L L L K	22	... R D F L K L N R D C I K D K C F N A K E I S R Y R D 98
HsCFAP77	... S M F Q N P L I V K	65	... R N Y I A M N R G A V K A G L V T A R E N L L Y R Q 179
BtCFAP77	... S M F Q N P L I V K	65	... R N Y I A M N R G A V K A G L V T A R E N L H Y R Q 143
CrCFAP77	... S M N Q N P L L A H	35	... P D F K T L N K M A V A S G L S T A K D L P A F R K 112

α helix — Helix 1 — Helix 2 — Helix 3

D

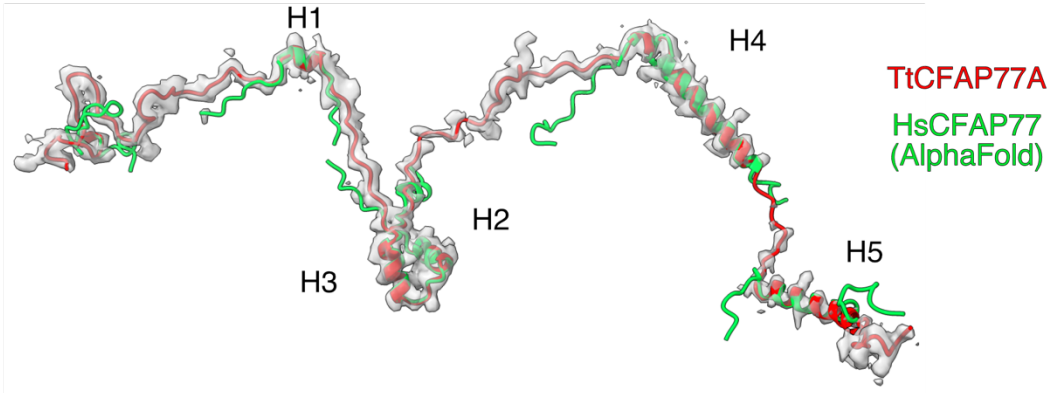

Figure 3.1. The *Tetrahymena* outer junction is occupied by the conserved CFAP77 and species-specific OJ2. (A) Cross-sectional view of the *Tetrahymena* OJ highlighting proteins CFAP77 (red), OJ2 (purple) and OJ3 (yellow). **(B)** Architecture of the *Tetrahymena* OJ, including the proteins CFAP77, OJ2 and OJ3. **(C)** Multiple sequence alignment of a segment of CFAP77. Human (Hs), bovine (Bt), and *Chlamydomonas* (Cr) sequences as well as two orthologs of *Tetrahymena* (Tt) were included. **(D)** Cryo-EM model of *Tetrahymena* TtCFAP77A. Folded regions of the AlphaFold2 model of human CFAP77 (green) were fitted into the map used to model the *Tetrahymena* protein. Adapted from Kubo *et al*., 2023.[142]

The lumen of the *Tetrahymena* OJ is occupied by CFAP77 and OJ2, which weave along several tubulin PFs (Fig. 3.1B). CFAP77 and OJ2 are 28.9 kDa and 19.9 kDa MIPs, respectively. Unlike the filamentous 24-nm periodicity of OJ3, CFAP77 and OJ2 have 16-nm periodicities and span approximately 5 β- and α-tubulin subunits (Fig. 3.1B). When I examined the 48-nm cryo-EM maps of DMTs from *Chlamydomonas* flagella and bovine respiratory cilia, I observed convincing cryo-EM densities for CFAP77 in both maps. I did not observe a density for OJ2 in either map. Furthermore, bioinformatics analysis revealed that parasitic ciliate proteomes have an OJ2 homolog, but OJ2 is not evolutionarily conserved in other organisms.

OJ2 and CFAP77 were identified by searching our mass spectrometry database of *Tetrahymena CU428* DMTs using regular expression patterns of amino acid side chains that were modeled in the cryo-EM map. A BLAST search[249] of CFAP77 revealed bioinformatically that *Tetrahymena* has two paralogs of CFAP77, likely a result of a gene duplication that is common to the organism. When I looked at the mass spectrometry data of *Tetrahymena CU428* DMTs, I found two paralogs of CFAP77: CFAP77A and CFAP77B (Table 2.3). CFAP77A was twice as abundant as CFAP77B in the mass spectrometry data, and all 4 cryo-EM densities for CFAP77 along the 48-nm averaged cryo-EM map

were the same (Table 2.3). Sequence similarity was approximately 60% by pairwise sequence alignment[250] and ColabFold-predicted structures of CFAP77A and CFAP77B were too similar to differentiate with the resolution of the cryo-EM map. Since it was not possible to model each paralog separately, I modeled only the structure of CFAP77A. For the rest of this thesis, "CFAP77" refers to "CFAP77A" unless explicitly stated. CFAP77 interacts with the OJ PFs A12, A11, B1, and B2; OJ2 interacts with PFs A11 and B1 (Fig. 3.1B).

CFAP77 is an evolutionarily conserved OJ MIP found in most organisms with motile cilia or flagella (Fig. 3.1C). However, CFAP77 has not been detected by mass spectrometry in mammalian primary cilia.[251] In the roundworm *Caenorhabditis elegans*, the only ciliated cells are sensory neurons which have primary cilia.[52] There is no evidence for an orthologous gene in *C. elegans* that encodes for CFAP77. To illustrate the structural and evolutionary conservation of CFAP77, I was able to fit the model of the ColabFold-predicted structure of human CFAP77 into the cryo-EM density of *Tetrahymena* CFAP77 (Fig. 3.1D).

3.9.2 Structural evidence for CFAP77 and OJ2 stabilizing the *Tetrahymena* outer junction

In 1979, it was discovered that Taxol, a diterpene compound extracted from the bark of the Pacific yew tree, was an effective cancer drug.[252] Taxol binds to a lumen-facing hydrophobic pocket of β-tubulin subunits, which induces hyper-stabilization of cellular MTs.[253,254] Both CFAP77A and OJ2 interact with β-tubulin taxane-binding sites. The first MIP discovered to bind to β-tubulin taxane-binding sites was RIB43A.[17] In *Tetrahymena*, cryo-EM studies revealed RIB43A-short occupied taxane-binding sites along the ribbon

PF arc, stabilized the MT and induced curvature in the MT wall.[17] Taxol-stabilized MTs had previously been observed to exhibit similar deformation to the MT lattice structure.[255] The model of *Tetrahymena* OJ2 contains unstructured regions, two short 2-turn α-helices, and a longer C-terminal α-helix (Fig. 3.2A). Each molecule of OJ2 threads along PFs A11 and B1 and interacts with the taxane-binding site of one β-tubulin subunit from the B1 PF of the B-tubule (Fig. 3.2Biv). The model of CFAP77A has one short 2-turn α-helix, two 4-turn α-helices, a helix-turn-helix motif, and a C-terminal α-helix (Fig. 3.2A). One CFAP77A molecule interacts with two β-tubulin subunits from the B2 PF of the B-tubule (Fig. 3.2Bi, ii). Specifically, the two 4-turn α-helices of CFAP77A each occupy a taxane-binding site of a β-tubulin subunit (Fig. 3.2Biii). In the *Tetrahymena* axoneme, almost every taxane-binding site of β-tubulin of PF B2 is occupied by CFAP77A; every second taxane-binding site of β-tubulin of PF B1 is occupied by OJ2 (Fig. 3.2A).

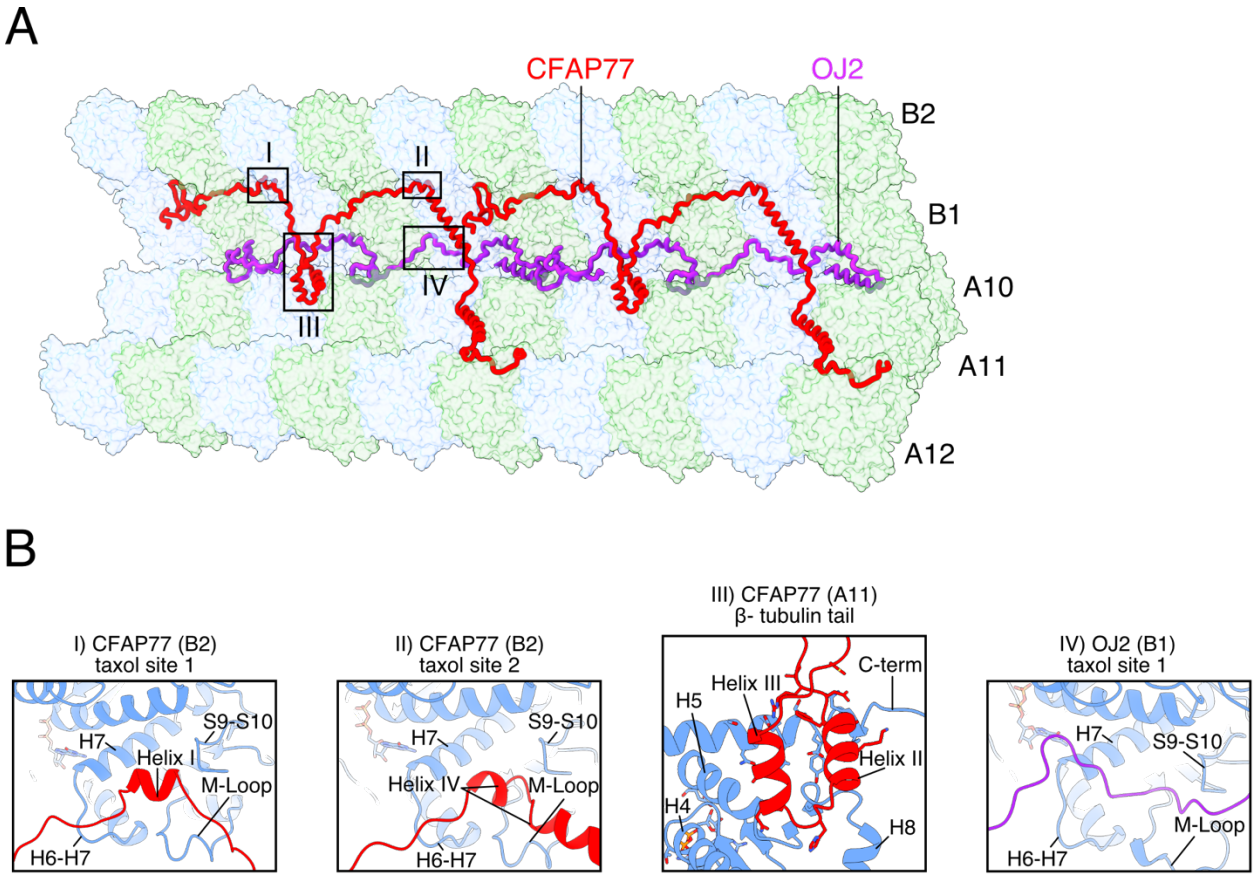

Figure 3.2. Structural evidence for CFAP77A and OJ2 stabilizing the outer junction. **(A)** Architecture of the *Tetrahymena* OJ, including the proteins CFAP77A and OJ2. **(B)** Helices of CFAP77 occupy taxane-binding pockets of β-tubulin of PF B2. A loop of OJ2 occupies the taxane-binding pocket of β-tubulin of PF B1. The helix-turn-helix motif of CFAP77 is positioned near the C-terminus of β-tubulin of PF A11. Adapted from Kubo *et al.*, 2023.[142]

CFAP77 and OJ2 appear more integrated into the OJ than the taxane-binding site interactions with the B-tubule. *Tetrahymena* CFAP77A and OJ2 have isoelectric points (pI) of 9.49 and 9.56, respectively. The pI values of *Tetrahymena* β- and α-tubulin are 4.79 and 5.01, respectively. Under physiological conditions, *Tetrahymena* has an intracellular pH that is maintained near 7.1.[256] In the *Tetrahymena* cilium, CFAP77A and OJ2 surfaces are electrostatically positive, while tubulin surfaces are relatively

electronegative (Fig. 3.3A, B). In addition to the taxane-binding site interactions, I think OJ MIPs CFAP77A and OJ2 interact with tubulin electrostatically.

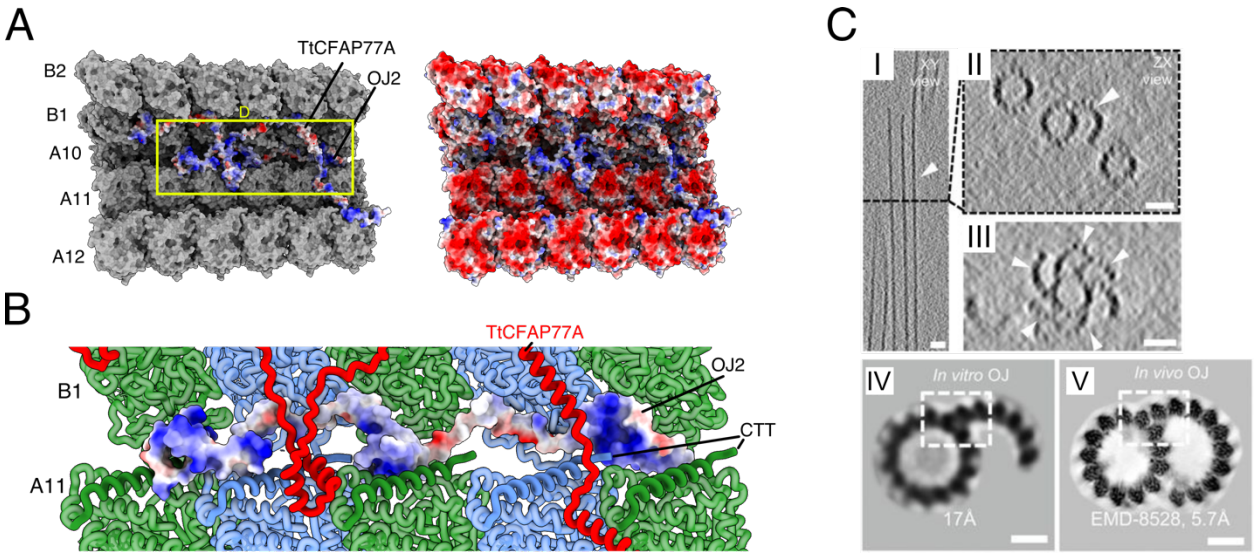

Figure 3.3. CFAP77A and OJ2 were hypothesized to interact with the C-terminal tails of β-tubulin through electrostatic interactions at the outer junction. Cleavage of the C-terminal tails of β-tubulin allows for partial DMT formation *in vitro*. (A) Electrostatic potential of the OJ proteins TtCFAP77 and OJ2. **(B)** Electropositive grooves of OJ2 are proximal to the β-tubulin C-terminus of PF A11. Adapted from Kubo *et al.*, 2023.[142] **(C)** Cryo-EM reconstruction of *in vitro* assembled partial DMTs from porcine tubulins. (I) Representative image of a cryo-ET section. Scale bar, 25 nm. (II) zx view of a cryo-ET section. Scale bar, 25 nm. (III) zx view of a cryo-ET section showing an DMT flower. Scale bar, 25 nm. Arrowheads in (A) to (C) indicate B-microtubules. (IV) Subtomogram averaging of in vitro DMTs at 17-Å resolution (IV) and of *Tetrahymena* ciliary DMTs at 5.7 Å (EMD-8528 map from the Electron Microscopy Data Bank) (V). Scale bars, 25 nm. Adapted from Schmidt-Cernohorska *et al.*, 2019.[74]

Interestingly, partial DMTs have been reconstituted *in vitro* using only tubulin (Fig. 3.3C).[74] Incubation of free tubulin with subtilisin-treated *in vitro* polymerized MTs was sufficient for the nucleation of multiple B-tubule “hooks” on the surface of the singlet MT (Fig. 3.3C).[74] These experiments demonstrated that manipulation of the tubulin C-terminal tails of the A-tubule is important for DMT formation. With that in mind, I examined the models of CFAP77A and OJ2 for possible interactions with C-terminal tails of β-tubulin along the A-

tubule. The last 10 or so amino acids of the C-terminal tails of β- and α-tubulin were not modeled because of flexibility owing to intrinsic disorder. The CFAP77 helix-turn-helix is positioned atop a β-tubulin C-terminal α-helix and tail region of PF A11 (Fig. 3.3B). OJ2 has two separate electronegative pockets that are proximal to two β-tubulin C-terminal tail regions on PF A11 (Fig. 3.3B).

An unstructured loop of OJ2 forms the first pocket, which is near the same C-terminal tail region as the CFAP77 helix-turn-helix (Fig. 3.3B). The second electronegative pocket is proximal to the next β-tubulin C-terminal tail (Fig. 3.3B). Thus, every β-tubulin C-terminal tail of the OJ PF A11 is proximal to either both CFAP77A and OJ2 or just OJ2. I hypothesize that CFAP77 and OJ2 are important for assembly of the OJ and stability of the DMT through B-tubule taxane-binding site interactions and electrostatic interactions with β-tubulin C-terminal tails of the A-tubule. I previously hypothesized that one or more proteins may be responsible for suppressing tubulin C-terminal tails during DMT formation in cilia.

The cryo-EM density for CFAP77 was observed in 48-nm cryo-EM maps for *Chlamydomonas* flagella, bovine respiratory cilia, *Tetrahymena* cilia, and mammalian sperm.[16,19,20,151] Unlike *Tetrahymena* DMTs, the OJ of mammalian sperm appears to be occupied by CFAP77 alone (Fig. 3.4). Proximal to the OJ are CCDC105 and TEX43, which are positioned on the B-tubule side of the ribbon PF arc A11-A12 (Fig. 3.4). CCDC105 and TEX43 are mammalian-specific MIPs but interact with the C-terminal tails of β- and α-tubulin along the A-tubule near the OJ. Similar to how CFAP77 and OJ2 likely

function to stabilize the OJ and suppress C-terminal tails of tubulin, so too might CCDC105 and TEX43 in mammalian sperm flagella.

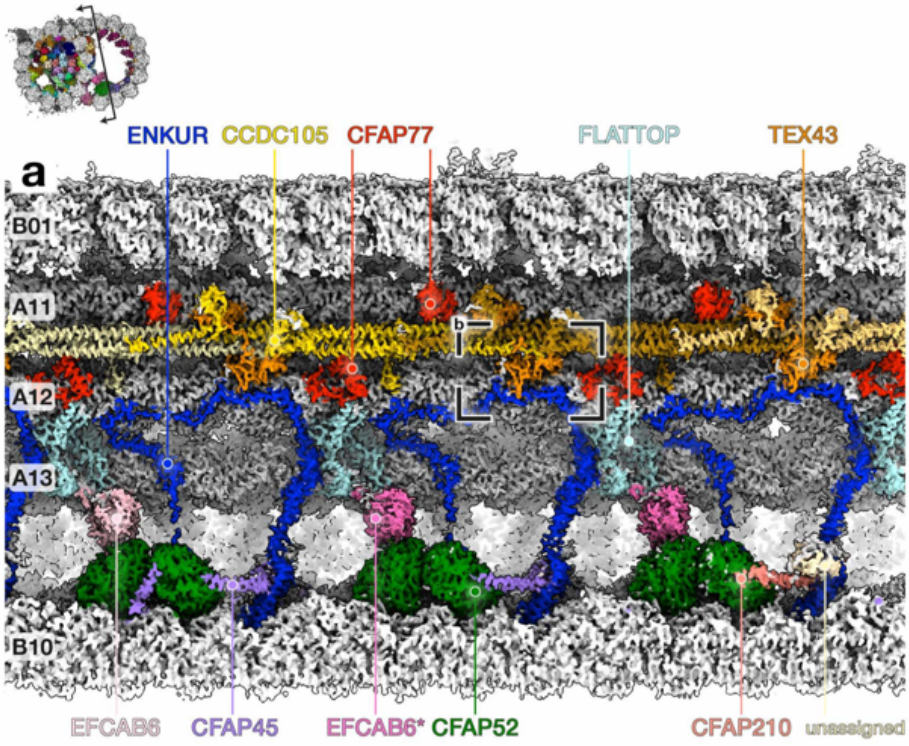

Figure 3.4. Sperm-MIPs at the ribbon interact with tubulin C-terminal tails. (A) Cryo-EM map of the ribbon and inner junction of sperm DMTs with MIPs colored individually. Each protomer in the CCDC105 filament is colored separately for clarity. Adapted from Leung *et al.*, 2022.[20]

At the OJ, PF B1 of the B-tubule must make non-canonical interactions with PF A11 of the A-tubule, which has already made lateral interactions with PFs A10 and A12 (Fig. 3.5A). The interactions of tubulin at the OJ involve the M-loops of tubulin from PF B1 and loops H9-S8 and H10-S9 of tubulin from PF A11 (Fig. 1.3C and Fig. 3.5A, B). In our model of the *Tetrahymena* DMT, OJ2 was observed at the tubulin interface of PFs B1 and A11 (Fig. 3.5B). Based on the protein structure model, the IntPred algorithm predicted that the

OJ2 C-terminal α-helix interacts with the M-loop of α-tubulin from PF B1 as well as the H9-S8 loop of α-tubulin from PF A11 (Fig. 3.5B).

These observations have provided a structural basis for CFAP77 and OJ2 functioning to assemble and stabilize the OJ in *Tetrahymena* DMTs. The proximity and attractive electrostatic forces of CFAP77A and OJ2 to the β-tubulin C-terminal tails of PF A11 suggest that it is possible that these MIPs suppress C-terminal tails during OJ formation (Fig. 3.3B). The binding of taxane-binding sites of β-tubulin along PFs B1 and B2 suggests that CFAP77A and OJ2 stabilize the OJ (Fig. 3.2B). Finally, OJ2 may strengthen the interactions between α-tubulin from PFs B1 and A11 along the OJ (Fig. 3.5B). Throughout the rest of this thesis, I will present research focused on understanding the function of the OJ proteins CFAP77A and OJ2.

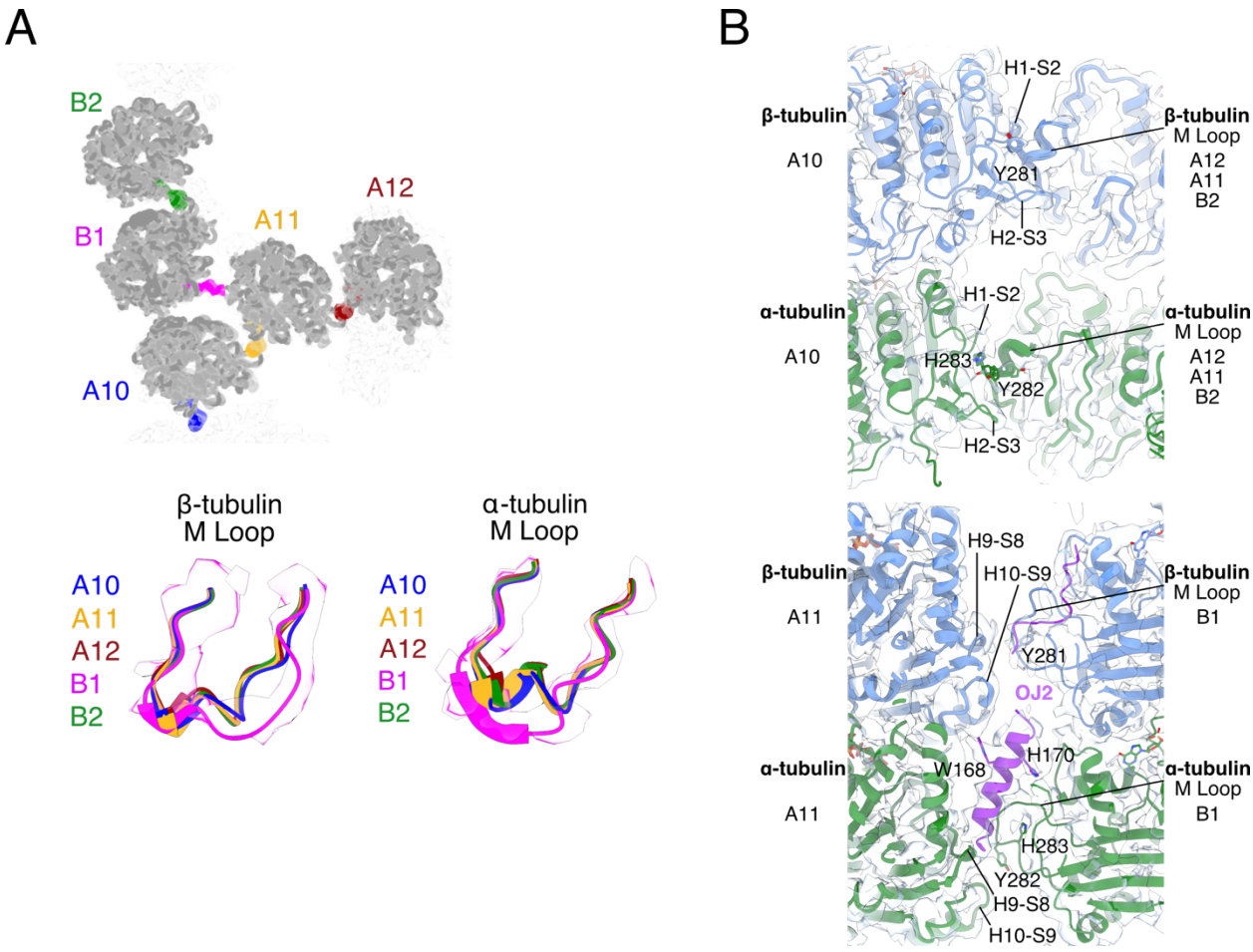

Figure 3.5. CFAP77 stabilizes the outer junction. (A) Top: Cross-sectional view of the OJ. M-loops of tubulins are colored according to protofilament: B2 (green); B1 (purple); A10 (blue); A11 (gold); A12 (dark red). Bottom: those same M-loops are superimposed. **(B)** The canonical (top) and unique (bottom) lateral interactions between tubulin subunits. Protofilaments A11, A12, and B2 are superimposed and adopt the same overall conformation and lateral interactions (top). The lateral interactions between B1 and A11 are particularly unique in *Tetrahymena* because they involve OJ2 (bottom). Adapted from Kubo *et al.*, 2023.[142]

3.9.3 Molecular dynamics demonstrate that CFAP77 and OJ2 stabilize the outer junction

After thoroughly inspecting the model of the OJ, I found structural evidence that CFAP77A and OJ2 were important for stabilizing the DMT. A multidisciplinary approach was needed to properly investigate my findings. The first question that I asked was how tubulin PFs at the OJ respond to the presence and absence of CFAP77A and OJ2. With the model of

the *Tetrahymena* OJ readily available, postdoctoral fellow Dr. Shintaroh Kubo performed coarse-grained molecular dynamics simulations (Fig. 3.6A). In the simulation experiments, CFAP77A, OJ2, and PFs A10-A12 of the A-tubule and B1-B2 of the B-tubule were included (Fig. 3.6A). CFAP77A and OJ2 dramatically lowered the interaction energy of the OJ PFs by approximately -6 kcal/mol (Fig. 3.6A, B). In the absence of CFAP77A and OJ2, the B-tubule tubulin dissociates from the A-tubule (Fig. 3.6A). Interestingly, the interaction energy of the OJ was the lowest at approximately -7 kcal/mol with OJ2 alone; however, the interaction energy changed by only 3.3% (+0.21 kcal/mol) for CFAP77A with or without OJ2 (Fig. 3.6B). Furthermore, CFAP77A lowered the interaction energy of the B-tubule PFs by 11% more than OJ2, indicating that CFAP77A contributes the most to the stability of the B-tubule (Fig. 3.6B).

A

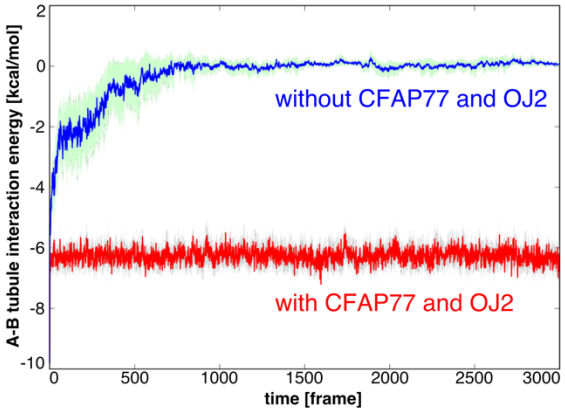

C

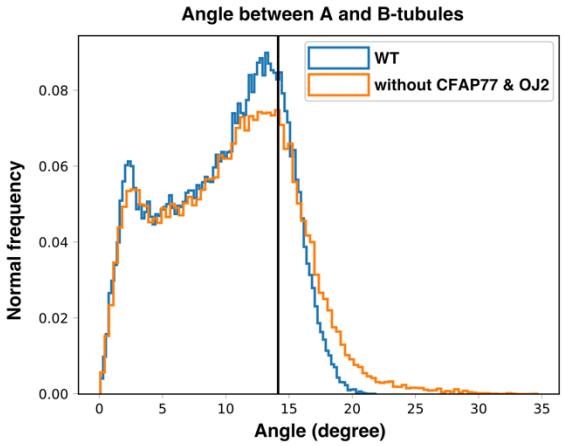

B

Average energy between A- and B-tubules		
	With OJ2	Without OJ2
With FAP77	-6.2604 ± 0.00408215	-6.05342 ± 0.0055639
Without FAP77	-7.18253 ± 0.00409181	-0.290828 ± 0.00524678
Average energy between PFs B1 and B2		
	With OJ2	Without OJ2
With FAP77	-30.2775 ± 0.00598608	-30.7353 ± 0.00608574
Without FAP77	-27.5101 ± 0.00881373	-26.6082 ± 0.00922062

Figure 3.6. Molecular dynamics simulations of CFAP77A and OJ2. (A) Molecular dynamics simulations of the OJ with and without CFAP77 and OJ2. **(B)** Stability of the OJ in the presence and absence of CFAP77 and OJ2 based on coarse-grained molecular dynamics simulations. **(C)** Frequency of angular elasticity for A- and B-tubules from our MD simulations. Adapted from Kubo *et al.*, 2023.[142]

Using molecular dynamics simulations, I was able to answer one more question: do CFAP77A and OJ2 affect the angular architecture of the OJ? The angular elasticity between the A- and B-tubules was calculated for the OJ PFs A10-A12 and B1-B2 with and without CFAP77A and OJ2. Angular analysis revealed that the angles of interactions between tubulin subunits were unstable in the absence of CFAP77A and OJ2 (Fig. 3.6C). Molecular dynamics simulations supported the structural observations that CAFP77A and OJ2 contribute to the stability of the OJ of the DMT in *Tetrahymena* (Fig. 3.6A, C). Of the two MIPs, only CFAP77A is evolutionarily conserved. I am now going to focus my investigation on the function of CFAP77 using both genetics and *in vitro* experiments.

3.9.4 CFAP77A and CFAP77B paralogs differentially localize in *Tetrahymena* cilia

One of the weak points in my investigation of CFAP77 has been the lack of information acquired on *Tetrahymena* CFAP77B. If nothing else, I wanted to know the localization of both CFAP77 paralogs in *Tetrahymena* cilia. This would inform me on the relative contribution of each paralog toward the stabilization of the DMT. Dr. Dorota Wloga and scientist Dr. Ewa Joachimiak of the Nencki Institute of Experimental Biology engineered CFAP77A-3HA and CFAP77B-3HA knock-in strains by transforming wild-type cells with an engineered plasmid vector.[238,239] Immunofluorescence microscopy revealed that CFAP77A and CFAP77B were differentially localized in *Tetrahymena* cilia (Fig. 3.7A). CFAP77A-3HA is highly abundant and localized to the proximal end of the cilium, while

CFAP77B-3HA is less abundant but is present along the entire length of the cilium (Fig. 3.7A). The localization experiment supported our mass spectrometry analysis showing that CFAP77A was approximately twice as abundant as CFAP77B (Table 2.3). We did not see either CFAP77 paralog localize to the ciliary distal tip, which consists of singlet MTs only.

3.9.5 Knockout of CFAP77 reduces *Tetrahymena* swimming and cilia length

Structural analyses and molecular dynamics simulations of the *Tetrahymena* OJ of the DMT revealed that CFAP77A and OJ2 may be important for OJ assembly and/or stability. I next wanted to investigate the function of evolutionarily conserved CFAP77 using a genetics approach. I wanted to know how knockout of CFAP77A and CFAP77B genes from *Tetrahymena* would impact ciliary functions like ciliary beating waveform and swimming speed. Dr. Wloga's lab genetically engineered three *Tetrahymena* knockout cell strains: CFAP77A, CFAP77B, and CFAP77A/B double knockout.[142] Using a germline gene disruption approach,[59,142,240] Dr. Wloga's laboratory removed the gene coding regions of CFAP77A, CFAP77B, or both CFAP77A and CFAP77B (Fig. 3.7B, C).

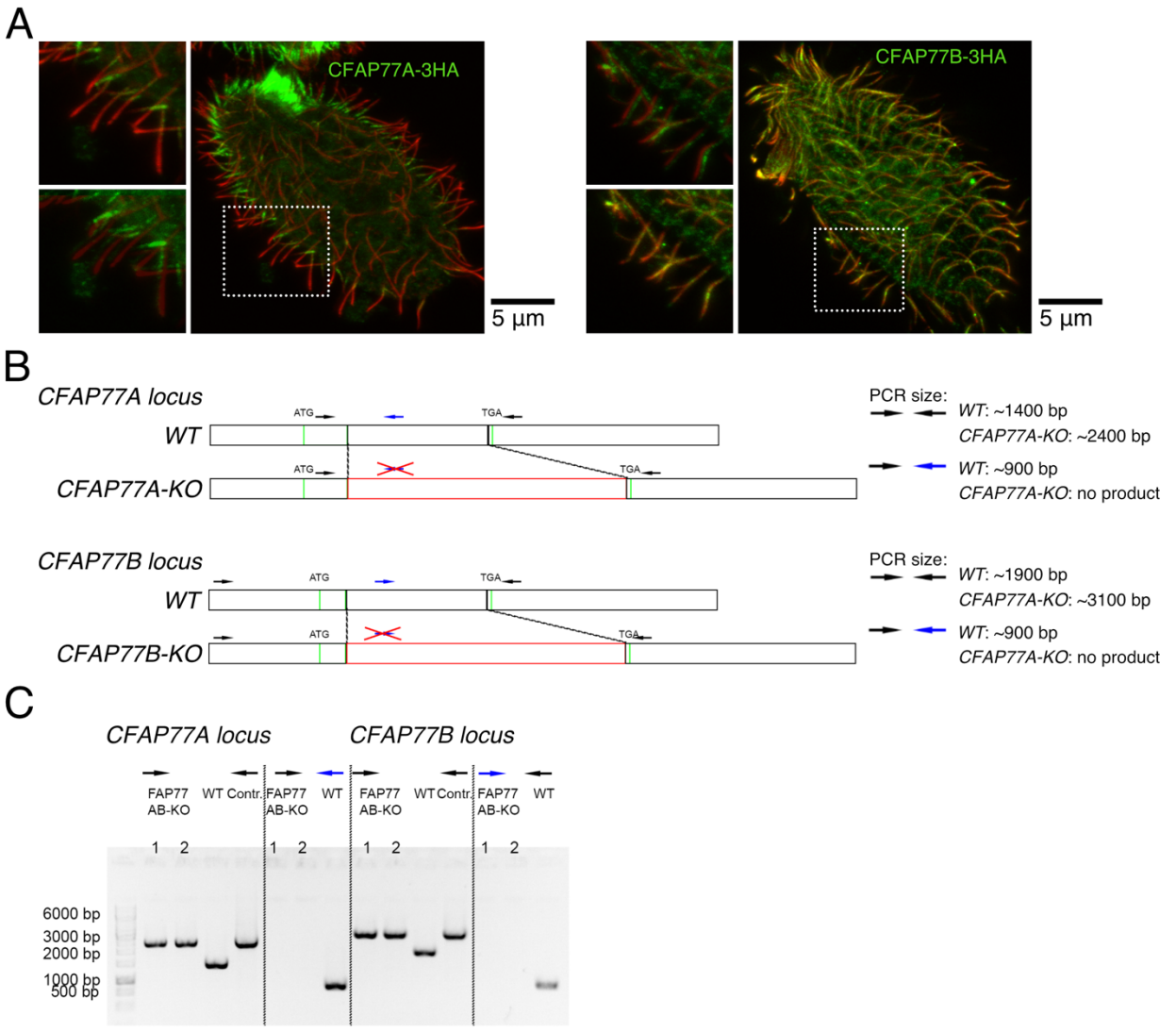

Figure 3.7. Knockout of CFAP77A/B caused mild defects in *Tetrahymena* cilia. (A) Differential localization of CFAP77A and CFAP77B in CFAP77A-3HA and CFAP77B-3HA knock-in mutants. Green—anti-HA; red—poly glycylated tubulin. **(B)** Homologous recombination methodology for CFAP77A and CFAP77B knockout strains. **(C)** PCR-based confirmation of the gene knockout. Adapted from Kubo *et al.*, 2023.[142]

The CFAP77 knockout *Tetrahymena* strains were observed to exhibit mild impaired swimming speeds when compared with healthy wild-type cells (Fig. 3.8A). The *Tetrahymena* CFAP77 knockout mutants all swam in straight trajectories similar to wild-type cells. The *CFAP77A-KO* and *CFAP77B-KO* cells traveled approximately 34% and

37% less than wild-type cells, respectively (Fig. 3.8A). *CFAP77A/B-KO* cells swam approximately 58% the distance of wild-type cells (Fig. 3.8A).

The ciliary beat frequency was reduced by approximately 40% in *CFAP77A/B-KO* cells, which explains why the double knockout mutant swims only approximately 42% of the distance of the wild type (Fig. 3.8B). Furthermore, infrequent asynchronous ciliary beating was observed in *CFAP77A/B-KO* cells (Fig. 3.8B). The ciliary waveform and amplitude of *CFAP77A/B-KO* cells were very similar to those of wild-type cells (Fig. 3.8C). The cilia length of *CFAP77A/B-KO* cells was approximately 10% shorter than that of wild-type cilia, indicative of a ciliary assembly defect (Fig. 3.8D). The shorter cilia length implies an assembly defect of *CFAP77A/B-KO* cells; this is exciting because it provides genetic evidence for CFAP77 functioning in the assembly of the DMT. To observe any assembly or structural defects in *CFAP77A/B-KO* cilia, I used cryo-ET to compare the axonemes and DMTs of *CFAP77A/B-KO* and wild-type cells.

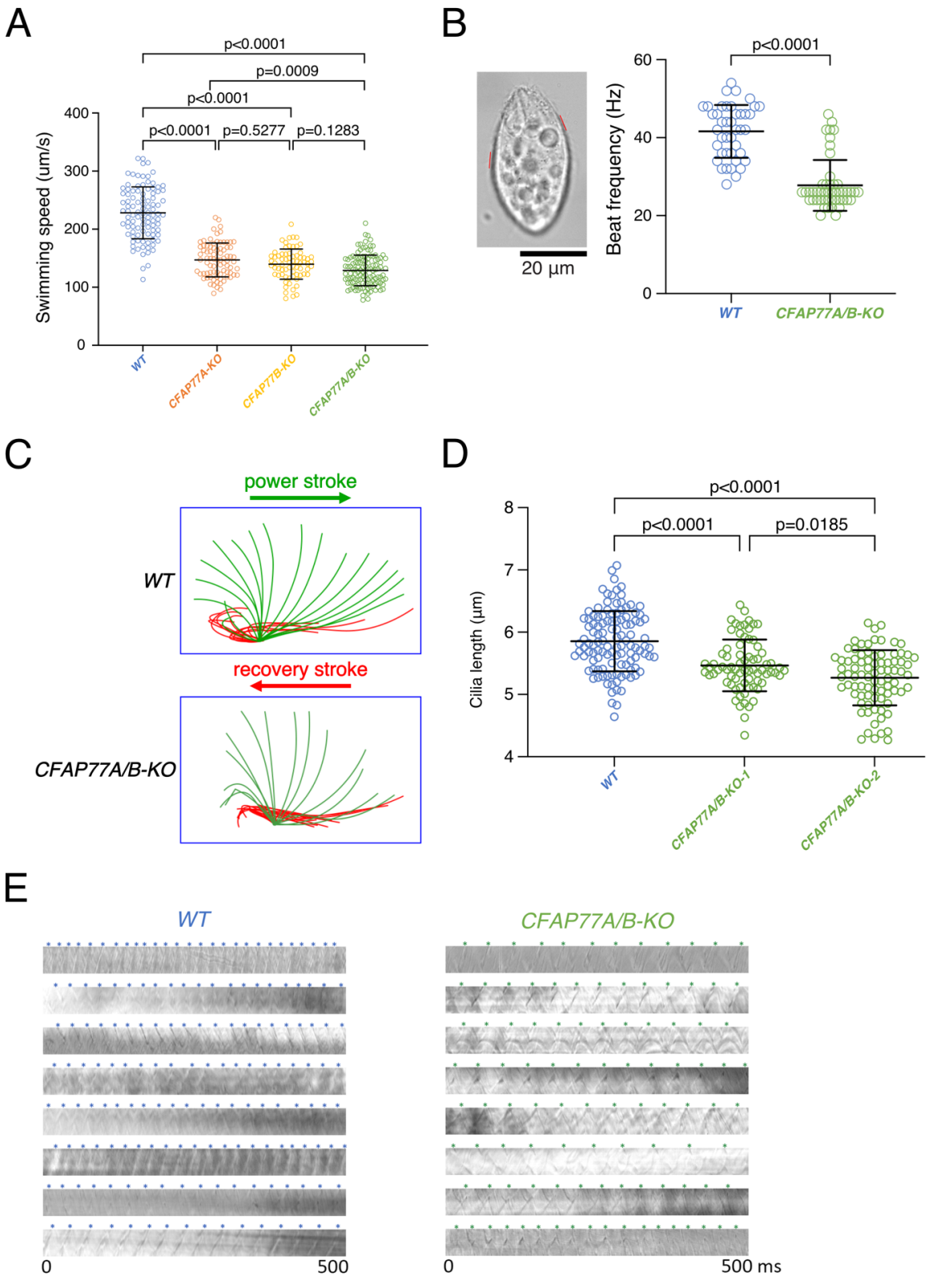
A
p<0.0001
p=0.0009
p<0.0001
p<0.0001
p=0.5277
p=0.1283
Swimming speed (um/s)
400
300
200
100
0
WT
CFAP77A-KO
CFAP77B-KO
CFAP77A/B-KO
B
20 µm
p<0.0001
Beat frequency (Hz)
60
40
20
0
WT
CFAP77A/B-KO
C
power stroke
WT
recovery stroke
CFAP77A/B-KO
D
p<0.0001
p<0.0001
p=0.0185
Cilia length (µm)
8
7
6
5
4
WT
CFAP77A/B-KO-1
CFAP77A/B-KO-2
E
WT
CFAP77A/B-KO
0
500
0
500 ms

Figure 3.8. Knockout of CFAP77A/B caused mild defects in cilia. (A) Knockout of CFAP77A or CFAP77B or both led to a 40% swimming speed reduction (n = 99 for WT, n = 81 for CFAP77A-KO, n = 70 for CFAP77B-KO, n = 119 for CFAP77A/B-KO). Statistical analyses were performed with two-sided Tukey's multiple comparisons tests. **(B)** *Tetrahymena* cells with marked exemplary positions (red lines) where cilia beat was analyzed in recorded swimming cells. Graphical representation of measurements of cilia beating frequency in WT and CFAP77A/B-KO mutants. (n = 42 cilia from 12 cells for WT, n = 48 cilia from 12 cells for CFAP77A/B-KO). Statistical analyses were performed with a two-sided Mann-Whitney comparisons test. **(C)** Lack of both CFAP77 paralogs does not apparently alter cilia beating amplitude and waveform. **(D)** Cilia length measurements of WT and CFAP77A/B-KO mutants. The average cilia length was as follows: WT =5.85 µm (number of measured cilia, n = 115), CFAP77A/B-KO clone 1 = 5.46 µm (n = 74), CFAP77A/B-KO clone 2 = 5.27 µm (n = 83). Student's t test WT/KO is 2E–08 and 6,8E–16, respectively. Data are presented as the mean values +/– standard deviation in **(A, B, D)**. **(E)** Examples of kymographs of cilia motility generated from each movie in ImageJ. Each wave peak (*) on a kymograph corresponds to cilia passing through the drawn line. Adapted from Kubo *et al.*, 2023.[142]

3.9.6 Knockout of CFAP77 disrupts the structure of the *Tetrahymena* axoneme

In this chapter, I used structural, computational, and genetic experiments to understand the molecular architecture and interactions of the OJ of *Tetrahymena* DMTs. I was excited to see the shorter cilia length of *CFAP77A/B-KO* cells because of the implication that loss of CFAP77 might lead to assembly defects. I was also curious about how CFAP77A and CFAP77B differentially localize and their roles in cilia. I used cryo- ET and subtomogram averaging to observe the structural consequences of CFAP77 loss on axonemes and DMTs.

I collected and processed tilt series of crosslinked axonemes for both *CFAP77A/B-KO* and wild-type cells. I then performed subtomogram averaging of the 96-nm repeating unit of DMTs from the axonemes of both *CFAP77A/B-KO* and wild-type cells. I also used IsoNet software for CTF deconvolution and missing wedge correction of the reconstructed tomograms for improved visualization. The 96-nm subtomogram averaged maps of the

CFAP77A/B-KO and wild-type DMTs were 22 Å and 19 Å in resolution, respectively (Fig. 3.9A, B). The subtomogram averaged maps of the *CFAP77A/B-KO* and wild-type DMTs were indistinguishable at the resolution obtained (Fig. 3.9A, B). Certainly, it was clear that DMT assembly appeared normal despite the loss of both CFAP77 genes in *Tetrahymena*. My results infer that CFAP77 is not needed for assembly of the DMT, perhaps, due to genetic redundancy. However, if there were irregular defects in the axoneme as a result of the CFAP77 double knockout, subtomogram averaging might have concealed them.

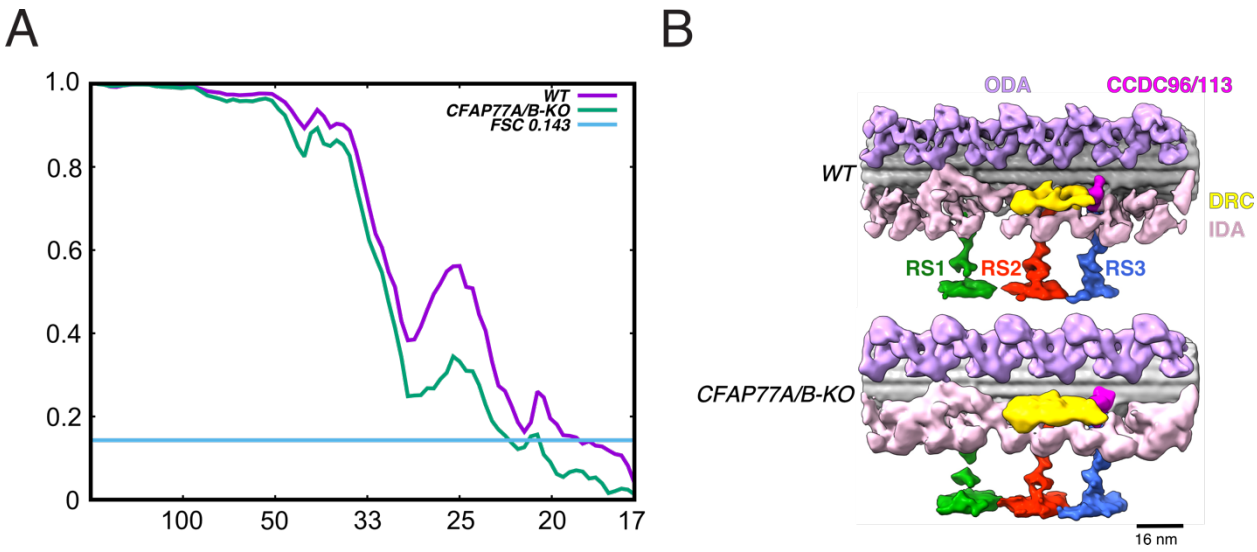

Figure 3.9. Cilia in the CFAP77A/B-KO mutant have a slightly higher level of tubulin glutamylation. (A) Fourier shell correlation curves showing the determined resolution of WT (CU-428) and CFAP77A/B-KO 96-nm subtomogram averaged maps. **(B)** The 96-nm subtomogram averaged maps of WT (CU-428) and CFAP77A/B-KO mice show no abnormalities. Adapted from Kubo *et al*., 2023.[142]

After seeing that the subtomogram-averaged maps for *CFAP77A/B-KO* and wild-type DMTs looked identical, I inspected every reconstructed tilt series. Interestingly, I observed two phenomena specific to *CFAP77A/B-KO* axonemes: infrequent gaps in the OJ of DMTs (Fig. 3.10A, B, blue arrows) and additional densities present at the OJ of DMTs

(Fig. 3.10A, B, red arrows). Perhaps the absence of CFAP77 destabilizes the OJ, causing it to undergo infrequent breakages from mechanical stresses associated with ciliary beating. The additional densities present at the OJ of *CFAP77A/B-KO* axonemes are unknown. It is possible that there is a compensatory mechanism involving one or more proteins binding to the OJ to stabilize it. It is also possible that these additional densities are proteins that are localized to the OJ of *CFAP77A/B-KO* axonemes to block unspecific or improperly localized proteins.[257] After structurally investigating the consequences of CFAP77 knockout in *Tetrahymena*, it was clear that there were subtle and observable defects. After I observed additional densities at the OJ, I was curious about how they were recruited. PTMs of β- and α-tubulin C-terminal tails are abundant and some of those are associated with recruitment and regulation of various MAPs and motor proteins.[72,258,259] Polyglutamylation of tubulin C-terminal tails has been shown to regulate the stability of MTs against the MT-severing enzyme spastin.[260] I wanted to wrap up my study of *CFAP77A/B-KO* axonemes by investigating tubulin polyglutamylation in *Tetrahymena* cilia in response to loss of CFAP77.

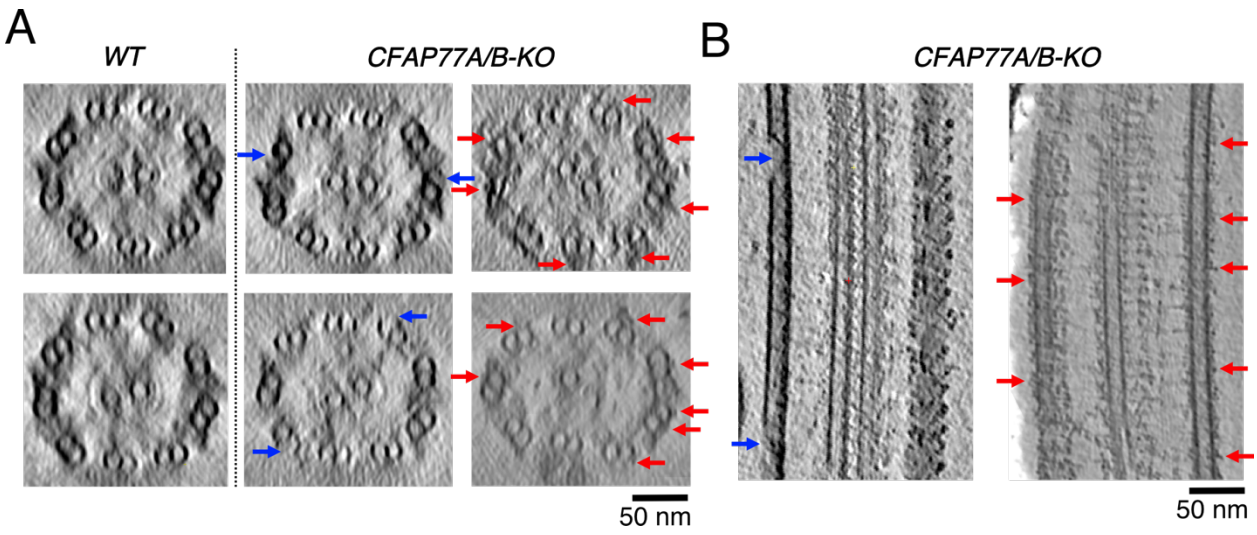

Figure 3.10. Knockout of CFAP77A/B caused mild defects in cilia.
(A) Tomographic cross-sections of WT and CFAP77A/B-KO mutants showing occasional damage in the OJ of CFAP77A/B-KO mutants (blue arrows) and unknown densities near the OJ (red arrows). **(B)** Longitudinal sections from the CFAP77A/B-KO tomogram showing OJ damage (blue arrows) and unknown densities (red arrows). Adapted from Kubo *et al.*, 2023.[142]

3.9.7 Knockout of CFAP77 *in Tetrahymena* is associated with higher tubulin polyglutamylation levels

I was curious after seeing the additional densities at the OJ of *CFAP77A/B-KO* axonemes and thought polyglutamylation might be responsible for that recruitment. Therefore, I wanted to compare tubulin polyglutamylation levels between *CFAP77A/B-KO* and wild-type cilia. To that end, Dr. Wloga's lab performed immunofluorescence microscopy localization experiments with polyE anti-polyglutamic acid primary antibodies to compare the fluorescence signal between *CFAP77A/B-KO* and wild-type cilia (Fig. 3.11A, B). Dr. Wloga's lab also performed western blotting and densiometric analyses of ciliary samples for both *CFAP77A/B-KO* and wild-type cilia (Fig. 3.11C, D). The tubulin polyglutamylation levels in *CFAP77A/B-KO* cilia were approximately twice (2X) as high as those in wild-type cilia (Fig. 3.11D). *Tetrahymena* cilia clearly have higher tubulin polyglutamylation levels in response to the loss of CFAP77. The binding affinity of mammalian MAP9 for MTs *in vitro* is dependent upon the level of polyglutamylation.[261] Perhaps increased polyglutamylation increases the affinity of *Tetrahymena* MAPs that bind and stabilize the DMT to compensate for the loss of CFAP77 and DMT instability. Importantly, the increase in polyglutamylation is not necessarily associated with recruitment of the densities seen in Figure 3.10B to the OJ. These experiments have raised interesting questions

concerning tubulin PTMs. How are ciliary tubulin PTMs related to MIP loss, general DMT instability, or extreme mechanical stresses? How do tubulin PTMs regulate all of the MAPs and MIPs in cilia? In this chapter, I leave the ciliary field with interesting observations concerning compensatory mechanisms in response to the loss of ciliary genes.

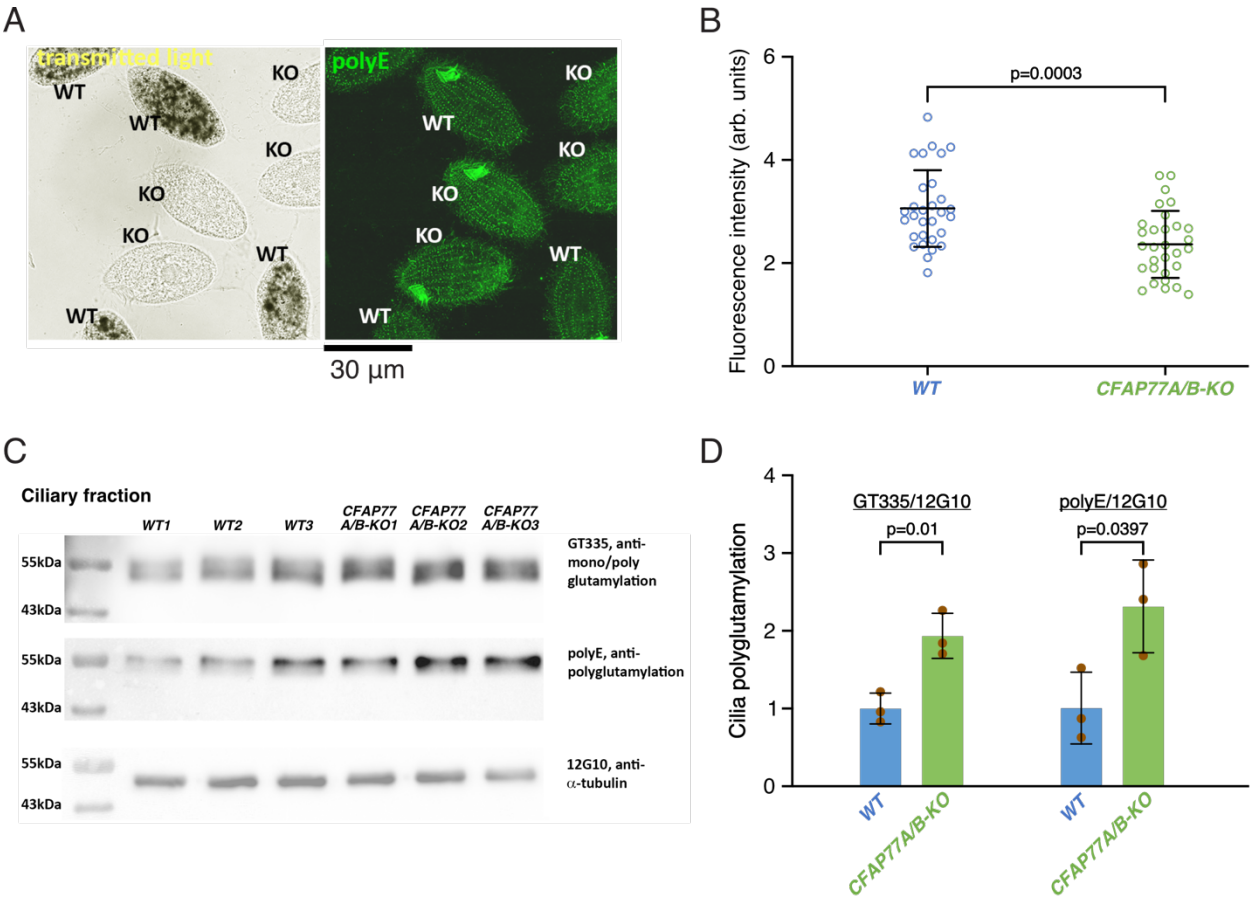

Figure 3.11. Cilia in the CFAP77A/B-KO mutant have a slightly higher level of tubulin glutamylation. (A) Phase-contrast (left) and immunofluorescence (right) of a mixed population of WT and CFAP77A/B-KO mutant cells stained with polyE antibodies detecting long glutamyl side chains (polyglutamylation). Note that WT cells were fed India ink and thus contained dark food vacuoles, enabling their identification in the population of mixed cells. **(B)** Graph showing the corresponding quantitative immunofluorescence analyses of the average pixel intensity of the axoneme region in mixed and processed

side–by–side populations of WT and mutant cells (n = 30 cells for each WT and CFAP77A/B-KO from one experiment). Fluorescence intensity is measured in arbitrary units. **(C)** Western blot and **(D)** densitometric analyses (graph) of the levels of tubulin glutamylation of ciliary tubulin in WT and CFAP77A/B-KO cells. The level of tubulin was determined using anti-α-tubulin 12G10 antibodies, and the levels of tubulin glutamylation were detected using GT335 (left) or polyE antibodies (right) (n = 3 biological replicates for WT and CFAP77A/B-KO). Data are presented as the mean values +/- standard deviations in (B and D). This experiment was performed one time. A two-sided t-test was performed for (B and D). Adapted from Kubo *et al.*, 2023.[142]

In this chapter, I collaborated with postdoctoral fellows Dr. Shintaroh Kubo and Dr. Dorota Wloga's lab at the Nencki Institute of Experimental Biology. I used cryo-EM and mass spectrometry to identify the OJ MIPs CFAP77A and OJ2 in *Tetrahymena* ciliary axonemes. I observed structural interactions that suggested that CFAP77A and OJ2 might stabilize the OJ of DMTs through their interactions with β-tubulin taxane-binding sites, β-tubulin C-terminal tails, and the α-tubulin lateral interface between PFs B1 and A11 (Fig. 3.2A, B). Using molecular dynamics simulations, we showed that CFAP77A and OJ2 stabilize the OJ of the DMT (Fig. 3.6A). Knockout of CFAP77 in *Tetrahymena* resulted in slower ciliary beating, slower swimming, and 10% shorter cilia length (Fig. 3.8A, B, D). I found that loss of CFAP77 in *Tetrahymena* was associated with a two-times increase in tubulin polyglutamylation (Fig. 3.11D). Using cryo-ET and subtomogram averaging, I compared the axonemes and 96-nm DMTs of *CFAP77A/B-KO* and wild-type cilia. While the subtomogram averaged map was not different in the double knockout, I found infrequent damage to the OJ of the DMT and additional densities present at the OJ (Fig. 3.10B). I took those findings and created a model to explain the role of CFAP77 in cilia (Fig. 3.12).

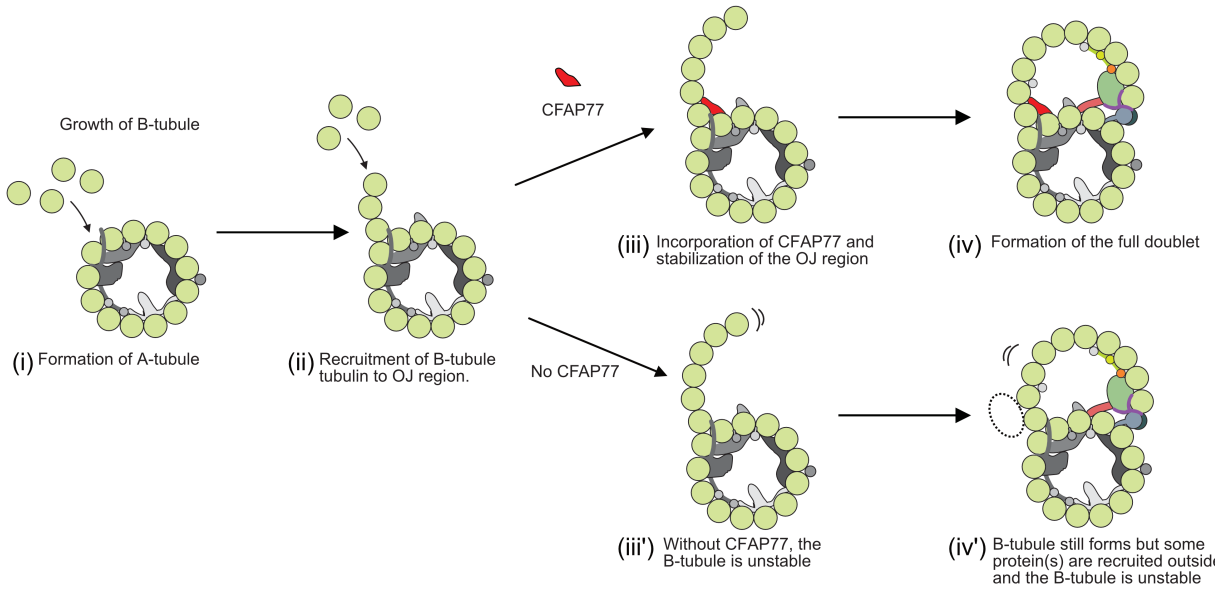

Figure 3.12. A model of the role of CFAP77 in the formation of B-tubules. The A-tubule is formed (i), and then free tubulins bind to form the hook at the OJ (ii). With CFAP77, the newly formed B-tubule hook is stabilized (iii), leading to the final DMT formation (iv). Without CFAP77, the B-tubule is not properly stabilized (iii'), and there are additional protein(s) on the outer surface (iv'). The presence of additional protein(s) may or may not be related to elevated levels of tubulin polyglutamylation detected in CFAP77A/B-KO cilia. Adapted from Kubo *et al.*, 2023.[142]

In wild-type cells, CFAP77 is recruited to the OJ of the forming DMT. Assembly of the DMT is not dependent on CFAP77. The lumen of the OJ of the DMT is occupied by CFAP77. Consequently, the DMT is stable. However, if CFAP77 is down-regulated or knocked out, the DMT is formed, but the OJ is somewhat destabilized, and additional protein(s) are recruited to the surface of the OJ. One idea is that ciliary beating puts excessive mechanical stresses on the DMT that lacks CFAP77, and consequently, the OJ is infrequently damaged. Recruitment of protein(s) to the OJ in response to the loss of CFAP77 is not understood. Perhaps recruitment of the unknown protein(s) is associated with higher levels of polyglutamylation of the C-terminal tail of β- and α-tubulin.

As this chapter concludes, I have accomplished the second research objective. In my introduction, I had three research goals:

I Obtain a high resolution cryo-EM map of the doublet microtubule from axonemes of *Tetrahymena* cilia.

II Model the molecular architecture of the *Tetrahymena* DMT, compare the *Tetrahymena* DMT with DMTs from other species, and identify proteins at the outer junction region of the DMT.

III Study one or two outer junction MIPs to understand their function in cilia.

The first two objectives were met after the herculean effort to model the near-complete architecture of the 48-nm native DMT from *Tetrahymena*. The third objective was completed after I performed structural analysis of the OJ MIPs CFAP77A and OJ2 and then collaborated with postdoctoral fellows Dr. Shintaroh Kubo and Dr. Dorota Wloga's laboratory to perform molecular dynamics simulations and genetic knockout experiments.

Chapter 4: General discussion and conclusion

4.1 Axonemal *Tetrahymena* DMT and MIPs

I isolated native DMTs by isolating cilia, solubilizing the ciliary membrane, and splitting the axoneme into intact MT-protein complexes by activating inner and outer dynein motor proteins (Fig. 2.1). I then used cryo-EM, mass spectrometry, and artificial intelligence to define the near-complete molecular architecture of the 48-nm repeating unit of the native axonemal DMT of *Tetrahymena* cilia. We modeled and identified 28 evolutionarily conserved MIPs and 13 MIPs only present in parasitic ciliates (Fig. 2.4, Table 2.3, and Table 2.4). I also observed densities for 8 MAPs bound to the surface of the A- and B-tubules on the outer-facing side of the DMT (Fig. 2.7).

The greatest evolutionary diversity in MIPs was observed at the ribbon PF arc region (Fig. 2.5B). Studying the relative stability of the DMT across species and their unique environments would provide insight into species-specific ciliary evolution. Molecular dynamics simulations would be a useful computational method to compare the energetic contributions of the *Chlamydomonas*- and *Tetrahymena*-specific CFAP and RIB proteins against the mammalian tektin bundle (Fig. 2.5B). An experimental approach could involve isolating each of the species DMTs and treating them with sarkosyl (sodium lauroyl sarcosinate) to dissociate the DMT into ribbons.[262] The relative stability between ribbons could then be measured with optical tweezers.[263]

4.2 *Tetrahymena* DMT MIPs and MAPs have a 96-nm registry

The periodicity of MIPs from DMTs isolated from *Chlamydomonas* flagella and mammalian cilia and sperm is reported to be 48 nm.[16,19,20] *Tetrahymena* MIPs have a 96-

nm registry (Fig. 2.6). It has long been established that the DMT surface exhibits a 96-nm registry, set by the evolutionarily conserved CCDC39/40 molecular ruler.[136] Periodicities of the inner and outer proteins in *Tetrahymena* are both 96 nm, while *Chlamydomonas* and mammals maintain disparate registries. Thus, the periodicities of inner and outer proteins of the ciliary DMTs are likely uncoupled. The organization of the CCDC39/40 complex is self-regulated by head-to-tail interactions[16,17,136]; perhaps the *Tetrahymena* ciliary MAPs are similarly self-regulated. Another explanation for the registries of MIPs and MAPs along the axonemal DMT is that they are set during the assembly of the basal body triplet MTs or base of the DMTs and propagate along the length of the cilia/flagella.

4.3 *Tetrahymena* DMT is decorated with PG-rich motif proteins

In the *Tetrahymena* ciliary proteome, there are at least 5 proteins containing PG-rich motifs: 3 sperm tail proline- and glycine-rich repeat proteins, STPG1A, STPG1B, and STPG2 and 2 Outer Dense Fiber 3-Like (ODF3L-1 and ODF3L-2) proteins (Fig. 2.9E). The PG-rich motif is a novel MT binding motif (Fig. 2.7E and Fig. 2.9E). I only observed cryo-EM densities for STPG1A and STPG2 (Fig. 2.7C, D). STPG1A and STPG2 each occupy a wedge of the B- and A-tubules, respectively, while short regions of both proteins extend into the lumen (Fig. 2.7). Insight from structural analyses of the DMT surface, combined with *in situ* mass spectrometry data, suggests that ODF3L-1 and ODF3L-2 proteins span 96 nm along the DMT surface (Kubo *et al*., 2023). The functions of the ODF3L-1 and ODF3L-2 proteins, as well as their possible involvement with the 96-nm registry of the *Tetrahymena* axonemal DMT, remain to be explored.

STPG1A and STPG2 are not the only proteins to thread between the MT surface and lumen. Evolutionarily conserved CFAP182A (Pierce1) and CFAP182B (Pierce2) weave along PFs A7-A8 of the A-tubule, occupying equal regions of the outer surface and lumen (Fig. 2.2 and Fig. 2.5B). Pierce1 and Pierce2 are important for outer dynein motor arm assembly in mammals and zebrafish and are thought to bridge the 24-nm outer dynein arm periodicity with the 48-nm mammalian MIP periodicity.[19] It would be interesting to build a model of the 48-nm *Tetrahymena* DMT including the outer dynein arms using data from this and a previous Bui lab publication[179] and use molecular dynamics simulations to predict the energetic contribution of CFAP182 to outer dynein arm stability. It would also be interesting to study the function of CFAP182A and CFAP182B in *Tetrahymena* through genetic knockout experiments and cryogenic electron tomography.

4.4 Tetrahymena MAPs overlap with tracks for IFT motor proteins

Tetrahymena MAPs bound to the outer-facing side of the A- and B-tubules overlap with retrograde and anterograde tracks, respectively (Fig. 2.7 and Fig. 2.8).[75] *Tetrahymena* MAPs may function similarly to MAP7. MAP7 was shown to exert biphasic regulation of kinesin-1 activity.[223] At low concentrations, the MAP7 projection domain recruits Kinesin-1 to MTs and activates Kinesin-1 motility.[223] At high concentrations, MAP7 slows and pauses anterograde transport at brunch junctions in rat neurons.[223,264] Perhaps the biphasic regulation is from the competition for MT binding sites between the MT binding domains of MAP7 and Kinesin-1 that result in steric clashes.[223] *Tetrahymena* MAPs may similarly regulate IFT through competition for MT binding sites (Fig. 2.9A-D). When we docked kinesin-2 to the B-tubule (anterograde track) and dynein-2 to the A-tubule

(retrograde track), I observed steric clashes with filamentous MAPs (Fig. 2.9A-D). Densities for filamentous MAPs in the outer-facing A- and B-tubules have not been observed in cryo-EM maps from *Chlamydomonas* or mammalian DMTs.[16,19,20] It could be that the filamentous MAPs are a species-specific adaptation, or it could be that those MAPs were lost during sample preparation. In *Chlamydomonas* flagella, Dr. Ben Engel's lab showed that axonemal DMTs proximal to the basal body have a sleeve that completely envelops their surfaces for 76 nm (Fig. 1.2D).[66] This sleeve could act as a barrier for IFT trains.[66] We have not observed a similar structure in *Tetrahymena*.[142,151] The evolutionary conservation of IFT is particularly interesting when it appears that many organisms have different mechanisms of regulation. Understanding and comparing those regulatory mechanisms not only informs us about evolutionary biology but might later provide an exploitation for biotechnology and MT-based delivery systems.

4.5 CFAP77 and OJ2 stabilize the outer junction of DMTs in *Tetrahymena*

Bioinformatics revealed that OJ2 is a ciliary protein within parasitic ciliates, while CFAP77 is evolutionarily conserved within motile cilia and flagella. There is no evidence for CFAP77 in primary cilia. Expression of CFAP77 in human airway epithelial cell culture starts during differentiation, when ciliated cells become plentiful.[265] CFAP77 localizes along the entire length of human airway epithelial cilia but is most abundant in the middle (axonemal) region.[265] In a genome-wide study of epigenetic markers of opioid dependence in European-American women, CFAP77 was one of three genes with CpG sites that were hypomethylated.[266] A proteomics study of epididymal buffalo sperm showed that CFAP77 was one of 84 proteins that were both phosphorylated and

ubiquitinated.[267] These studies show that CFAP77 gene expression is regulated by methylation and that CFAP77 protein activity is regulated by phosphorylation and ubiquitination.[266,267] I did not study how up-regulation of CFAP77 gene expression affects cilia in *Tetrahymena*, as hypomethylation would do in human airway epithelial cilia.[265] Studying CFAP77 over-expression might shed some light on the association with opioid use disorder.[266] It is unknown how phosphorylation and ubiquitination of CFAP77 alter its activity, cilia, or the DMT. Once the ciliary and structural effects of CFAP77 phosphorylation and ubiquitination are known, another interesting study would be to detect the temporal dynamics of CFAP77 PTMs during sperm maturation and swimming. This would serve as a model for MIP PTMs in cilia and flagella. Dysregulation of CFAP77 gene expression and protein activity is not associated with severe diseases, which suggests that CFAP77 has a redundant role in cilia.

Structural analyses of CFAP77A and OJ2 revealed much evidence for their role in the stabilization of the OJ of DMTs. Both proteins weave along the lumen of the OJ, interacting with many PFs and binding to β-tubulin taxane-binding sites (Fig. 3.2). OJ2 might stabilize the lateral interaction between α-tubulins from PFs B1 and A11 of the OJ (Fig. 3.5B). CFAP77A and OJ2 are both incredibly electrostatically attracted and proximal to the β-tubulin C-terminal tails of the A-tubule (Fig. 3.3). Cleavage of tubulin C-terminal tails of singlet MTs is necessary for partial DMT assembly *in vitro* in the absence of any MT-interacting protein.[74] However, any perturbation of β-tubulin C-terminal tails *in vivo* is deleterious to ciliary function in mammals.[152,228] It would follow that one or more proteins function to suppress tubulin C-terminal tails during OJ assembly.

Functional studies further supported the stabilizing roles of CFAP77 and OJ2 in the axonemal DMT. Molecular dynamics simulations predicted that both CFAP77A and OJ2 stabilize the OJ of the DMT (Fig. 3.6). *Tetrahymena* has two paralogs of CFAP77 that differentially localize, and knockout of both paralogs resulted in slightly shorter cilia with a reduced beat frequency and reduced swimming speed (Fig. 3.8). The shorter cilia length implied an assembly defect, but not in the proteins composing the 96-nm as shown the reconstructed tomograms (Fig. 3.10). However, I did observe infrequent damage to the OJ and additional densities. The damage is likely caused by the loss of CFAP77 during ciliary beating, while the identity of the additional densities remains unknown. Perhaps unknown compensative proteins bind to the OJ to stabilize it (Fig. 3.10). Alternatively, the additional densities at the OJ may be regulatory proteins that block mis-localized proteins.[257] The reduced ciliary beating and swimming speed of *CFAP77A/B-KO* is similar to the phenotypes of *RIB72A/B-KO* and *CFAP115-KO*. *RIB72A/B-KO*[144] and *CFAP115-KO*[143] are both associated with reduced ciliary beating frequency and slower swimming. There is also impaired coordination of ciliary action in *RIB72A/B-KO*,[144] *CFAP115-KO*,[143] and *CFAP77A/B-KO*,[142] which causes occasional excessive curves in the waveform (Fig. 3.8).

4.6 CFAP77 is not essential for DMT assembly or swimming in *Tetrahymena*

MAP9 was recently shown to be important for stabilization of the OJ.[261] Loss of MAPH-9 resulted in ultrastructural defects in axonemes of *Caenorhabditis elegans* ciliated sensory neurons.[261] While the axonemes in wild-type and MAPH-9 knockout cells were observed to have a mix of DMTs, partial DMTs, and singlet MTs, there were more singlet MTs

observed in MAPH-9 knockout cells.[261] The rest of the investigation of that study, as well as the results from this thesis, support stabilizing roles for CFAP77A and MAPH-9 at the OJ of the DMTs, but neither protein is required for DMT formation or ciliary function.[142,261] Furthermore, the filamentous proteins on the surface of the *Tetrahymena* DMT likely stabilize the OJ in the same way MAPH-9 does in *Caenorhabditis elegans* neurons.[142,261] It may be that these MAPs are also sufficient for stabilization of DMTs from primary cilia that lack CFAP77.

Dr. Hiroshi Inaba and colleagues designed a tetrameric peptide; each monomer consists of a single repeat of the tau MT binding domain fused to both an Azami-Green fluorescent protein and a polyhistidine tag.[268] When this tetrameric peptide was co-polymerized with free tubulin under various conditions, it nucleated various MT superstructures *in vitro,* including branched MTs and partial DMTs.[268] Perhaps unidentified MAPs or MIPs function similarly to that tetrameric peptide and are necessary for assembly of the OJ of DMTs. For example, the unidentified filamentous density OJ3 (Fig. 3.1). This protein could function in assembly of the OJ in both motile and primary cilia that lack CFAP77.

My investigation into CFAP77 has shown that it stabilizes the DMTs that are under bending, compressive and tensile mechanical stresses.[269] It is generally accepted that MIPs act to regulate DMT stability and isolate damage or defects caused by ciliary bending.[139] The loss of a MIP could mean that bending-induced damage is sustained more often than in cilia with the MIP present. Ciliary bending and mechanical force are strongest at the base.[270] The CFAP77A paralog was expressed at higher levels than the CFAP77B paralog in Tetrahymena, and CFAP77A was localized to the lower region of

the axoneme (Fig. 3.7). Perhaps the OJ of the DMT is more stable where CFAP77A is more abundant.

Obviously, OJ2 contributes to the stability of the DMT in *Tetrahymena,* as evidenced by structural interactions and simulations. The triple knockout of CFAP77A, CFAP77B, and OJ2 would be expected to have more dramatic effects on the stability and assembly of the DMT. Furthermore, the triple knockout would be closer to the effects of the loss of CFAP77 in mammals (including humans) because OJ2 is species specific. Filamentous MAPs along the outer surface PFs may be sufficient to prevent catastrophic failure, but significant damage would be expected. Loss of CFAP77 may be more consequential to airway epithelial cilia and sperm in mammals because there are no other MIPs that have been observed between PFs B1 and A11.[20] Perhaps there is a ciliopathy associated with loss of CFAP77, just as hypomethylation of the CFAP77 gene is associated with opioid dependency.[265]

4.7 A tubulin PTM code regulates DMT stability and interacting proteins in cilia

Tubulin PTMs have previously been proposed to act as a "code" that is read out by motor proteins for directional regulation.[271] Tubulin polyglutamylation increases the affinity of Tau for MTs and the MT-severing activity of katanin; however, β-tubulin polyglutamylation decreases kinesin-1 processivity.[272] Molecular dynamics simulations have shown that polyglutamylation is inhibitory to dynein activity and may act as boundaries for dynein motor tracks.[273] Mammalian MAP9 specifically binds to polyglutamylated MTs *in vitro*.[261] In *CFAP77A/B-KO* cilia, tubulin polyglutamylation levels were twice as high as those in

wild-type cilia (Fig. 3.11). Perhaps tubulin PTMs are part of a compensatory mechanism in response to instability associated with MIP loss.

4.8 Conclusion

I have made many contributions toward our understanding of cilia and MIPs. I have optimized methods for culturing *Tetrahymena* strains; intact axoneme purification; intact DMT purification; and cryo-EM/cryo-ET sample preparation. I set out with three research objectives: i) Obtain a high resolution cryo-EM map of the doublet microtubule from axonemes of *Tetrahymena* cilia; Model the molecular architecture of the *Tetrahymena* DMT, compare the *Tetrahymena* DMT with DMTs from other species, and identify proteins at the outer junction region of the DMT; and iii) Study one or two outer junction MIPs to understand their function in cilia.

I have shown that the 48-nm repeat of the native *Tetrahymena* DMT contains at least 28 evolutionarily conserved MIPs, 13 MIPs unique to parasitic ciliates, and filamentous MAPs on the outer surface. I found a structural basis for MIPs CFAP77 and OJ2 stabilizing the OJ of DMT. Using molecular dynamics simulations, we showed that CFAP77A and OJ2 energetically stabilize the OJ. Using gene knockout, we showed that loss of CFAP77A and CFAP77B caused minor infrequent damage to the DMT OJ, shorter cilia, and slower swimming. I have demonstrated that CFAP77 is an evolutionarily conserved MIP that stabilizes the OJ of the axonemal DMT but is not necessary for assembly or motility.

As important as the contributions toward knowledge, I also leave the field of cilia and flagella with many intriguing questions. I have shown that OJ2 may be important for the

assembly and stability of axonemal DMTs in parasitic ciliates. Further investigation is required to find the answer; in doing so, the investigator will also understand the consequence of CFAP77 loss in mammals because CFAP77 is the only luminal OJ MIP in motile cilia. Another protein that may also be important for the OJ is CFAP141, a short helical protein wedged between PFs B1 and A11 (Fig. 2.4). CFAP141 is evolutionarily conserved and was modelled in DMTs from flagella from algae[16] and mammalian sperm.[274] I also demonstrated that the compensatory response to MIP loss and DMT instability is recruitment of proteins and increased tubulin polyglutamylation. How do tubulin PTMs affect DMT stability and the molecular architecture of the MIP network? While it was known that tubulin PTMs are part of the tubulin code for MAPs and motor proteins, we now know MIPs are involved as well. There is an intricate network connecting tubulin PTMs to the constitution of the axonemal DMT. Discovering how PTMs affect the DMT will provide a much greater understanding of ciliary regulation.

References

1 Mitchell, D. R. Evolution of Cilia. *Cold Spring Harbor Perspectives in Biology* **9**, a028290 (2017). https://doi.org/10.1101/cshperspect.a028290

2 Satir, P. Cilia. *Scientific American* **204**, 108-116 (1961). https://doi.org/10.1038/scientificamerican0261-108

3 Satir, P. & Christensen, S. T. Overview of Structure and Function of Mammalian Cilia. *Annual Review of Physiology* **69**, 377-400 (2007). https://doi.org/10.1146/annurev.physiol.69.040705.141236

4 Youn, Y. H. & Han, Y.-G. Primary Cilia in Brain Development and Diseases. *The American Journal of Pathology* **188**, 11-22 (2018). https://doi.org/10.1016/j.ajpath.2017.08.031

5 Pazour, G. J., Agrin, N., Leszyk, J. & Witman, G. B. Proteomic analysis of a eukaryotic cilium. *Journal of Cell Biology* **170**, 103-113 (2005). https://doi.org/10.1083/jcb.200504008

6 Nicastro, D. *et al.* Cryo-electron tomography reveals conserved features of doublet microtubules in flagella. *Proceedings of the National Academy of Sciences* **108** (2011). https://doi.org/10.1073/pnas.1106178108

7 Sui, H. & Downing, K. H. Molecular architecture of axonemal microtubule doublets revealed by cryo-electron tomography. *Nature* **442**, 475-478 (2006). https://doi.org/10.1038/nature04816

8 Ichikawa, M., Liu, D., Kastritis, P. L., Basu, K., Hsu, T. C., Yang, S., & Bui, K. H. Subnanometre-resolution structure of the doublet microtubule reveals new classes of microtubule-associated proteins. *Nat Commun* **8**, 15035 (2017).

9 Nakane, T. *et al.* Single-particle cryo-EM at atomic resolution. *Nature* **587**, 152-156 (2020). https://doi.org/10.1038/s41586-020-2829-0

10 Yip, K. M., Fischer, N., Paknia, E., Chari, A. & Stark, H. Atomic-resolution protein structure determination by cryo-EM. *Nature* **587**, 157-161 (2020). https://doi.org/10.1038/s41586-020-2833-4

11 Fujiyoshi, Y. The structural study of membrane proteins by electron crystallography. *Advances in Biophysics* **35**, 25-80 (1998). https://doi.org/10.1016/S0065-227X(98)80003-8

12 Allegretti, M. *et al.* In-cell architecture of the nuclear pore and snapshots of its turnover. *Nature* **586**, 796-800 (2020). https://doi.org/10.1038/s41586-020-2670-5

13 Frank, J., Verschoor, A. & Boublik, M. Computer Averaging of Electron Micrographs of 40S Ribosomal Subunits. *Science* **214**, 1353-1355 (1981). https://doi.org/doi:10.1126/science.7313694

14 Gabashvili, I. S. *et al.* Solution Structure of the E. coli 70S Ribosome at 11.5 ŠResolution. *Cell* **100**, 537-549 (2000). https://doi.org/10.1016/S0092-8674(00)80690-X

15 Nguyen, T. H. D. *et al.* The architecture of the spliceosomal U4/U6.U5 tri-snRNP. *Nature* **523**, 47-52 (2015). https://doi.org/10.1038/nature14548

16 Ma, M. *et al.* Structure of the Decorated Ciliary Doublet Microtubule. *Cell* **179**, 909-922 e912 (2019). https://doi.org/10.1016/j.cell.2019.09.030

17 Ichikawa, M. *et al.* Tubulin lattice in cilia is in a stressed form regulated by microtubule inner proteins. *Proceedings of the National Academy of Sciences* **116**, 19930-19938 (2019). https://doi.org/10.1073/pnas.1911119116
18 Khalifa, A. A. Z. *et al.* The inner junction complex of the cilia is an interaction hub that involves tubulin post-translational modifications. *eLife* **9**, e52760 (2020). https://doi.org/10.7554/eLife.52760
19 Gui, M. *et al.* De novo identification of mammalian ciliary motility proteins using cryo-EM. *Cell* **184**, 5791-5806.e5719 (2021). https://doi.org/https://doi.org/10.1016/j.cell.2021.10.007
20 Leung, M. R. *et al.* Unraveling the intricate microtubule inner protein networks that reinforce mammalian sperm flagella. (Cell Biology, 2022).
21 Dippell, R. V. The development of basal bodies in paramecium. *Proceedings of the National Academy of Sciences* **61**, 461-468 (1968). https://doi.org/10.1073/pnas.61.2.461
22 Ruehle, M. D., Orias, E. & Pearson, C. G. Tetrahymena as a Unicellular Model Eukaryote: Genetic and Genomic Tools. *Genetics* **203**, 649-665 (2016). https://doi.org/10.1534/genetics.114.169748
23 Orias, E., Cervantes, M. D. & Hamilton, E. P. Tetrahymena thermophila, a unicellular eukaryote with separate germline and somatic genomes. *Research in Microbiology* **162**, 578-586 (2011). https://doi.org/10.1016/j.resmic.2011.05.001
24 Eisen, J. A. *et al.* Macronuclear Genome Sequence of the Ciliate Tetrahymena thermophila, a Model Eukaryote. *PLoS Biology* **4**, e286 (2006). https://doi.org/10.1371/journal.pbio.0040286
25 Nevers, Y. *et al.* Insights into Ciliary Genes and Evolution from Multi-Level Phylogenetic Profiling. *Molecular Biology and Evolution* **34**, 2016-2034 (2017). https://doi.org/10.1093/molbev/msx146
26 Brumley, D. R., Polin, M., Pedley, T. J. & Goldstein, R. E. Metachronal waves in the flagellar beating of Volvox and their hydrodynamic origin. *Journal of The Royal Society Interface* **12**, 20141358 (2015). https://doi.org/10.1098/rsif.2014.1358
27 Satir, P. ON THE EVOLUTIONARY STABILITY OF THE 9 + 2 PATTERN. *Journal of Cell Biology* **12**, 181-184 (1962). https://doi.org/10.1083/jcb.12.1.181
28 Lindemann, C. B. & Lesich, K. A. The many modes of flagellar and ciliary beating: Insights from a physical analysis. *Cytoskeleton* **78**, 36-51 (2021). https://doi.org/10.1002/cm.21656
29 Wong, S. Y. & Reiter, J. F. in *Current Topics in Developmental Biology* Vol. 85 225-260 (Elsevier, 2008).
30 Wong, S. Y. *et al.* Primary cilia can both mediate and suppress Hedgehog pathway–dependent tumorigenesis. *Nature Medicine* **15**, 1055-1061 (2009). https://doi.org/10.1038/nm.2011
31 Nonaka, S. *et al.* Randomization of Left–Right Asymmetry due to Loss of Nodal Cilia Generating Leftward Flow of Extraembryonic Fluid in Mice Lacking KIF3B Motor Protein. *Cell* **95**, 829-837 (1998). https://doi.org/10.1016/S0092-8674(00)81705-5
32 Hamada, H., Meno, C., Watanabe, D. & Saijoh, Y. Establishment of vertebrate left–right asymmetry. *Nature Reviews Genetics* **3**, 103-113 (2002). https://doi.org/10.1038/nrg732

33 Worthington, W. C. & Cathcart, R. S. Ependymal Cilia: Distribution and Activity in the Adult Human Brain. *Science* **139**, 221-222 (1963). https://doi.org/10.1126/science.139.3551.221

34 Olstad, E. W. *et al.* Ciliary Beating Compartmentalizes Cerebrospinal Fluid Flow in the Brain and Regulates Ventricular Development. *Current Biology* **29**, 229-241.e226 (2019). https://doi.org/10.1016/j.cub.2018.11.059

35 Kramer-Zucker, A. G. *et al.* Cilia-driven fluid flow in the zebrafish pronephros, brain and Kupffer's vesicle is required for normal organogenesis. *Development* **132**, 1907-1921 (2005). https://doi.org/10.1242/dev.01772

36 Sakka, L., Coll, G. & Chazal, J. Anatomy and physiology of cerebrospinal fluid. *European Annals of Otorhinolaryngology, Head and Neck Diseases* **128**, 309-316 (2011). https://doi.org/10.1016/j.anorl.2011.03.002

37 Zhu, M. *et al.* Human Cerebrospinal Fluid Regulates Proliferation and Migration of Stem Cells Through Insulin-Like Growth Factor-1. *Stem Cells and Development* **24**, 160-171 (2015). https://doi.org/10.1089/scd.2014.0076

38 Fame, R. M. & Lehtinen, M. K. Emergence and Developmental Roles of the Cerebrospinal Fluid System. *Developmental Cell* **52**, 261-275 (2020). https://doi.org/10.1016/j.devcel.2020.01.027

39 Sade, J. Ciliary Activity and Middle Ear Clearance. *Archives of Otolaryngology - Head and Neck Surgery* **86**, 128-135 (1967). https://doi.org/10.1001/archotol.1967.00760050130002

40 Sade, J., Meyer, F. A., King, M. & Silberberg, A. Clearance of Middle Ear Effusions by the Mucociliary System. *Acta Oto-Laryngologica* **79**, 277-282 (1975). https://doi.org/10.3109/00016487509124685

41 Matsui, H., Randell, S. H., Peretti, S. W., Davis, C. W. & Boucher, R. C. Coordinated clearance of periciliary liquid and mucus from airway surfaces. *Journal of Clinical Investigation* **102**, 1125-1131 (1998). https://doi.org/10.1172/JCI2687

42 Battista, S. P. & Kensler, C. J. Mucus Production and Ciliary Transport Activity In Vivo Studies Using the Chicken. *Archives of Environmental Health: An International Journal* **20**, 326-338 (1970). https://doi.org/10.1080/00039896.1970.10665600

43 Hartman, C. G. in *Sex and internal secretions: A survey of recent research.* (ed Edgar Allen) 647-733 (Williams & Wilkins Co, 1934).

44 Grochowsky, A. & Gunay-Aygun, M. Clinical characteristics of individual organ system disease in non-motile ciliopathies. *Translational Science of Rare Diseases* **4**, 1-23 (2019). https://doi.org/10.3233/TRD-190033

45 Yamaguchi, T., Hempson, S. J., Reif, G. A., Hedge, A.-M. & Wallace, D. P. Calcium Restores a Normal Proliferation Phenotype in Human Polycystic Kidney Disease Epithelial Cells. *Journal of the American Society of Nephrology* **17**, 178-187 (2006). https://doi.org/10.1681/ASN.2005060645

46 McMahon, A. P., Ingham, P. W. & Tabin, C. J. in *Current Topics in Developmental Biology* Vol. 53 1-114 (Elsevier, 2003).

47 Mitchison, H. M. & Valente, E. M. Motile and non-motile cilia in human pathology: from function to phenotypes: Motile and non-motile ciliopathies. *The Journal of Pathology* **241**, 294-309 (2017). https://doi.org/10.1002/path.4843

48 Meeks, M. & Bush, A. Primary ciliary dyskinesia (PCD). *Pediatric Pulmonology* **29**, 307-316 (2000). https://doi.org/10.1002/(SICI)1099-0496(200004)29:4<307::AID-PPUL11>3.0.CO;2-2

49 Antony, D. *et al.* Mutations in CCDC39 and CCDC40 are the Major Cause of Primary Ciliary Dyskinesia with Axonemal Disorganization and Absent Inner Dynein Arms. *Human Mutation* **34**, 462-472 (2013). https://doi.org/https://doi.org/10.1002/humu.22261

50 Nosrati, R., Driouchi, A., Yip, C. M. & Sinton, D. Two-dimensional slither swimming of sperm within a micrometre of a surface. *Nature Communications* **6**, 8703 (2015). https://doi.org/10.1038/ncomms9703

51 Yanagimachi, R. Mysteries and unsolved problems of mammalian fertilization and related topics. *Biology of Reproduction* **106**, 644-675 (2022). https://doi.org/10.1093/biolre/ioac037

52 Ganner, A. & Neumann-Haefelin, E. Genetic kidney diseases: Caenorhabditis elegans as model system. *Cell and Tissue Research* **369**, 105-118 (2017). https://doi.org/10.1007/s00441-017-2622-z

53 Werner, M. E. & Mitchell, B. J. in *Methods in Enzymology* Vol. 525 191-217 (Elsevier, 2013).

54 Pinto, A. L. *et al.* Zebrafish Motile Cilia as a Model for Primary Ciliary Dyskinesia. *International Journal of Molecular Sciences* **22**, 8361 (2021). https://doi.org/10.3390/ijms22168361

55 Rajagopalan, V. *et al.* in *Cytoskeleton Methods and Protocols* Vol. 586 (ed Ray H. Gavin) 283-299 (Humana Press, 2009).

56 Ray, C. Meiosis and Nuclear Behavior in Tetrahymena pyriformis *. *The Journal of Protozoology* **3**, 88-96 (1956). https://doi.org/10.1111/j.1550-7408.1956.tb02440.x

57 Karrer, K. M. in *Methods in Cell Biology* Vol. 62 127-186 (Elsevier, 1999).

58 Fujii, G., Tsuchiya, R., Ezoe, E. & Hirohashi, S. Analysis of Nuclear Localization Signals Using a Green Fluorescent Protein-Fusion Protein Library. *Experimental Cell Research* **251**, 299-306 (1999). https://doi.org/10.1006/excr.1999.4575

59 Dave, D., Wloga, D. & Gaertig, J. in *Methods in Cell Biology* Vol. 93 1-20 (Elsevier, 2009).

60 Howard-Till, R., Tian, M. & Loidl, J. A specialized condensin complex participates in somatic nuclear maturation in Tetrahymena thermophila. *Molecular Biology of the Cell* **30**, 1326-1338 (2019). https://doi.org/10.1091/mbc.E18-08-0487

61 Porter, K. R. The submicroscopic morphology of protoplasm. 1956. *The Anatomical Record. Part A, Discoveries in Molecular, Cellular, and Evolutionary Biology* **287**, 1186-1204 (2005).

62 Manton, I., Clarke, B., Greenwood, A. D. & Flint, E. A. Further Observations on the Structure of Plant Cilia, by a Combination of Visual and Electron Microscopy. *Journal of Experimental Botany* **3** (1952).

63 Anvarian, Z., Mykytyn, K., Mukhopadhyay, S., Pedersen, L. B. & Christensen, S. T. Cellular signalling by primary cilia in development, organ function and disease. *Nature Reviews Nephrology* **15**, 199-219 (2019). https://doi.org/10.1038/s41581-019-0116-9

64 Bae, Y.-K., Kim, E., L'Hernault, S. W. & Barr, M. M. The CIL-1 PI 5-Phosphatase Localizes TRP Polycystins to Cilia and Activates Sperm in C. elegans. *Current Biology* **19**, 1599-1607 (2009). https://doi.org/https://doi.org/10.1016/j.cub.2009.08.045

65 Chávez, M. *et al.* Modulation of Ciliary Phosphoinositide Content Regulates Trafficking and Sonic Hedgehog Signaling Output. *Developmental Cell* **34**, 338-350 (2015). https://doi.org/https://doi.org/10.1016/j.devcel.2015.06.016

66 van den Hoek, H. *et al.* In situ architecture of the ciliary base reveals the stepwise assembly of intraflagellar transport trains. *Science* **377**, 543-548 (2022). https://doi.org/10.1126/science.abm6704

67 Palmblad, J., Mossberg, B. & Afzelius, B. A. Ultrastructural, Cellular, and Clinical Features of the Immotile-Cilia Syndrome. *Annual Review of Medicine* **35**, 481-492 (1984). https://doi.org/10.1146/annurev.me.35.020184.002405

68 Song, K. *et al.* In situ structure determination at nanometer resolution using TYGRESS. *Nature Methods* **17**, 201-208 (2020). https://doi.org/10.1038/s41592-019-0651-0

69 Margolis, R. L., Wilson, L. & Kiefer, B. I. Mitotic mechanism based on intrinsic microtubule behaviour. *Nature* **272**, 450-452 (1978). https://doi.org/10.1038/272450a0

70 Rodionov, V. I. *et al.* Microtubule-dependent control of cell shape and pseudopodial activity is inhibited by the antibody to kinesin motor domain. *Journal of Cell Biology* **123**, 1811-1820 (1993). https://doi.org/10.1083/jcb.123.6.1811

71 Smith, D. S., Järlfors, U. & Beránek, R. THE ORGANIZATION OF SYNAPTIC AXOPLASM IN THE LAMPREY (PETROMYZON MARINUS) CENTRAL NERVOUS SYSTEM. *Journal of Cell Biology* **46**, 199-219 (1970). https://doi.org/10.1083/jcb.46.2.199

72 Westermann, S. & Weber, K. Post-translational modifications regulate microtubule function. *Nature Reviews Molecular Cell Biology* **4**, 938-948 (2003). https://doi.org/10.1038/nrm1260

73 Anderson, R. G. W. & Brenner, R. M. THE FORMATION OF BASAL BODIES (CENTRIOLES) IN THE RHESUS MONKEY OVIDUCT. *Journal of Cell Biology* **50**, 10-34 (1971). https://doi.org/10.1083/jcb.50.1.10

74 Schmidt-Cernohorska, M. Flagellar microtubule doublet assembly in vitro reveals a regulatory role of tubulin C-terminal tails. *Science* **363**, 285-288 (2019).

75 Stepanek, L. & Pigino, G. Microtubule doublets are double-track railways for intraflagellar transport trains. *Science* **352**, 721-724 (2016).

76 Satir, P. How cilia move. *Scientific American* **231**, 44-52 (1974). https://doi.org/10.1038/scientificamerican1074-44

77 Keeling, P. J. & Doolittle, W. F. Alpha-tubulin from early-diverging eukaryotic lineages and the evolution of the tubulin family. *Molecular Biology and Evolution* **13**, 1297-1305 (1996). https://doi.org/10.1093/oxfordjournals.molbev.a025576

78 Landrein, B. & Hamant, O. How mechanical stress controls microtubule behavior and morphogenesis in plants: history, experiments and revisited theories. *The Plant Journal* **75**, 324-338 (2013). https://doi.org/10.1111/tpj.12188

79 Nogales, E., Whittaker, M., Milligan, R. A. & Downing, K. H. High-resolution model of the microtubule. *Cell* **96**, 79-88 (1999).

80 Huang, A. B., Lin, C. M. & Hamel, E. Differential effects of magnesium on tubulin-nucleotide interactions. *Biochimica et Biophysica Acta (BBA) - Protein Structure and*

Molecular Enzymology **832**, 22-32 (1985). https://doi.org/10.1016/0167-4838(85)90170-0

81 Rice, L. M., Montabana, E. A. & Agard, D. A. The lattice as allosteric effector: Structural studies of αβ- and γ-tubulin clarify the role of GTP in microtubule assembly. *Proceedings of the National Academy of Sciences* **105**, 5378-5383 (2008). https://doi.org/10.1073/pnas.0801155105

82 Hyman, A. A., Salser, S., Drechsel, D. N., Unwin, N. & Mitchison, T. J. Role of GTP hydrolysis in microtubule dynamics: information from a slowly hydrolyzable analogue, GMPCPP. *Molecular Biology of the Cell* **3**, 1155-1167 (1992). https://doi.org/10.1091/mbc.3.10.1155

83 Eshun-Wilson, L. *et al.* Effects of α-tubulin acetylation on microtubule structure and stability. *Proceedings of the National Academy of Sciences* **116**, 10366-10371 (2019). https://doi.org/10.1073/pnas.1900441116

84 Ley, S. C. *et al.* Tyrosine phosphorylation of α tubulin in human T lymphocytes. *European Journal of Immunology* **24**, 99-106 (1994). https://doi.org/10.1002/eji.1830240116

85 Fourest-Lieuvin, A. *et al.* Microtubule Regulation in Mitosis: Tubulin Phosphorylation by the Cyclin-dependent Kinase Cdk1. *Molecular Biology of the Cell* **17**, 1041-1050 (2006). https://doi.org/10.1091/mbc.e05-07-0621

86 Khan, I. A. & Ludueña, R. F. Phosphorylation of β _{III} -Tubulin. *Biochemistry* **35**, 3704-3711 (1996). https://doi.org/10.1021/bi951247p

87 Song, Y. *et al.* Transglutaminase and Polyamination of Tubulin: Posttranslational Modification for Stabilizing Axonal Microtubules. *Neuron* **78**, 109-123 (2013). https://doi.org/10.1016/j.neuron.2013.01.036

88 Brady, S. T., Tytell, M. & Lasek, R. J. Axonal tubulin and axonal microtubules: biochemical evidence for cold stability. *Journal of Cell Biology* **99**, 1716-1724 (1984). https://doi.org/10.1083/jcb.99.5.1716

89 Hallak, M. E., Rodriguez, J. A., Barra, H. S. & Caputto, R. Release of tyrosine from tyrosinated tubulin. Some common factors that affect this process and the assembly of tubulin. *FEBS Letters* **73**, 147-150 (1977). https://doi.org/10.1016/0014-5793(77)80968-X

90 Gundersen, G. G., Khawaja, S. & Bulinski, J. C. Postpolymerization detyrosination of alpha-tubulin: a mechanism for subcellular differentiation of microtubules. *Journal of Cell Biology* **105**, 251-264 (1987). https://doi.org/10.1083/jcb.105.1.251

91 Brown, A., Li, Y., Slaughter, T. & Black, M. M. Composite microtubules of the axon: quantitative analysis of tyrosinated and acetylated tubulin along individual axonal microtubules. *Journal of Cell Science* **104**, 339-352 (1993). https://doi.org/10.1242/jcs.104.2.339

92 Multigner, L. *et al.* The A and B Tubules of the Outer Doublets of Sea Urchin Sperm Axonemes Are Composed of Different Tubulin Variants. *Biochemistry* **35**, 10862-10871 (1996). https://doi.org/10.1021/bi961057u

93 Webster, D. R. Detyrosination of alpha tubulin does not stabilize microtubules in vivo [published erratum appears in J Cell Biol 1990 Sep;111(3):1325-6]. *The Journal of Cell Biology* **111**, 113-122 (1990). https://doi.org/10.1083/jcb.111.1.113

94 Ghosh-Roy, A., Goncharov, A., Jin, Y. & Chisholm, Andrew D. Kinesin-13 and Tubulin Posttranslational Modifications Regulate Microtubule Growth in Axon Regeneration. *Developmental Cell* **23**, 716-728 (2012). https://doi.org/10.1016/j.devcel.2012.08.010
95 Bieling, P. *et al.* CLIP-170 tracks growing microtubule ends by dynamically recognizing composite EB1/tubulin-binding sites. *Journal of Cell Biology* **183**, 1223-1233 (2008). https://doi.org/10.1083/jcb.200809190
96 Gadadhar, S. *et al.* Tubulin glycylation controls primary cilia length. *Journal of Cell Biology* **216**, 2701-2713 (2017). https://doi.org/10.1083/jcb.201612050
97 Bré, M.-H. *et al.* Axonemal tubulin polyglycylation probed with two monoclonal antibodies: widespread evolutionary distribution, appearance during spermatozoan maturation and possible function in motility. *Journal of Cell Science* **109**, 727-738 (1996). https://doi.org/10.1242/jcs.109.4.727
98 Xia, L. *et al.* Polyglycylation of Tubulin Is Essential and Affects Cell Motility and Division in Tetrahymena thermophila. *Journal of Cell Biology* **149**, 1097-1106 (2000). https://doi.org/10.1083/jcb.149.5.1097
99 Million, K. *et al.* Polyglutamylation and polyglycylation of alpha- and beta-tubulins during in vitro ciliated cell differentiation of human respiratory epithelial cells. *Journal of Cell Science* **112**, 4357-4366 (1999). https://doi.org/10.1242/jcs.112.23.4357
100 Wloga, D. & Gaertig, J. Post-translational modifications of microtubules. *Journal of Cell Science* **123**, 3447-3455 (2010). https://doi.org/10.1242/jcs.063727
101 Janke, C. & Chloë Bulinski, J. Post-translational regulation of the microtubule cytoskeleton: mechanisms and functions. *Nature Reviews Molecular Cell Biology* **12**, 773-786 (2011). https://doi.org/10.1038/nrm3227
102 Janke, C., Rogowski, K. & Van Dijk, J. Polyglutamylation: a fine‐regulator of protein function? *EMBO reports* **9**, 636-641 (2008). https://doi.org/10.1038/embor.2008.114
103 Abal, M., Keryer, G. & Bornens, M. Centrioles resist forces applied on centrosomes during G2/M transition. *Biology of the Cell* **97**, 425-434 (2005). https://doi.org/10.1042/BC20040112
104 Audebert, S. *et al.* Developmental regulation of polyglutamylated α- and β-tubulin in mouse brain neurons. *Journal of Cell Science* **107**, 2313-2322 (1994). https://doi.org/10.1242/jcs.107.8.2313
105 Sirajuddin, M., Rice, L. M. & Vale, R. D. Regulation of microtubule motors by tubulin isotypes and post-translational modifications. *Nature Cell Biology* **16**, 335-344 (2014). https://doi.org/10.1038/ncb2920
106 Lacroix, B. *et al.* Tubulin polyglutamylation stimulates spastin-mediated microtubule severing. *Journal of Cell Biology* **189**, 945-954 (2010). https://doi.org/10.1083/jcb.201001024
107 Hausrat, T. J. *et al.* Disruption of tubulin-alpha4a polyglutamylation prevents aggregation of hyper-phosphorylated tau and microglia activation in mice. *Nature Communications* **13**, 4192 (2022). https://doi.org/10.1038/s41467-022-31776-5
108 Wirschell, M. *et al.* The nexin-dynein regulatory complex subunit DRC1 is essential for motile cilia function in algae and humans. *Nature Genetics* **45**, 262-268 (2013). https://doi.org/10.1038/ng.2533

109 Lin, J., Okada, K., Raytchev, M., Smith, M. C. & Nicastro, D. Structural mechanism of the dynein power stroke. *Nature Cell Biology* **16**, 479-485 (2014). https://doi.org/10.1038/ncb2939
110 Wieczorek, M., Bechstedt, S., Chaaban, S. & Brouhard, G. J. Microtubule-associated proteins control the kinetics of microtubule nucleation. *Nature Cell Biology* **17**, 907-916 (2015). https://doi.org/10.1038/ncb3188
111 Monroy, B. Y. *et al.* A Combinatorial MAP Code Dictates Polarized Microtubule Transport. *Developmental Cell* **53**, 60-72.e64 (2020). https://doi.org/https://doi.org/10.1016/j.devcel.2020.01.029
112 Janke, C. *et al.* Phylogenetic diversity of the expression of the microtubule-associated protein tau: implications for neurodegenerative disorders. *Molecular Brain Research* **68**, 119-128 (1999). https://doi.org/10.1016/S0169-328X(99)00079-0
113 Sen, I., Veprintsev, D., Akhmanova, A. & Steinmetz, M. O. End Binding Proteins Are Obligatory Dimers. *PLoS ONE* **8**, e74448 (2013). https://doi.org/10.1371/journal.pone.0074448
114 Berges, R. *et al.* End-binding 1 protein overexpression correlates with glioblastoma progression and sensitizes to Vinca -alkaloids in vitro and in vivo. *Oncotarget* **5**, 12769-12787 (2014). https://doi.org/10.18632/oncotarget.2646
115 Cheng, Y., Sun, M., Wang, F., Geng, X. & Wang, F. Identification of Hub Genes Related to Alzheimer's Disease and Major Depressive Disorder. *American Journal of Alzheimer's Disease & Other Dementias®* **36**, 153331752110461 (2021). https://doi.org/10.1177/15333175211046123
116 Ayaz, P., Ye, X., Huddleston, P., Brautigam, C. A. & Rice, L. M. A TOG:αβ-tubulin Complex Structure Reveals Conformation-Based Mechanisms for a Microtubule Polymerase. *Science* **337**, 857-860 (2012). https://doi.org/10.1126/science.1221698
117 Al-Jassar, C. *et al.* The Ciliopathy-Associated Cep104 Protein Interacts with Tubulin and Nek1 Kinase. *Structure* **25**, 146-156 (2017). https://doi.org/10.1016/j.str.2016.11.014
118 Lindeboom, J. J. *et al.* A Mechanism for Reorientation of Cortical Microtubule Arrays Driven by Microtubule Severing. *Science* **342**, 1245533 (2013). https://doi.org/10.1126/science.1245533
119 Smith, L. B. *et al.* KATNAL1 Regulation of Sertoli Cell Microtubule Dynamics Is Essential for Spermiogenesis and Male Fertility. *PLoS Genetics* **8**, e1002697 (2012). https://doi.org/10.1371/journal.pgen.1002697
120 Lombino, F. L. *et al.* The Microtubule Severing Protein Katanin Regulates Proliferation of Neuronal Progenitors in Embryonic and Adult Neurogenesis. *Scientific Reports* **9**, 15940 (2019). https://doi.org/10.1038/s41598-019-52367-3
121 Sharma, N. *et al.* Katanin regulates dynamics of microtubules and biogenesis of motile cilia. *Journal of Cell Biology* **178**, 1065-1079 (2007). https://doi.org/10.1083/jcb.200704021
122 Tan, R. *et al.* Microtubules gate tau condensation to spatially regulate microtubule functions. *Nature Cell Biology* **21**, 1078-1085 (2019). https://doi.org/10.1038/s41556-019-0375-5

123 Gao, X. *et al.* Treatment of autosomal dominant hearing loss by in vivo delivery of genome editing agents. *Nature* **553**, 217-221 (2018). https://doi.org/10.1038/nature25164
124 McVicker, D. P., Chrin, L. R. & Berger, C. L. The Nucleotide-binding State of Microtubules Modulates Kinesin Processivity and the Ability of Tau to Inhibit Kinesin-mediated Transport. *Journal of Biological Chemistry* **286**, 42873-42880 (2011). https://doi.org/10.1074/jbc.M111.292987
125 Chaudhary, A. R., Berger, F., Berger, C. L. & Hendricks, A. G. Tau directs intracellular trafficking by regulating the forces exerted by kinesin and dynein teams. *Traffic* **19**, 111-121 (2018). https://doi.org/10.1111/tra.12537
126 Barlan, K., Lu, W. & Gelfand, Vladimir I. The Microtubule-Binding Protein Ensconsin Is an Essential Cofactor of Kinesin-1. *Current Biology* **23**, 317-322 (2013). https://doi.org/10.1016/j.cub.2013.01.008
127 Sloboda, R. D., Rudolph, S. A., Rosenbaum, J. L. & Greengard, P. Cyclic AMP-dependent endogenous phosphorylation of a microtubule-associated protein. *Proceedings of the National Academy of Sciences* **72**, 177-181 (1975). https://doi.org/10.1073/pnas.72.1.177
128 Weingarten, M. D., Lockwood, A. H., Hwo, S. Y. & Kirschner, M. W. A protein factor essential for microtubule assembly. *Proceedings of the National Academy of Sciences* **72**, 1858-1862 (1975). https://doi.org/10.1073/pnas.72.5.1858
129 Herzog, W. & Weber, K. Fractionation of Brain Microtubule-Associated Proteins. Isolation of Two Different Proteins which Stimulate Tubulin Polymerization in vitro. *European Journal of Biochemistry* **92**, 1-8 (1978). https://doi.org/10.1111/j.1432-1033.1978.tb12716.x
130 McAlear, T. S. & Bechstedt, S. The mitotic spindle protein CKAP2 potently increases formation and stability of microtubules. *eLife* **11**, e72202 (2022). https://doi.org/10.7554/eLife.72202
131 Karki, S. & Holzbaur, E. L. Cytoplasmic dynein and dynactin in cell division and intracellular transport. *Current Opinion in Cell Biology* **11**, 45-53 (1999). https://doi.org/10.1016/S0955-0674(99)80006-4
132 Sweeney, H. L. & Holzbaur, E. L. F. Motor Proteins. *Cold Spring Harbor Perspectives in Biology* **10**, a021931 (2018). https://doi.org/10.1101/cshperspect.a021931
133 Hirokawa, N. Kinesin and Dynein Superfamily Proteins and the Mechanism of Organelle Transport. *Science* **279**, 519-526 (1998). https://doi.org/10.1126/science.279.5350.519
134 Hendel, N. L., Thomson, M. & Marshall, W. F. Diffusion as a Ruler: Modeling Kinesin Diffusion as a Length Sensor for Intraflagellar Transport. *Biophysical Journal* **114**, 663-674 (2018). https://doi.org/10.1016/j.bpj.2017.11.3784
135 Wemmer, K., Ludington, W. & Marshall, W. F. Testing the role of intraflagellar transport in flagellar length control using length-altering mutants of Chlamydomonas. *Philosophical Transactions of the Royal Society B: Biological Sciences* **375**, 20190159 (2020). https://doi.org/10.1098/rstb.2019.0159
136 Oda, T., Yanagisawa, H., Kamiya, R. & Kikkawa, M. A molecular ruler determines the repeat length in eukaryotic cilia and flagella. *Science* **346**, 857-860 (2014).

137 Becker-Heck, A. *et al.* The coiled-coil domain containing protein CCDC40 is essential for motile cilia function and left-right axis formation. *Nature Genetics* **43**, 79-84 (2011). https://doi.org/10.1038/ng.727
138 Merveille, A.-C. *et al.* CCDC39 is required for assembly of inner dynein arms and the dynein regulatory complex and for normal ciliary motility in humans and dogs. *Nature Genetics* **43**, 72-78 (2011). https://doi.org/10.1038/ng.726
139 Owa, M. *et al.* Inner lumen proteins stabilize doublet microtubules in cilia and flagella. *Nature Communications* **10**, 1143 (2019). https://doi.org/10.1038/s41467-019-09051-x
140 Nicastro, D. *et al.* The Molecular Architecture of Axonemes Revealed by Cryoelectron Tomography. *Science* **313**, 944-948 (2006). https://doi.org/10.1126/science.1128618
141 Linck, R. W. & Norrander, J. M. Protofilament Ribbon Compartments of Ciliary and Flagellar Microtubules. *Protist* **154**, 299-311 (2003). https://doi.org/10.1078/143446103322454086
142 Kubo, S. *et al.* Native doublet microtubules from Tetrahymena thermophila reveal the importance of outer junction proteins. *Nature Communications* **14**, 2168 (2023). https://doi.org/10.1038/s41467-023-37868-0
143 Fabritius, A. S. *et al.* Proteomic analysis of microtubule inner proteins (MIPs) in Rib72 null Tetrahymena cells reveals functional MIPs. *Molecular Biology of the Cell* **32**, br8 (2021). https://doi.org/10.1091/mbc.E20-12-0786
144 Stoddard, D. *et al.* Tetrahymena RIB72A and RIB72B are microtubule inner proteins in the ciliary doublet microtubules. *Molecular Biology of the Cell* **29**, 2566-2577 (2018). https://doi.org/10.1091/mbc.E18-06-0405
145 King, S. M. Axonemal protofilament ribbons, DM10 domains, and the link to juvenile myoclonic epilepsy. *Cell Motil Cytoskeleton* **63**, 245-253 (2006).
146 Suzuki, T., Inoue, I. & Yamakawa, K. Epilepsy protein Efhc1/myoclonin1 is expressed in cells with motile cilia but not in neurons or mitotic apparatuses in brain. *Sci Rep* **10**, 22076 (2020).
147 Linck, R. & Stephens, R. Biochemical characterization of tektins from sperm flagellar doublet microtubules. *Journal of Cell Biology* **104**, 1069-1075 (1987). https://doi.org/10.1083/jcb.104.4.1069
148 Ryan, R. *et al.* Functional characterization of tektin-1 in motile cilia and evidence for TEKT1 as a new candidate gene for motile ciliopathies. *Human Molecular Genetics* **27**, 266-282 (2018). https://doi.org/10.1093/hmg/ddx396
149 Liu, Y. *et al.* Bi-allelic human TEKT3 mutations cause male infertility with oligoasthenoteratozoospermia owing to acrosomal hypoplasia and reduced progressive motility. *Human Molecular Genetics* **32**, 1730-1740 (2023). https://doi.org/10.1093/hmg/ddad013
150 Stephenson, S. E. M. *et al.* Generation and characterisation of a parkin-Pacrg knockout mouse line and a Pacrg knockout mouse line. *Scientific Reports* **8**, 7528 (2018). https://doi.org/10.1038/s41598-018-25766-1
151 Li, S., Fernandez, J.-J., Fabritius, A. S., Agard, D. A. & Winey, M. Electron cryo-tomography structure of axonemal doublet microtubule from Tetrahymena thermophila. *Life Science Alliance* **5**, e202101225 (2022). https://doi.org/10.26508/lsa.202101225

152 Vent, J. *et al.* Direct involvement of the isotype-specific C-terminus of β tubulin in ciliary beating. *Journal of Cell Science* **118**, 4333-4341 (2005). https://doi.org/10.1242/jcs.02550
153 Bosch Grau, M. Tubulin glycylases and glutamylases have distinct functions in stabilization and motility of ependymal cilia. *J Cell Biol* **202**, 441-451 (2013).
154 Knaysi, G. Cytology of bacteria. *The Botanical Review* **4**, 83-112 (1938). https://doi.org/10.1007/BF02875629
155 Briggs, J. A. Structural biology in situ—the potential of subtomogram averaging. *Current Opinion in Structural Biology* **23**, 261-267 (2013). https://doi.org/10.1016/j.sbi.2013.02.003
156 White, H. E., Ignatiou, A., Clare, D. K. & Orlova, E. V. Structural Study of Heterogeneous Biological Samples by Cryoelectron Microscopy and Image Processing. *BioMed Research International* **2017**, 1-23 (2017). https://doi.org/10.1155/2017/1032432
157 Dubochet, J. & McDowall, A. W. VITRIFICATION OF PURE WATER FOR ELECTRON MICROSCOPY. *Journal of Microscopy* **124**, 3-4 (1981). https://doi.org/10.1111/j.1365-2818.1981.tb02483.x
158 Henderson, R., Raeburn, C. & Vigers, G. A side-entry cold holder for cryo-electron microscopy. *Ultramicroscopy* **35**, 45-53 (1991). https://doi.org/10.1016/0304-3991(91)90043-6
159 Faruqi, A. R., Cattermole, D. M., Henderson, R., Mikulec, B. & Raeburn, C. Evaluation of a hybrid pixel detector for electron microscopy. *Ultramicroscopy* **94**, 263-276 (2003). https://doi.org/10.1016/S0304-3991(02)00336-4
160 Frank, J. Detection of Object Movement in the Optical Diffractograms of Electron Micrographs. *Optik* **30** (1969).
161 Henderson, R. & Unwin, P. N. T. Three-dimensional model of purple membrane obtained by electron microscopy. *Nature* **257**, 28-32 (1975). https://doi.org/10.1038/257028a0
162 Scheres, S. H. W. RELION: Implementation of a Bayesian approach to cryo-EM structure determination. *Journal of Structural Biology* **180**, 519-530 (2012). https://doi.org/10.1016/j.jsb.2012.09.006
163 Zivanov, J. *et al.* A Bayesian approach to single-particle electron cryo-tomography in RELION-4.0. *eLife* **11**, e83724 (2022). https://doi.org/10.7554/eLife.83724
164 Doerr, A. Single-particle cryo-electron microscopy. *Nature Methods* **13**, 23-23 (2016). https://doi.org/10.1038/nmeth.3700
165 Skiniotis, G. & Southworth, D. R. Single-particle cryo-electron microscopy of macromolecular complexes. *Microscopy* **65**, 9-22 (2016). https://doi.org/10.1093/jmicro/dfv366
166 Emsley, P. & Cowtan, K. Coot : model-building tools for molecular graphics. *Acta Crystallographica Section D Biological Crystallography* **60**, 2126-2132 (2004). https://doi.org/10.1107/S0907444904019158
167 Ramachandran, G. N., Ramakrishnan, C. & Sasisekharan, V. Stereochemistry of polypeptide chain configurations. *Journal of Molecular Biology* **7**, 95-99 (1963). https://doi.org/10.1016/S0022-2836(63)80023-6

168 Adams, P. D. *et al.* PHENIX : a comprehensive Python-based system for macromolecular structure solution. *Acta Crystallographica Section D Biological Crystallography* **66**, 213-221 (2010). https://doi.org/10.1107/S0907444909052925
169 Pfab, J., Phan, N. M. & Si, D. DeepTracer for fast de novo cryo-EM protein structure modeling and special studies on CoV-related complexes. *Proc Natl Acad Sci U S A* **118** (2021).
170 Jumper, J. *et al.* Highly accurate protein structure prediction with AlphaFold. *Nature* **596**, 583-589 (2021). https://doi.org/10.1038/s41586-021-03819-2
171 Varadi, M. *et al.* AlphaFold Protein Structure Database: massively expanding the structural coverage of protein-sequence space with high-accuracy models. *Nucleic Acids Research* **50**, D439-D444 (2022). https://doi.org/10.1093/nar/gkab1061
172 Chang, L. *et al.* DeepTracer-ID: De novo protein identification from cryo-EM maps. *Biophysical Journal* **121**, 2840-2848 (2022). https://doi.org/10.1016/j.bpj.2022.06.025
173 Chojnowski, G. *et al.* findMySequence : a neural-network-based approach for identification of unknown proteins in X-ray crystallography and cryo-EM. *IUCrJ* **9**, 86-97 (2022). https://doi.org/10.1107/S2052252521011088
174 Jamali, K. *et al.* Automated model building and protein identification in cryo-EM maps. (Molecular Biology, 2023).
175 Stahl, K., Graziadei, A., Dau, T., Brock, O. & Rappsilber, J. Protein structure prediction with in-cell photo-crosslinking mass spectrometry and deep learning. *Nature Biotechnology* (2023). https://doi.org/10.1038/s41587-023-01704-z
176 Maheshwari, A. & Ishikawa, T. Heterogeneity of dynein structure implies coordinated suppression of dynein motor activity in the axoneme. *Journal of Structural Biology* **179**, 235-241 (2012). https://doi.org/https://doi.org/10.1016/j.jsb.2012.04.018
177 Maheshwari, A. *et al.* α- and β-Tubulin Lattice of the Axonemal Microtubule Doublet and Binding Proteins Revealed by Single Particle Cryo-Electron Microscopy and Tomography. *Structure* **23**, 1584-1595 (2015). https://doi.org/https://doi.org/10.1016/j.str.2015.06.017
178 Black, C., Dai, D., Bui, K., Ichikawa, M. & Peri, K. Preparation of Doublet Microtubule Fraction for Single Particle Cryo-electron Microscopy. *BIO-PROTOCOL* **11** (2021). https://doi.org/10.21769/BioProtoc.4041
179 Kubo, S. *et al.* Remodeling and activation mechanisms of outer arm dyneins revealed by cryo‐EM. *EMBO reports* **22**, e52911 (2021). https://doi.org/10.15252/embr.202152911
180 Ghanaeian, A. *et al.* Integrated modeling of the Nexin-dynein regulatory complex reveals its regulatory mechanism. *bioRxiv*, 2023.2005.2031.543107 (2023). https://doi.org/10.1101/2023.05.31.543107
181 Williams, N. E., Wolfe, J. & Bleyman, L. K. Long-Term Maintenance of Tetrahymena Spp.: Long-Term Maintenance of Tetrahymena spp. *The Journal of Protozoology* **27**, 327-327 (1980). https://doi.org/10.1111/j.1550-7408.1980.tb04270.x
182 Mastronarde, D. N. Automated electron microscope tomography using robust prediction of specimen movements. *J Struct Biol* **152**, 36-51 (2005).
183 Zivanov, J. New tools for automated high-resolution cryo-EM structure determination in RELION-3. *Elife* **7** (2018).

184 Zheng SQ, P. E., Armache JP, Verba KA, Cheng Y, Agard DA. MotionCor2: anisotropic correction of beam-induced motion for improved cryo-electron microscopy. *Nat Methods* **14**, 331-332 (2017).
185 Zhang, K. Gctf: Real-time CTF determination and correction. *J Struct Biol* **193**, 1-12 (2016).
186 Bepler, T. Positive-unlabeled convolutional neural networks for particle picking in cryo-electron micrographs. *Nat Methods* **16**, 1153-1160 (2019).
187 Egelman, E. H. The iterative helical real space reconstruction method: surmounting the problems posed by real polymers. *J Struct Biol* **157**, 83-94 (2007).
188 Frank, J., Radermacher, M., Penczek, P., Zhu, J., Li, Y., Ladjadj, M., & Leith, A. SPIDER and WEB: processing and visualization of images in 3D electron microscopy and related fields. *J Struct Biol* **116**, 190-199 (1996).
189 Grigorieff, N. FREALIGN: high-resolution refinement of single particle structures. *J Struct Biol* **157**, 117-125 (2007).
190 Afonine, P. V. *et al.* Real-space refinement in PHENIX for cryo-EM and crystallography. *Acta Crystallographica Section D Structural Biology* **74**, 531-544 (2018). https://doi.org/10.1107/S2059798318006551
191 Sanchez-Garcia, R. *et al.* DeepEMhancer: a deep learning solution for cryo-EM volume post-processing. *Communications Biology* **4**, 874 (2021). https://doi.org/10.1038/s42003-021-02399-1
192 Pfab, J., Phan, N. M. & Si, D. DeepTracer for fast de novo cryo-EM protein structure modeling and special studies on CoV-related complexes. *Proceedings of the National Academy of Sciences* **118**, e2017525118 (2021). https://doi.org/10.1073/pnas.2017525118
193 Mirdita, M. *et al.* ColabFold: making protein folding accessible to all. *Nature Methods* **19**, 679-682 (2022). https://doi.org/10.1038/s41592-022-01488-1
194 Emsley, P., Lohkamp, B., Scott, W. G. & Cowtan, K. Features and development of Coot. *Acta Crystallographica Section D Biological Crystallography* **66**, 486-501 (2010). https://doi.org/10.1107/S0907444910007493
195 Vertrees, J. cealign: A structure alignment plugin for PyMol. (2007).
196 Finn, R. D., Clements, J. & Eddy, S. R. HMMER web server: interactive sequence similarity searching. *Nucleic Acids Research* **39**, W29-W37 (2011). https://doi.org/10.1093/nar/gkr367
197 Pagnuco, I. A., Revuelta, M. V., Bondino, H. G., Brun, M. & Ten Have, A. HMMER Cut-off Threshold Tool (HMMERCTTER): Supervised classification of superfamily protein sequences with a reliable cut-off threshold. *PLOS ONE* **13**, e0193757 (2018). https://doi.org/10.1371/journal.pone.0193757
198 Northey, T. C., Barešić, A. & Martin, A. C. R. IntPred: a structure-based predictor of protein–protein interaction sites. *Bioinformatics* **34**, 223-229 (2018). https://doi.org/10.1093/bioinformatics/btx585
199 Akella, J. S. *et al.* MEC-17 is an α-tubulin acetyltransferase. *Nature* **467**, 218-222 (2010). https://doi.org/10.1038/nature09324
200 Yanagisawa, H.-a. *et al.* FAP20 is an inner junction protein of doublet microtubules essential for both the planar asymmetrical waveform and stability of flagella in

Chlamydomonas. *Molecular Biology of the Cell* **25**, 1472-1483 (2014). https://doi.org/10.1091/mbc.e13-08-0464

201 Dymek, E. E., Lin, J., Fu, G., Porter, M. E., Nicastro, D., & Smith, E. F. PACRG and FAP20 form the inner junction of axonemal doublet microtubules and regulate ciliary motility. *Mol Biol Cell* **30**, 1805-1816 (2019).

202 Norrander, J. M., deCathelineau, A. M., Brown, J. A., Porter, M. E. & Linck, R. W. The Rib43a Protein Is Associated with Forming the Specialized Protofilament Ribbons of Flagellar Microtubules in Chlamydomonas. *Molecular Biology of the Cell* **11**, 201-215 (2000). https://doi.org/10.1091/mbc.11.1.201

203 Ikeda, K., Brown, J. A., Yagi, T., Norrander, J. M., Hirono, M., Eccleston, E., Kamiya, R., & Linck, R. W. Rib72, a conserved protein associated with the ribbon compartment of flagellar A-microtubules and potentially involved in the linkage between outer doublet microtubules. *J Biol Chem* **278**, 7725-7734 (2003).

204 Kwon, K. Y., Jeong, H., Jang, D. G., Kwon, T. & Park, T. J. Ckb and Ybx2 interact with Ribc2 and are necessary for the ciliary beating of multi-cilia. *Genes & Genomics* **45**, 157-167 (2023). https://doi.org/10.1007/s13258-022-01350-w

205 Kang, K. *et al.* A Genome-Wide Methylation Approach Identifies a New Hypermethylated Gene Panel in Ulcerative Colitis. *International Journal of Molecular Sciences* **17**, 1291 (2016). https://doi.org/10.3390/ijms17081291

206 Xiong, M. *et al.* A common variant rs2272804 in the 5'UTR of RIBC2 inhibits downstream gene expression by creating an upstream open reading frame. *European Review for Medical and Pharmacological Sciences* **24**, 3839-3848 (2020). https://doi.org/10.26355/eurrev_202004_20851

207 McCafferty, C. L., Pennington, E. L., Papoulas, O., Taylor, D. W. & Marcotte, E. M. Does AlphaFold2 model proteins' intracellular conformations? An experimental test using cross-linking mass spectrometry of endogenous ciliary proteins. (2022).

208 Pazour, G. J., Agrin, N., Leszyk, J. & Witman, G. B. Proteomic analysis of a eukaryotic cilium. *J Cell Biol* **170**, 103-113 (2005). https://doi.org/10.1083/jcb.200504008

209 Patir, A. *et al.* The transcriptional signature associated with human motile cilia. *Sci Rep* **10**, 10814 (2020). https://doi.org/10.1038/s41598-020-66453-4

210 Kirima, J. & Oiwa, K. Flagellar-associated Protein FAP85 Is a Microtubule Inner Protein That Stabilizes Microtubules. *Cell Struct Funct* **43**, 1-14 (2018). https://doi.org/10.1247/csf.17023

211 Pirner, M. A. & Linck, R. W. Tektins are heterodimeric polymers in flagellar microtubules with axial periodicities matching the tubulin lattice. *J Biol Chem* **269**, 31800-31806 (1994).

212 Linck, R. W. Flagellar doublet microtubules: fractionation of minor components and alpha-tubulin from specific regions of the A-tubule. *J Cell Sci* **20**, 405-439 (1976).

213 Ikeda, K., Ikeda, T., Morikawa, K. & Kamiya, R. Axonemal localization of Chlamydomonas PACRG, a homologue of the human Parkin-coregulated gene product. *Cell Motil Cytoskeleton* **64**, 814-821 (2007). https://doi.org/10.1002/cm.20225

214 Bower, R. *et al.* DRC2/CCDC65 is a central hub for assembly of the nexin-dynein regulatory complex and other regulators of ciliary and flagellar motility. *Mol Biol Cell* **29**, 137-153 (2018). https://doi.org/10.1091/mbc.E17-08-0510

215 Qin, H. *et al.* Differential Gene Expression Modulated by the Cytoplasmic Domain of FcγRIa (CD64) α-Chain. *The Journal of Immunology* **173**, 6211-6219 (2004). https://doi.org/10.4049/jimmunol.173.10.6211
216 Diener, D. R. *et al.* Sequential assembly of flagellar radial spokes. *Cytoskeleton* **68**, 389-400 (2011). https://doi.org/10.1002/cm.20520
217 Porter, M. E. & Sale, W. S. The 9 + 2 Axoneme Anchors Multiple Inner Arm Dyneins and a Network of Kinases and Phosphatases That Control Motility. *Journal of Cell Biology* **151**, F37-F42 (2000). https://doi.org/10.1083/jcb.151.5.F37
218 Olson, G. E. & Linck, R. W. Observations of the structural components of flagellar axonemes and central pair microtubules from rat sperm. *Journal of Ultrastructure Research* **61**, 21-43 (1977). https://doi.org/10.1016/S0022-5320(77)90004-1
219 Heuser, T. *et al.* Cryoelectron tomography reveals doublet-specific structures and unique interactions in the I1 dynein. *Proceedings of the National Academy of Sciences* **109** (2012). https://doi.org/10.1073/pnas.1120690109
220 Pigino, G. *et al.* Cryoelectron tomography of radial spokes in cilia and flagella. *Journal of Cell Biology* **195**, 673-687 (2011). https://doi.org/10.1083/jcb.201106125
221 Barber, C. F., Heuser, T., Carbajal-González, B. I., Botchkarev, V. V. & Nicastro, D. Three-dimensional structure of the radial spokes reveals heterogeneity and interactions with dyneins in Chlamydomonas flagella. *Molecular Biology of the Cell* **23**, 111-120 (2012). https://doi.org/10.1091/mbc.e11-08-0692
222 Lin, J. *et al.* Cryo-electron tomography reveals ciliary defects underlying human RSPH1 primary ciliary dyskinesia. *Nature Communications* **5**, 5727 (2014). https://doi.org/10.1038/ncomms6727
223 Ferro, L. S., Fang, Q., Eshun-Wilson, L., Fernandes, J., Jack, A., Farrell, D. P., Golcuk, M., Huijben, T., Costa, K., Gur, M., DiMaio, F., Nogales, E., & Yildiz, A. Structural and functional insight into regulation of kinesin-1 by microtubule-associated protein MAP7. *Science* **375**, 326-331 (2022).
224 Sung, H.-H. *et al.* Drosophila Ensconsin Promotes Productive Recruitment of Kinesin-1 to Microtubules. *Developmental Cell* **15**, 866-876 (2008). https://doi.org/10.1016/j.devcel.2008.10.006
225 Monroy, B. Y. *et al.* Competition between microtubule-associated proteins directs motor transport. *Nature Communications* **9**, 1487 (2018). https://doi.org/10.1038/s41467-018-03909-2
226 Kiesel, P. *et al.* The molecular structure of mammalian primary cilia revealed by cryo-electron tomography. *Nature Structural & Molecular Biology* **27**, 1115-1124 (2020). https://doi.org/10.1038/s41594-020-0507-4
227 Chandrasekaran, A., Ojeda, A. M., Kolmakova, N. G. & Parsons, S. M. Mutational and bioinformatics analysis of proline- and glycine-rich motifs in vesicular acetylcholine transporter. *Journal of Neurochemistry* **98**, 1551-1559 (2006). https://doi.org/10.1111/j.1471-4159.2006.03975.x
228 Montserrat Bosch Grau , G. G. C., Cecilia Rocha , Maria M. Magiera , Patricia Marques Sousa , Tiziana Giordano , Nathalie Spassky , Carsten Janke. Tubulin glycylases and glutamylases have distinct functions in stabilization and motility of ependymal cilia. *J Cell Biol* **202**, 441-451 (2013).

229 Mastronarde, D. N. & Held, S. R. Automated tilt series alignment and tomographic reconstruction in IMOD. *Journal of Structural Biology* **197**, 102-113 (2017). https://doi.org/10.1016/j.jsb.2016.07.011
230 Kremer, J. R., Mastronarde, D. N. & McIntosh, J. R. Computer Visualization of Three-Dimensional Image Data Using IMOD. *Journal of Structural Biology* **116**, 71-76 (1996). https://doi.org/10.1006/jsbi.1996.0013
231 Tegunov, D. & Cramer, P. Real-time cryo-electron microscopy data preprocessing with Warp. *Nat Methods* **16**, 1146-1152 (2019).
232 Bui, K. H. & Ishikawa, T. in *Methods in Enzymology* Vol. 524 305-323 (Elsevier, 2013).
233 Liu, Y.-T. *et al.* Isotropic reconstruction for electron tomography with deep learning. *Nature Communications* **13**, 6482 (2022). https://doi.org/10.1038/s41467-022-33957-8
234 McEwen, B. F., Marko, M., Hsieh, C.-E. & Mannella, C. Use of frozen-hydrated axonemes to assess imaging parameters and resolution limits in cryoelectron tomography. *Journal of Structural Biology* **138**, 47-57 (2002). https://doi.org/10.1016/S1047-8477(02)00020-5
235 Pettersen, E. F. UCSF ChimeraX: Structure visualization for researchers, educators, and developers. *Protein Sci* **30**, 70-82 (2021).
236 Kenzaki, H. CafeMol: A Coarse-Grained Biomolecular Simulator for Simulating Proteins at Work. *J Chem Theory Comput* **7**, 1979-1989 (2011).
237 Tan, C. *et al.* Implementation of residue-level coarse-grained models in GENESIS for large-scale molecular dynamics simulations. *PLOS Computational Biology* **18**, e1009578 (2022). https://doi.org/10.1371/journal.pcbi.1009578
238 Urbanska, P., Joachimiak, E., Bazan, R., Fu, G., Poprzeczko, M., Fabczak, H., Nicastro, D., & Wloga, D. Ciliary proteins Fap43 and Fap44 interact with each other and are essential for proper cilia and flagella beating. *Cell Mol Life Sci* **75**, 4479-4493 (2018).
239 Mochizuki, K. High efficiency transformation of Tetrahymena using a codon-optimized neomycin resistance gene. *Gene* **425**, 79-83 (2008).
240 Cassidy-Hanley, D. *et al.* Germline and Somatic Transformation of Mating Tetrahymena thermophila by Particle Bombardment. *Genetics* **146**, 135-147 (1997). https://doi.org/10.1093/genetics/146.1.135
241 Bazan, R. *et al.* Ccdc113/Ccdc96 complex, a novel regulator of ciliary beating that connects radial spoke 3 to dynein g and the nexin link. *PLOS Genetics* **17**, e1009388 (2021). https://doi.org/10.1371/journal.pgen.1009388
242 Duan, J. & Gorovsky, M. A. Both carboxy-terminal tails of alpha- and beta-tubulin are essential, but either one will suffice. *Curr Biol* **12**, 313-316 (2002).
243 Wolff, A., de Néchaud, B., Chillet, D., Mazarguil, H., Desbruyères, E., Audebert, S., Eddé, B., Gros, F., & Denoulet, P. Distribution of glutamylated alpha and beta-tubulin in mouse tissues using a specific monoclonal antibody, GT335. *European journal of cell biology **59***, 425–432 (1992).
244 Jerka-Dziadosz, M. *et al.* Cellular Polarity in Ciliates: Persistence of Global Polarity in a disorganized Mutant of Tetrahymena thermophila That Disrupts Cytoskeletal Organization. *Developmental Biology* **169**, 644-661 (1995). https://doi.org/https://doi.org/10.1006/dbio.1995.1176

245 Wloga, D., Camba, A., Rogowski, K., Manning, G., Jerka-Dziadosz, M., & Gaertig, J. Members of the NIMA-related kinase family promote disassembly of cilia by multiple mechanisms. *Mol Biol Cell* **17**, 2799-2810 (2006).
246 Schindelin, J. *et al.* Fiji: an open-source platform for biological-image analysis. *Nature Methods* **9**, 676-682 (2012). https://doi.org/10.1038/nmeth.2019
247 Janke, C., Rogowski, K., Wloga, D., Regnard, C., Kajava, A. V., Strub, J. M., Temurak, N., van Dijk, J., Boucher, D., van Dorsselaer, A., Suryavanshi, S., Gaertig, J., & Eddé, B. Tubulin polyglutamylase enzymes are members of the TTL domain protein family. *Science* **308**, 1758-1762 (2005).
248 Cao, Y., Park, A. & Sun, Z. Intraflagellar transport proteins are essential for cilia formation and for planar cell polarity. *Journal of the American Society of Nephrology: JASN* **21**, 1326-1333 (2010). https://doi.org/10.1681/ASN.2009091001
249 Altschul, S. F., Gish, W., Miller, W., Myers, E. W. & Lipman, D. J. Basic local alignment search tool. *Journal of Molecular Biology* **215**, 403-410 (1990). https://doi.org/10.1016/S0022-2836(05)80360-2
250 Rice, P., Longden, I. & Bleasby, A. EMBOSS: The European Molecular Biology Open Software Suite. *Trends in Genetics* **16**, 276-277 (2000). https://doi.org/10.1016/S0168-9525(00)02024-2
251 Mick, David U. *et al.* Proteomics of Primary Cilia by Proximity Labeling. *Developmental Cell* **35**, 497-512 (2015). https://doi.org/10.1016/j.devcel.2015.10.015
252 Walsh, V. & Goodman, J. The billion dollar molecule: Taxol in historical and theoretical perspective. *Clio Medica (Amsterdam, Netherlands)* **66**, 245-267 (2002). https://doi.org/10.1163/9789004333499_013
253 Schiff, P. B., Fant, J. & Horwitz, S. B. Promotion of microtubule assembly in vitro by taxol. *Nature* **277**, 665-667 (1979). https://doi.org/10.1038/277665a0
254 Löwe, J., Li, H., Downing, K. H. & Nogales, E. Refined structure of αβ-tubulin at 3.5 Å resolution11Edited by I. A. Wilson. *Journal of Molecular Biology* **313**, 1045-1057 (2001). https://doi.org/https://doi.org/10.1006/jmbi.2001.5077
255 Kellogg, E. H. *et al.* Insights into the Distinct Mechanisms of Action of Taxane and Non-Taxane Microtubule Stabilizers from Cryo-EM Structures. *Journal of Molecular Biology* **429**, 633-646 (2017). https://doi.org/10.1016/j.jmb.2017.01.001
256 Gillies, R. J. & Deamer, D. W. Intracellular pH changes during the cell cycle inTetrahymena. *Journal of Cellular Physiology* **100**, 23-31 (1979). https://doi.org/10.1002/jcp.1041000103
257 Hegde, R. S. & Zavodszky, E. Recognition and Degradation of Mislocalized Proteins in Health and Disease. *Cold Spring Harbor Perspectives in Biology* **11**, a033902 (2019). https://doi.org/10.1101/cshperspect.a033902
258 Agarwal-Mawal, A. *et al.* 14-3-3 Connects Glycogen Synthase Kinase-3β to Tau within a Brain Microtubule-associated Tau Phosphorylation Complex. *Journal of Biological Chemistry* **278**, 12722-12728 (2003). https://doi.org/10.1074/jbc.M211491200
259 Lessard, D. V. *et al.* Polyglutamylation of tubulin's C-terminal tail controls pausing and motility of kinesin-3 family member KIF1A. *Journal of Biological Chemistry* **294**, 6353-6363 (2019). https://doi.org/10.1074/jbc.RA118.005765

260 Valenstein, Max L. & Roll-Mecak, A. Graded Control of Microtubule Severing by Tubulin Glutamylation. *Cell* **164**, 911-921 (2016). https://doi.org/10.1016/j.cell.2016.01.019
261 Tran, M. V. *et al.* MAP9/MAPH-9 supports axonemal microtubule doublets and modulates motor movement. *bioRxiv*, 2023.2002.2023.529616 (2023). https://doi.org/10.1101/2023.02.23.529616
262 Kirima, J. & Oiwa, K. Flagellar-associated Protein FAP85 Is a Microtubule Inner Protein That Stabilizes Microtubules. *Cell Structure and Function* **43**, 1-14 (2018). https://doi.org/10.1247/csf.17023
263 Hendricks, A. G. & Goldman, Y. E. in *Optical Tweezers* Vol. 1486 (ed Arne Gennerich) 537-552 (Springer New York, 2017).
264 Tymanskyj, S. R., Yang, B. H., Verhey, K. J. & Ma, L. MAP7 regulates axon morphogenesis by recruiting kinesin-1 to microtubules and modulating organelle transport. *eLife* **7**, e36374 (2018). https://doi.org/10.7554/eLife.36374
265 Blackburn, K., Bustamante-Marin, X., Yin, W., Goshe, M. B. & Ostrowski, L. E. Quantitative Proteomic Analysis of Human Airway Cilia Identifies Previously Uncharacterized Proteins of High Abundance. *J Proteome Res* **16**, 1579-1592 (2017).
266 Montalvo-Ortiz, J. L., Cheng, Z., Kranzler, H. R., Zhang, H. & Gelernter, J. Genomewide Study of Epigenetic Biomarkers of Opioid Dependence in European- American Women. *Sci Rep* **9**, 4660 (2019).
267 Zhang, P. f. *et al.* Integrated analysis of phosphoproteome and ubiquitylome in epididymal sperm of buffalo (Bubalus bubalis). *Molecular Reproduction and Development* **88**, 15-33 (2021). https://doi.org/10.1002/mrd.23432
268 Inaba, H., Sueki, Y., Ichikawa, M., Kabir, A. M. R., Iwasaki, T., Shigematsu, H., Kakugo, A., Sada, K., Tsukazaki, T., & Matsuura, K. Generation of stable microtubule superstructures by binding of peptide-fused tetrameric proteins to inside and outside. *Sci Adv* **8, eabq3817** (2022).
269 Landrein, B. *et al.* Mechanical stress contributes to the expression of the STM homeobox gene in Arabidopsis shoot meristems. *eLife* **4**, e07811 (2015). https://doi.org/10.7554/eLife.07811
270 Hill, D. B. *et al.* Force Generation and Dynamics of Individual Cilia under External Loading. *Biophysical Journal* **98**, 57-66 (2010). https://doi.org/10.1016/j.bpj.2009.09.048
271 Janke, C. The tubulin code: Molecular components, readout mechanisms, and functions. *Journal of Cell Biology* **206**, 461-472 (2014). https://doi.org/10.1083/jcb.201406055
272 Genova, M. *et al.* Tubulin polyglutamylation differentially regulates microtubule‐interacting proteins. *The EMBO Journal* **42**, e112101 (2023). https://doi.org/10.15252/embj.2022112101
273 Kubo, S. & Bui, K. H. Regulatory mechanisms of the dynein-2 motility by post-translational modification revealed by MD simulation. *Scientific Reports* **13**, 1477 (2023). https://doi.org/10.1038/s41598-023-28026-z
274 Chen, Z. *et al.* De novo protein identification in mammalian sperm using high-resolution in situ cryo-electron tomography. (Biophysics, 2022).